



## GR Focus

## Early Mesozoic magmatism and tectonic evolution of the Qinling Orogen: Implications for oblique continental collision



Fangyang Hu <sup>a,b,c</sup>, Shuwen Liu <sup>b,\*</sup>, Mihai N. Ducea <sup>c,d</sup>, James B. Chapman <sup>e</sup>, Fuyuan Wu <sup>a,f</sup>, Timothy Kusky <sup>g,h,i</sup>

<sup>a</sup> State Key Laboratory of Lithospheric Evolution, Institute of Geology and Geophysics, Chinese Academy of Sciences, Beijing 100029, PR China

<sup>b</sup> Key Laboratory of Orogenic Belts and Crustal Evolution, Ministry of Education, School of Earth and Space Sciences, Peking University, Beijing 100871, PR China

<sup>c</sup> Department of Geosciences, University of Arizona, Tucson, AZ 85721, USA

<sup>d</sup> Faculty of Geology and Geophysics, University of Bucharest, Bucharest, Romania

<sup>e</sup> Department of Geology and Geophysics, University of Wyoming, Laramie, WY 82071, USA

<sup>f</sup> College of Earth and Planetary Sciences, University of Chinese Academy of Sciences, Beijing 100049, PR China

<sup>g</sup> State Key Laboratory of Geological Processes and Mineral Resources, and Center for Global Tectonics, School of Earth Sciences, China University of Geosciences, Wuhan 430074, China

<sup>h</sup> Three Gorges Research Center for Geo-hazards, China University of Geosciences, Wuhan 430074, China

<sup>i</sup> Middle East Technical University, Department of Geological Engineering, 06800 Ankara, Turkey

## ARTICLE INFO

## Article history:

Received 18 January 2020

Received in revised form 14 July 2020

Accepted 20 July 2020

Available online 16 September 2020

Handling Editor: Y.P. Dong

## Keywords:

Qinling orogen

Magmatic mechanism

Tectonic evolution

Asymmetric pattern

Oblique continental collision

## ABSTRACT

The Qinling Orogenic Belt in Central China is formed by an oblique continental collision between the North China and South China Blocks. In this review, we summarize the knowledge of the early Mesozoic magmatism, in combination with the coeval metamorphic characteristics, regional structural features and depositional history in the foreland and hinterland basins along the Qinling-Dabie Orogen. The early Mesozoic tectonic evolution of the Qinling is divided into four stages. Stage I (~250–235 Ma) is characterized by medium-K calc-alkaline magmatism in the western Qinling induced by slab roll-back. Meanwhile, ultrahigh-pressure metamorphism was triggered by continental subduction in the Sulu-Dabie, indicating a diachronous closure of the ocean. Stage II (~235–225 Ma) is recognized as a magmatic gap. Depositional variations of sedimentary facies and compressional deformations with an increased crustal thickness reflect the initial collision in the Qinling. Stage III (~225–210 Ma) is distinguished by a magmatic flare-up event. Abundant mantle-derived melts coupled with extensive crustal-derived melts were coeval with rapid uplift, strike-slip movement and regional crustal thickening in the Qinling as well as retrograde metamorphism in the Sulu-Dabie. The main tectonic driver was the propagating detachment of the subducted oceanic slab at gradually shallower depth from the Sulu-Dabie to the Qinling. Stage IV (~210–190 Ma) magmatism is dominated by high silica granites derived from metasedimentary rocks. The rapid denudation rates and extensional structures indicate gravitational collapse and regional delamination of the thickened crust. In addition to the strike-slip faults and block extrusion, the Qinling is characterized by asymmetric distribution patterns of magmatism and metamorphism, different melting mechanisms over time; diachronous depositions, differential uplift and non-uniform crustal thickening, and regional delamination of the thickened orogenic root. All these features are the result of the oblique collision, which is a common process in nature, and therefore could be applied to other orogens.

© 2020 International Association for Gondwana Research. Published by Elsevier B.V. All rights reserved.

## Contents

1. Introduction . . . . .	297
2. Geological background . . . . .	298
2.1. Southern margin of the NCB . . . . .	299
2.2. North Qinling Belt . . . . .	299
2.3. South Qinling Belt . . . . .	300
2.4. Northern margin of the SCB . . . . .	302
2.5. Songpan-Ganzi Fold Belt . . . . .	302

\* Corresponding author at: School of Earth and Space Sciences, Peking University, Beijing 100871, PR China.

E-mail address: [swliu@pku.edu.cn](mailto:swliu@pku.edu.cn) (S. Liu).

2.6. Tongbai-Hong'an-Dabie-Sulu Orogenic Belt . . . . .	302
3. Geochronological and geochemical features of the early Mesozoic magmatic rocks in the Qinling Orogenic Belt . . . . .	306
3.1. Spatial and temporal distribution of early Mesozoic granitoid rocks . . . . .	306
3.2. Whole-rock geochemical and isotopic features of early Mesozoic magmatic rocks . . . . .	306
3.2.1. Andesites/diorites . . . . .	306
3.2.2. Mafic magmatic enclaves/mafic xenoliths . . . . .	307
3.2.3. Granitoid rocks . . . . .	308
4. Discussion . . . . .	309
4.1. Nature of magmatic sources and basements in the Qinling Orogenic Belt . . . . .	309
4.2. Petrogenesis of early Mesozoic magmatic rocks in the Qinling Orogenic Belt . . . . .	312
4.2.1. MME/Xenoliths/andesite-dioritic rocks . . . . .	312
4.2.2. Granitoid rocks . . . . .	312
4.3. Crust-mantle interaction during the early Mesozoic in the Qinling Orogenic Belt . . . . .	314
4.4. Crustal thickness, structural features, metamorphism, and sedimentary records during the Mesozoic and their implications for tectonic evolution . . . . .	318
4.4.1. Crustal thickness and related structural features in the Qinling Orogenic Belt . . . . .	318
4.4.2. Metamorphism in the Qinling Orogenic Belt and Tongbai-Hong'an-Dabie-Sulu Orogenic Belt during the early Mesozoic . . . . .	319
4.4.3. Sedimentation in the hinterland and foreland basin systems . . . . .	321
5. Tectonic evolution of the Qinling Orogenic Belt during the early Mesozoic . . . . .	323
5.1. Stage I . . . . .	323
5.2. Stage II . . . . .	323
5.3. Stage III . . . . .	323
5.4. Stage IV . . . . .	325
6. Critical features of oblique continental collisional orogens . . . . .	325
7. Conclusions . . . . .	326
Declaration of competing interest . . . . .	326
Acknowledgments . . . . .	326
References . . . . .	326

## 1. Introduction

Continental collisional orogens, e.g., the Alpine-Himalaya belt, are generally considered to have the following key elements: (1) a suture with possible remnant ophiolites; (2) large fold and thrust belts; (3) high-pressure (HP) to ultrahigh-pressure metamorphic (UHP) rocks; (4) a regional high-grade metamorphic terrane; (5) a migmatitic core with *in situ* crustal-derived granites; (6) crustal scale shear zones and strike-slip faults (in oblique collision zones); and (7) a flexural foreland basin (Dewey, 1977; England and Thompson, 1986; Godin et al., 2006; Harris et al., 1986; Kusky et al., 2018; S. Li et al., 2018; Streule et al., 2010; Sylvester, 1998; F.Y. Wu et al., 2008). However, extensive magmatism, especially mantle-sourced magmatism has often not been considered as a typical feature of continental collisional orogens. Apart from the classical shear heating (Harris et al., 1986; Nábělek et al., 2010) and radioactive heating (Bea, 2012) proposed for minor granite in collisional belts, the dehydration of the subducted continental lithosphere (Angiboust et al., 2017; Ducea and Chapman, 2018; Zheng et al., 2011), break-off of the subducted oceanic or continental slab (Atherton and Ghani, 2002; Chen et al., 2015; Davies and von Blanckenburg, 1995; L.Y. Zhang et al., 2014), and delamination of the lower lithosphere (Chung et al., 2005; Ducea and Saleeby, 1996; Ducea et al., 2015; Hildebrand, 2013; Lee et al., 2006) are all potential mechanisms for inducing mantle and subsequent crustal melting during continental collision. Generally, these magmatic mechanisms are related to *syn-collisional* continental subduction or post-collisional tectonic collapse, e.g., the late Caledonian granites in the British Isles, post-collisional granites in the Variscan orogen, post-collisional granites in the Carpathian, and granitoids in the Iran Zagros orogen (Chi et al., 2013; Miles et al., 2016; Segedi and Downes, 2011; Soder and Romer, 2018). Granitoids have the potential to reveal the history of early accretionary events, and later collisional events (e.g., Fu et al., 2018). It is interesting that most collisional-related magmatism, as previously stated, is related to the oblique collisional process with magmas intruding along dilation bends in the oblique collision-related faults (Chi et al., 2013; Kröner and Romer, 2013; Kusky et al., 2003; Miles et al., 2016).

Therefore, it is important to investigate the magmatism and tectonic evolution during the oblique collision process and further understand the features of such plate tectonic processes.

The Qinling Orogenic Belt of Central China is one of the most important ancient collisional belts in East Asia, which underwent three main stages of subduction-collision processes from the Precambrian to Mesozoic (Fig. 1; Dong and Santosh, 2016; Meng et al., 2019; Wu and Zheng, 2013; Zhang et al., 2001). The Qinling Orogenic Belt has been studied for over 40 years, and several review papers have been published (Dong and Santosh, 2016; Hacker et al., 2004, 2006; Hu et al., 2016a; N. Li et al., 2015; N. Li et al., 2018; S.W. Liu et al., 2011; S. Liu et al., 2015; Mattauer et al., 1985; Meng and Zhang, 1999; Meng et al., 2019; Ratschbacher et al., 2003; X. Wang et al., 2013; Wu and Zheng, 2013; Zhang et al., 2001; B.R. Zhang et al., 2002; Zhai et al., 1998). Some papers focused on the Paleozoic collision event between the North Qinling Belt and North China Block (NCB) from the regional structure, magmatism and metamorphism aspects (Bader et al., 2013; Dong et al., 2011; Ratschbacher et al., 2003; Zhai et al., 1998). Other papers reviewed the complex evolutionary history of the Qinling Orogenic Belt from the Precambrian to Mesozoic based on sedimentary, structural, metamorphism and magmatism records (Dong and Santosh, 2016; Meng et al., 2019; X. Wang et al., 2013; Wu and Zheng, 2013). However, no review papers have concentrated on the collisional process and its combined magmatic, metamorphic, structural, and sedimentary responses between the NCB and South China Block (SCB) during early Mesozoic times. Due to the widespread early Mesozoic magmatism, most studies have paid attention to the granitoid intrusions in the Qinling Orogenic Belt as clues to the collisional process (Jiang et al., 2010; N. Li et al., 2015; Qin et al., 2013; Sun et al., 2002; Yang et al., 2012a; X. Wang et al., 2013). However, the collisional process and tectonic evolution of the early Mesozoic Qinling Orogenic Belt still remain controversial. The initial collision time has been proposed at the (1) middle Triassic (Bao et al., 2015; Qin et al., 2010a, 2013; X. Wang et al., 2011; X. Wang et al., 2013); (2) late Triassic (Deng et al., 2016; Jiang et al., 2010; S.W. Liu et al., 2011; Lu et al., 2016; Yang et al., 2012a); or (3) even early Jurassic (N. Li et al., 2015). The divergence of views on the initial collision

time has, in turn, led to an array of contrasting interpretations regarding the melting mechanisms during continental collision—for example, derivations from (1) post-collisional delamination (Bao et al., 2015; Qin et al., 2010a, 2013; X. Wang et al., 2011; X. Wang et al., 2013); (2) break-off of the subducted Paleo-Tethys oceanic slab (Sun et al., 2002; Deng et al., 2016; S.W. Liu et al., 2011; Jiang et al., 2010; Yang et al., 2012a) or syn-collisional subduction of the continental crust (Lu et al., 2016); and (3) subduction of the Paleo-Tethys oceanic plate (N. Li et al., 2015). Paleomagnetic and sedimentary studies show that the collision between the NCB and SCB started at the Dabie-Sulu Orogen or even farther east in the Korean Peninsula during the late Permian to early Triassic, followed by a clockwise rotation of the SCB (Oh and Kusky, 2007; Zhao and Coe, 1987; Zhu et al., 1998; S. Liu et al., 2015; Meng et al., 2019). Therefore, the Qinling Orogenic Belt is a good example of an oblique collisional orogenesis and provides an excellent opportunity for understanding the magmatic mechanism and tectonic evolution during such collisional processes.

In this paper, we summarize published geochronological and geochemical data for 41 granitoid intrusions together with our newly obtained whole-rock geochemical and zircon U-Pb-Hf-O isotopic data for eight early Mesozoic granitoid intrusions in the Qinling Orogenic Belt. We present the temporal-spatial distribution of the early Mesozoic magmatic rocks in the Qinling Orogenic Belt and explore the petrogenesis and characteristics of magmatism during different stages. Additionally, we also review and discuss the crustal thickness in the Qinling (Hu et al., 2017a), metamorphic characteristics in the Qinling-Dabie Orogen (e.g., Liu and Liou, 2011; Wu and Zheng, 2013), depositional history in the foreland and hinterland basins along the Qinling-Dabie Orogen (e.g., Liu et al., 2005; S. Liu et al., 2015; Liu and Zhang, 2013; Meng

et al., 2019), and regional structural features in the Qinling (e.g., Ratschbacher et al., 2003; F. Wang et al., 2014). Based on these lines of evidence, we reconstruct the early Mesozoic collisional process in the Qinling Orogenic Belt, including the initial collision time, magmatic mechanism, relationship between the magmatism, metamorphism and deformation, geothermal conditions along the belt, and responses to the tectonics and sedimentation. A comprehensive tectonic model is therefore proposed attempting to reconcile all the observations and evidence presented here. The oblique collision orogenesis is evaluated and seven important features of oblique collisional belts are summarized.

## 2. Geological background

The Qinling Orogenic Belt is part of the China Central Orogenic Belt, which connects the Tongbai-Hong'an-Dabie-Sulu Orogenic Belt to the east and Kunlun Orogen to the west (Figs. 1 and 2). It is noteworthy that the absence of the early Mesozoic eclogites and extensive coeval magmatism in the Qinling Orogenic Belt are significantly different from the Dabie-Sulu orogen, which is characterized by well-preserved world-class eclogite terranes with only minor magmatism during the early Mesozoic (Fig. 2; Dong and Santosh, 2016; Wu and Zheng, 2013; Zheng, 2008; Wang et al., 2018; Zheng et al., 2018).

The Qinling Orogenic Belt is bounded by the Lingbao-Lushan-Wuyang fault in the north, and the Mianlue-Bashan-Xiangfan-Guangji fault in the south (Fig. 2; Zhang et al., 2001; B.R. Zhang et al., 2002). Three proposed sutures in the region from the north to south are: the Kuanping suture, Shangdan suture and Mianlue suture, and the four tectonic domains from the north to south are: the southern margin of the

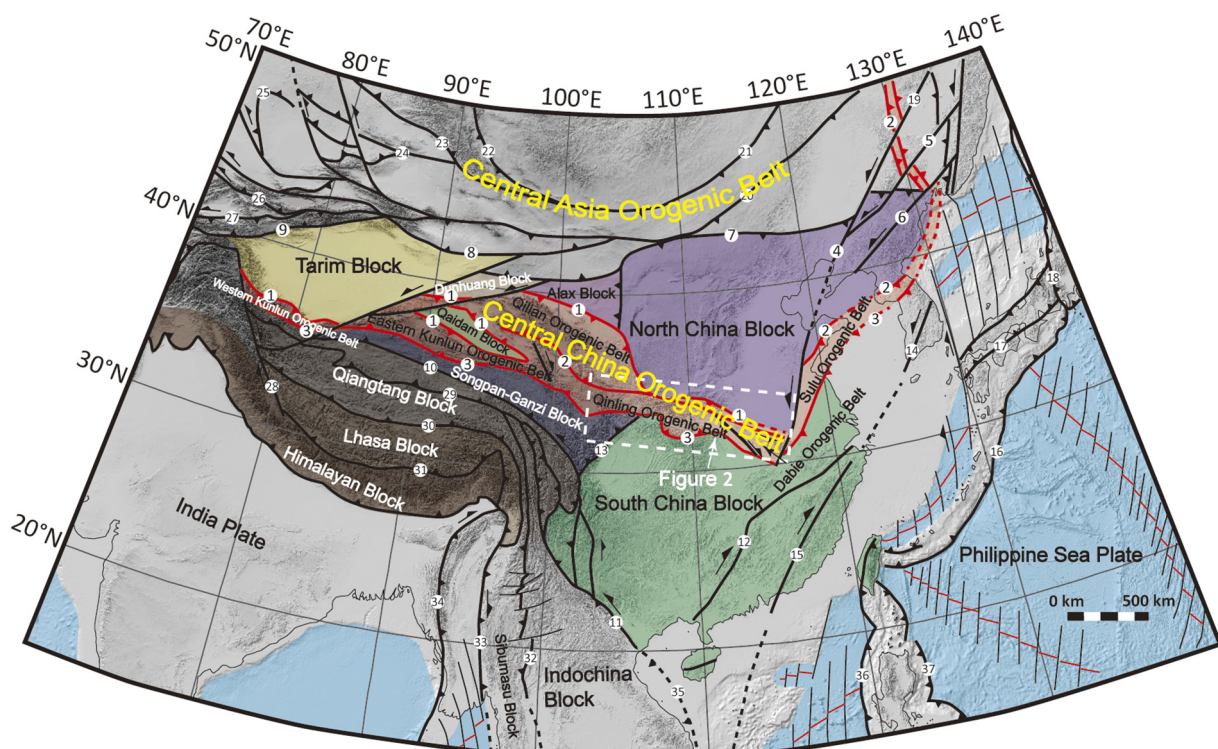


**Fig. 1.** Distribution of the major continental/micro-continental blocks in China and adjacent areas (modified after S. Li et al., 2018). The red area represents the Central China Orogenic Belt. Red and black coarse-lines are faults and sutures, representing borders between blocks or terranes. Fault names: 1. Luonan-Luanchuan Fault; 2. Shangdan Suture; 3. Mianlue-Anemaqen Suture; 4. Tanlu Fault; 5. Dunhua-Mishan Fault; 6. Yalvjiang Fault; 7. Solonker Suture; 8. Borohoro Fault; 9. Southern Tianshan Suture; 10. Jinshajiang Suture; 11. Ailaoshan-Red River Fault; 12. Jiangshan-Shaoxin Fault; 13. Longmenshan Fault; 14. Honam Fault; 15. Wuchuan-Sihui Fault; 16. Ryukyu Subduction Zone; 17. Central Japan Fault; 18. Kuril Subduction Zone; 19. Yilan-Yitong Fault; 20. Hegenshan Suture; 21. South Mongolia-Xinlinhot Suture; 22. Tuva-Mongol Orocline; 23. Erqis Suture; 24. Drbut Fault; 25. Kazakhstan Orocline; 26. North Tianshan Fault; 27. Narat Fault; 28. Karakunrum Fault; 29. Longmu Co-Shuanghu Suture; 30. Bangong Co-Nujiang Suture; 31. Indus-Yarlung Tsangpo-Lancangjiang Suture; 32. Changning-Menglian Suture; 33. Sagaing Fault; 34. Sumatra-Andaman-Sunda Subduction Zone; 35. East Vietnam Fault; 36. Manila Subduction Zone; 37. Philippine Trench.

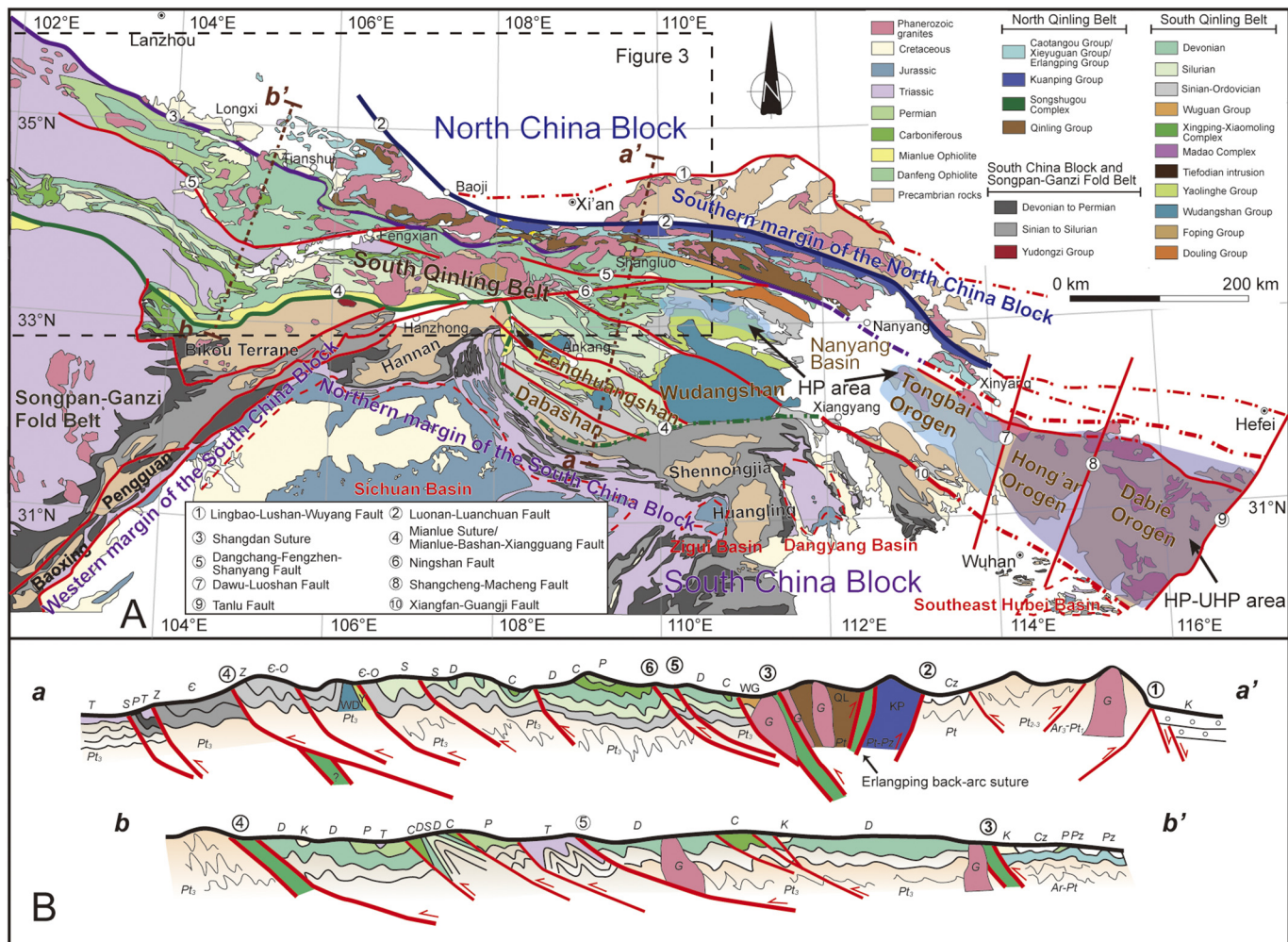


**Fig. 2.** Simplified geological map of the Qinling Orogenic Belt and adjacent area (A) and cross-section profiles (no scale) (B) (modified after Dong and Santosh, 2016; Dong et al., 2018; G.-L. Wu et al., 2014; Yan et al., 2016a; Zhang et al., 1993). The abbreviations in Fig. 2B: Ar-Archean; Pt-Proterozoic; Z-Sinian; Pz-Paleozoic; e-Cambrian; O-Ordovician; S-Silurian; D-Devonian; C-Carboniferous; P-Permian; T-Triassic; J-Jurassic; K-Cretaceous; Cz-Cenozoic; G-Granite, WD-Wudang Group; Y-Yaolinghe Group; WG-Wuguan Complex; QL-Qinling Group; KP-Kuanping Group.

NCB, North Qinling Belt, South Qinling Belt, and northern margin of the SCB (Fig. 2; Zhang et al., 2001; B.R. Zhang et al., 2002; Dong and Santosh, 2016). The Qinling Orogenic Belt was separated into the western and eastern Qinling segments along the Baocheng railway based on the different Pb isotope features of the Mesozoic granitoids and the Devonian molasse deposition only crops out in the west of the Baocheng railway (Fig. 2; Zhang et al., 2001, 2007). The Longitude 108°E is also a boundary according to geophysical data, e.g., the different Moho depths and gravity anomalies across this line (Fig. 2; Zhang et al., 2001; B.R. Zhang et al., 2002). Based on this evidence, along with the distribution of magmatism, we refine the division of the South Qinling Belt into three major zones, including western South Qinling Belt (west of 106°E longitude), middle South Qinling Belt (106°E–108°E longitude), and eastern South Qinling Belt (east of 108°E longitude) (Fig. 3).

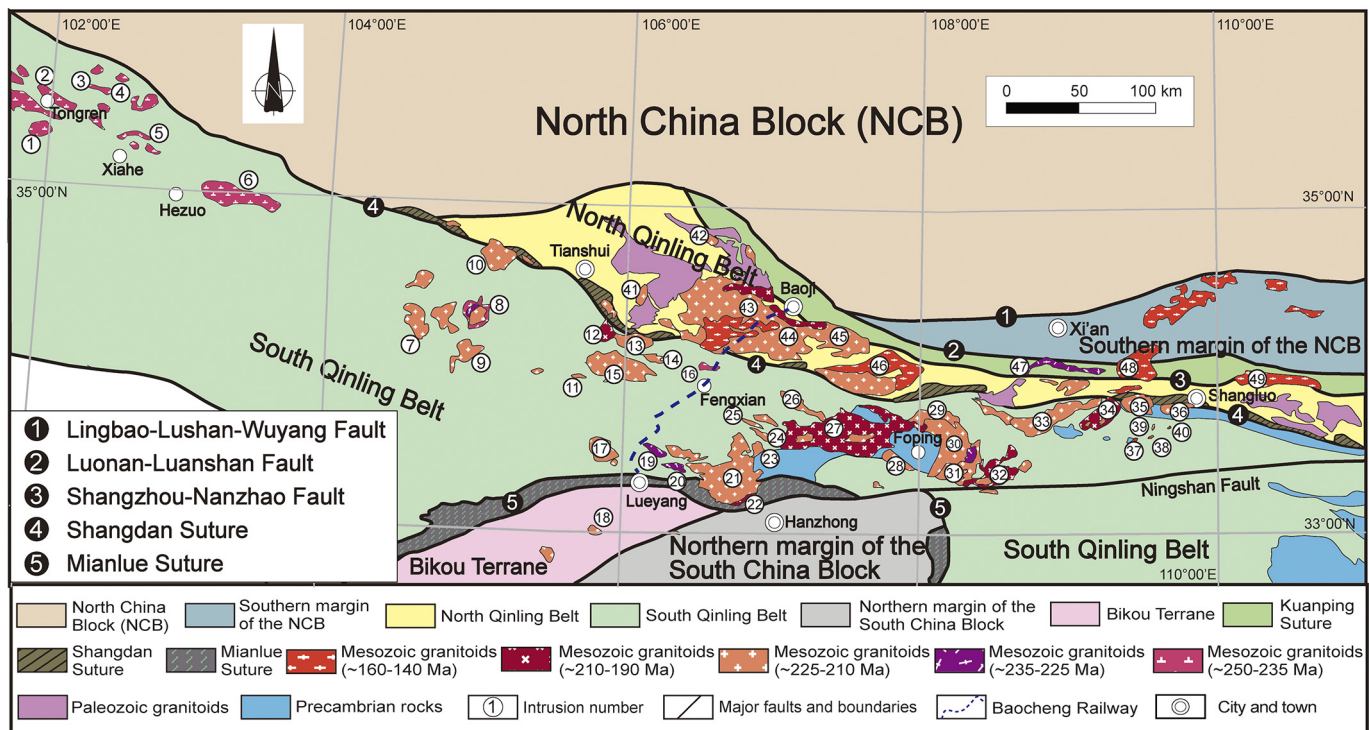
### 2.1. Southern margin of the NCB

The southern margin of the NCB is bounded by the Lingbao–Lushan–Wuyang fault and Luonan–Luanchuan fault, which consists of Precambrian rocks and Phanerozoic sedimentary cover rocks (Fig. 2). The highly deformed and metamorphosed Precambrian basement is mainly the Archean Taihua Group, consisting of biotite plagiogneiss, amphibolite, quartz schist and marble, and is overlain by Mesoproterozoic rift-related volcanic rocks (Xiong'er Group), and Meso- to Neoproterozoic

marine sedimentary rocks and uppermost Neoproterozoic tillite (Zhao et al., 2004; Shi et al., 2011). The Phanerozoic sedimentary rocks are mainly early Paleozoic (Cambrian to Ordovician) marine clastic rocks and carbonate sequences and late Paleozoic (late Carboniferous to Permian) to Mesozoic terrestrial clastic rocks (Fig. 4). All these rocks were intruded by abundant Jurassic to Cretaceous granitoid plutons (Fig. 3; N. Li et al., 2018).

### 2.2. North Qinling Belt

From north to south, the North Qinling Belt mainly comprises the Kuanping Group, Erlangping Group, and Qinling Group (main part), which are separated by southward dipping thrusts (Fig. 2; Dong et al., 2011; Dong and Santosh, 2016; Zhang et al., 2001). The Kuanping Group is mainly composed of Meso- to Neoproterozoic mafic volcanic rocks (ophiolitic unit) and late Neoproterozoic to early Paleozoic clastic rocks (sedimentary unit), which are thought to represent a Neoproterozoic or early Paleozoic suture (Diwu et al., 2010; Dong et al., 2011, 2014; Zhao et al., 2015, 2016; Cao et al., 2016; S.Z. Li et al., 2016). The early Paleozoic Erlangping (Caotangou/Xieyuguan) Group, consisting of low-grade volcanic-sedimentary sequences, has been suggested to represent a back-arc ophiolitic unit (Dong et al., 2011, 2014). The Proterozoic Qinling Group is the main basement terrane of the North Qinling Belt, consisting chiefly of felsic gneiss, amphibolite, quartz

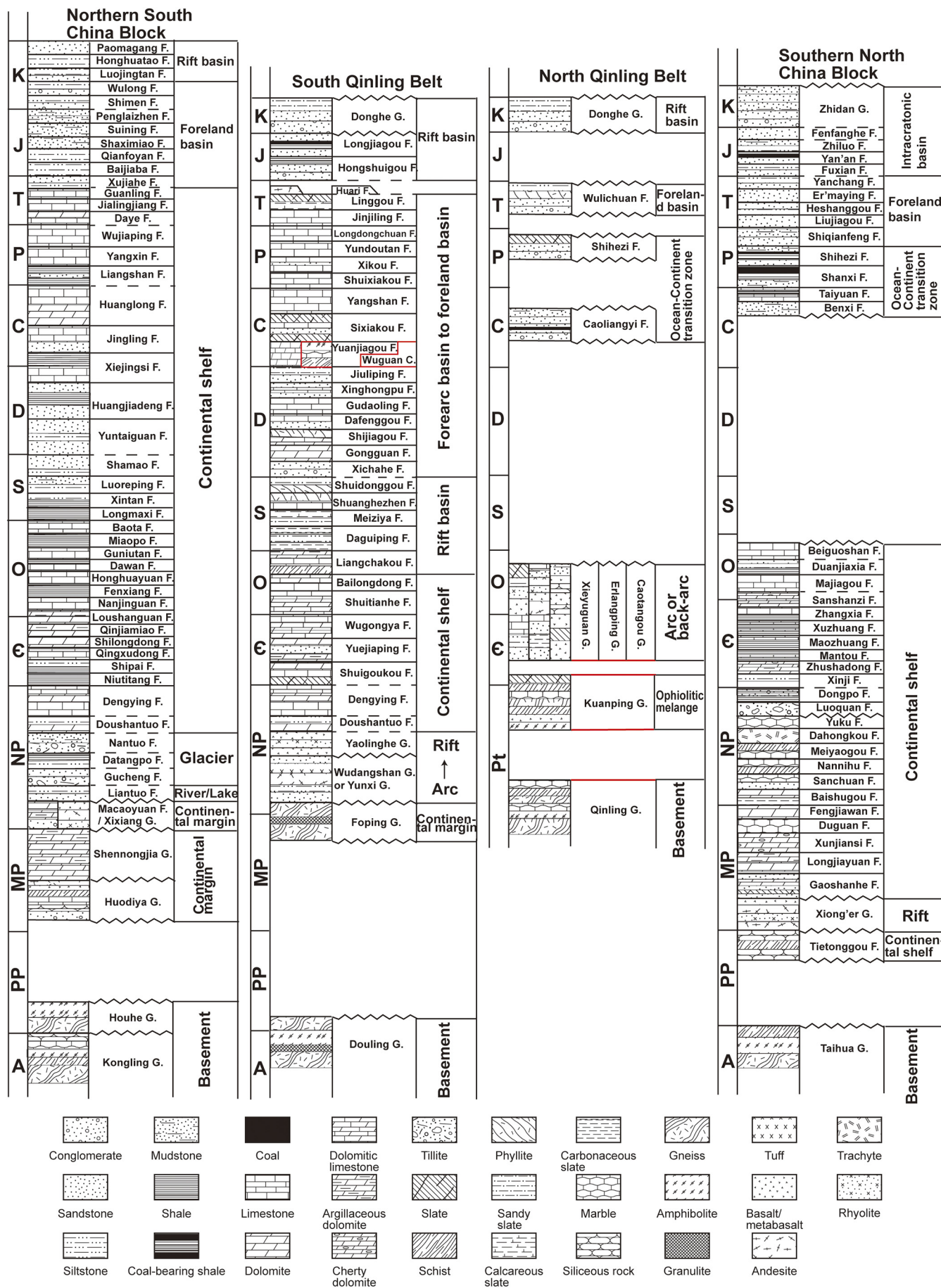


schist, and marble (Zhang et al., 2001; Z.Q. Zhang et al., 2006; Wan et al., 2011). The Songshugou Complex comprises meta-mafic and ultramafic rocks, representing an early Paleozoic ophiolite (Liu et al., 2009) or a Meso-Neoproterozoic ophiolite (Dong et al., 2008; Nie et al., 2017). The early Paleozoic Danfeng Group (~534–457 Ma) is dominantly composed of ophiolitic mélange and subduction-related volcanic-sedimentary sequences, representing the Shangdan suture zone (Dong et al., 2011). All these rocks are unconformably overlain by the discontinuously exposed Phanerozoic sedimentary strata, including the Carboniferous Caoliangyi Formation, Permian Shihezi Formation, Triassic Wulichuan Formation and Cretaceous Donghe Group, which are mainly terrestrial clastic rocks (Figs. 2 and 4). The Caoliangyi and Shihezi Formations record epicontinental deposition and the Wulichuan Formation and Donghe Group were deposited in a foreland basin (S.M. Zhang et al., 2014). The lack of the Silurian to Devonian strata in the North Qinling Belt and the southern margin of the NCB is considered to be caused by the continental collision between these two blocks during the Silurian to early Devonian (X. Liu et al., 2015; Zhao et al., 2015; Cao et al., 2016). The Paleozoic HP to UHP rocks are regionally exposed, which is also related to the collision between the North Qinling Belt and the NCC (H. Wang et al., 2011; Liu et al., 2016; Tang et al., 2016). The North Qinling Belt developed three episodes of magmatism, including: (1) Meso- to Neoproterozoic collision between the NCB and North Qinling Belt; (2) Paleozoic collision between the North and South Qinling Belt; and (3) Mesozoic collision between the SCB and NCB (Dong and Santosh, 2016; N. Li et al., 2018).

### 2.3. South Qinling Belt

The South Qinling Belt is bounded by the Shangdan suture and Mianlue suture, which are known for developing large strike-slip faults (e.g., the Ningshan fault) and northward dipping thrusts, reflecting an oblique continental collisional process (Fig. 2; Dong and Santosh, 2016; Y. Li et al., 2015; Zhang et al., 2001). The Douling Group and Foping Complex represent the crystalline basement of the South Qinling Belt. The Douling Group consists mainly of Neoarchean tonalite-trondjemite-granodiorite (TTG) assemblages, and Neoproterozoic amphibolite, quartzite, and marble (Hu et al., 2013; Shi et al., 2013; Y. Wu et al., 2014). The Proterozoic Foping Complex is composed of biotite plagiogneiss, amphibolite, hornblende gneiss and migmatite and experienced Triassic amphibolite to granulite facies metamorphism (Wang, 1997; Yang et al., 1999; Zhang et al., 2004).

Many Neoproterozoic blocks and volcanic rocks are exposed in the middle and eastern South Qinling Belt, including the Madao Complex, Xingping-Xiaomoling Complex, Tiewadian intrusion, and Yaolinghe and Wudangshan Group (Fig. 2). The ~868–765 Ma Madao Complex in the middle South Qinling Belt includes the Tangjiagou and Tiefodian granitoid gneisses (Hu et al., 2016b; Zhang et al., 2016). The Xingping-Xiaomoling Complex in the eastern South Qinling Belt exhibits a complex lithologic assemblage, including gabbro, diorite, quartz diorite, granodiorite, and monzogranite, with a long period of formation ages ranging from ~955 to ~650 Ma (Dong et al., 2017; Hu et al., 2016b; Liu, 2011; M. Yan et al., 2014). The Tiewadian intrusion in the Fenghuangshan area is mainly composed of ~740–705 Ma granitoid gneisses (Yang et al., 2012b). The Wudangshan Group (820–720 Ma) in the eastern South Qinling Belt is mainly composed of dacitic-rhyolitic lavas with minor basalt-andesite (Ling et al., 2008; L.-J. Wang



et al., 2013). The Yaolinghe Group (800–620 Ma), which is overlying the Wudangshan Group, consists mainly of metabasaltic rocks with minor meta-felsic rocks (Ling et al., 2008; L.-J. Wang et al., 2013; Zhu et al., 2014). These Neoproterozoic rocks are interpreted to have formed in a continental arc to rift-related setting (Ling et al., 2008; Hu et al., 2016b; L.-J. Wang et al., 2013; Zhang et al., 2016). No Precambrian rocks are exposed in the western South Qinling Belt, and it is mainly covered by Paleozoic and Mesozoic strata (Fig. 2; Li et al., 2013).

The Precambrian rocks are unconformably covered by Sinian marine carbonate and continuous Paleozoic sedimentary sequences, including Cambrian–Ordovician limestones, Silurian shales and Devonian–Carboniferous marine clastic rocks with interlayered limestones (Figs. 2 and 4). The Sinian to Ordovician carbonate rocks were deposited on a continental shelf, whereas the Silurian sedimentary rocks were deposited in a rift-related basin, which may be related to the separation between the South Qinling Belt and the SCB (S.M. Zhang et al., 2014; Wang et al., 2017). Devonian siliciclastic rocks are the most widespread strata in the South Qinling Belt and are proposed to have been deposited in a forearc basin related to the subduction of the Shangdan Ocean (Wang et al., 2002; Yan et al., 2006a, 2006b, 2007, 2012a, 2016a; X. Liu et al., 2015) or a foreland basin after the collision between the South and North Qinling Belts (Dong et al., 2013) (Figs. 2 and 4). The Wuguan Complex is mainly composed of late Neoproterozoic to Paleozoic quartz schist, marble and amphibolite, which was proposed to have been deposited in a forearc basin during the early Carboniferous and underwent Carboniferous and late Permian metamorphism (Fig. 2; Chen et al., 2014, 2020; Dong et al., 2018; Shi et al., 2013; Yan et al., 2009, 2016b). The Permian–Triassic sandstones with coeval volcanics are mainly exposed in the western South Qinling Belt, and only minor Permian–Triassic marine sediments are present in the eastern South Qinling Belt, which are deposited in a forearc to foreland basin (Figs. 2 and 4; Yan et al., 2016b; S.M. Zhang et al., 2014). In the South Qinling Belt, minor HP rocks formed during the Triassic are exposed in the Wudang core complex (Eide and Liou, 2000; Ratschbacher et al., 2003). Amphibolite to granulite facies rocks crop out in the Foping area and are proposed to have formed during the Late Triassic to Early Jurassic (Chen et al., 2019; Liu et al., 2019; Wei et al., 1998; Yang et al., 1999; Z.Q. Zhang et al., 2002). The magmatism in the South Qinling Belt is extensive, with most formed during the early Mesozoic, intruding into the Precambrian basement rocks and Phanerozoic strata in the South Qinling Belt (Fig. 4).

#### 2.4. Northern margin of the SCB

The northern margin of the SCB is a foreland fold-thrust belt and is separated from the South Qinling Belt by the Mianlue suture (Fig. 2). The crystalline basement includes the Neoarchean–Paleoproterozoic Kongling Group and Houhe Group. The previously defined Kongling Group is a high-grade metamorphic complex, including Archean TTG rocks and Proterozoic amphibolites, migmatites and metasedimentary rocks (S. Gao et al., 2011; Guo et al., 2014, 2015; S.-B. Zhang et al., 2006). The Paleoproterozoic Houhe Group predominantly consists of gneisses and amphibolites (Ling, 1996). The basement rocks are unconformably overlain by Meso- to Neoproterozoic marine facies sedimentary rocks and are intruded by Neoproterozoic mafic and granitoid intrusions (e.g., the Hannan Complex) (Li et al., 2003; Zhao et al., 2010). The foreland basins including the Sichuan Basin, Zigui Basin, Dangyang Basin, and Southeast Hubei Basin along the northern margin of the SCB, deposited Sinian glacial deposits and clastic-limestones,

Cambrian–Ordovician limestones, Silurian–Devonian sandstones and siltstones, Carboniferous–middle Triassic carbonate rocks, and Upper Triassic–Cretaceous clastic successions, which unconformably overly the basement rocks (Figs. 2 and 4). The lack of Devonian strata in the northern margin of the SCB may be caused by compression-related flexural bending during the collision between the SCB and South Qinling during the Mesozoic (e.g., Hu et al., 2012; Wang et al., 2019).

The Bikou Terrane, which is located at the northwestern edge of the SCB, has been proposed to be an extruded terrane and is separated from the Qinling Orogenic Belt, SCB and Songpan-Ganzi Fold Belt by thrust and strike-slip faults (Fig. 2; Li et al., 2007). The Bikou Terrane is dominated by three major lithologic units from bottom to top: 1) the Neoarchean Yudongzi Group (~2700–2660 Ma), which is composed of granitic gneiss, amphibolite, greenschist, quartzite, and banded iron formations (Zhang et al., 2001); 2) the Neoproterozoic Bikou Group (846–776 Ma), which is composed of volcanic or volcaniclastic rocks (Yan et al., 2004); and 3) the late Sinian sedimentary cover, which consists of shale, dolomite, limestone, and sandstone. All these rocks are intruded by the Triassic granitoid intrusions (Yang et al., 2015a).

#### 2.5. Songpan-Ganzi Fold Belt

The Songpan-Ganzi Fold Belt is bounded by the Qinling Orogenic Belt, the Qiangtang Block, and the SCB, which are separated by the Anemaqen suture, the Jinshajiang suture, and the Longmenshan Fault (Fig. 1). The basement is composed mainly of the Neoproterozoic granites and gneisses, which are similar to those from the western margin of the SCB, and is covered by the Sinian to Permian passive margin sequences and thick Triassic flysch (Fig. 2; Zhou et al., 2006; Roger et al., 2010; Weislogel et al., 2010). During the Triassic, northward subduction along the Anemaqen suture, southward subduction along the Jinshajiang suture, and eastward obduction along the Longmenshan Fault marked the complex collision among the Songpan-Ganzi Fold Belt, western South Qinling Belt, SCB, and the Qiangtang Block, which led to strong deformation of the Triassic flysch and passive margin sequence (e.g., Roger et al., 2010; Weislogel et al., 2010; Xu et al., 2015). After the collision, widespread granites intruded into the flysch during the Late Triassic to Early Jurassic (Roger et al., 2010; Xu et al., 2015). The magmatism was proposed to be related to the post-collisional extension/delamination (e.g., Yuan et al., 2010; Xu et al., 2015).

#### 2.6. Tongbai-Hong'an-Dabie-Sulu Orogenic Belt

The Tongbai-Hong'an-Dabie-Sulu Orogenic Belt is the eastern counterpart of the Qinling Orogenic Belt and has tectonic units corresponding to those of the Qinling Orogenic Belt (Figs. 1 and 2; Wu and Zheng, 2013; X. Liu et al., 2015). However, the metamorphic grade and magmatism are quite different from the equivalents of the South Qinling Belt (Zhang et al., 2009; Wu and Zheng, 2013; X. Liu et al., 2015). The Sulu Belt consists of UHP and HP belts, containing mainly UHP gneisses with eclogite blocks and HP schists (Zhang et al., 2009; Liu and Liou, 2011). Eclogite and their host gneisses preserved evidence of UHP metamorphism, e.g., coesite and/or quartz pseudomorphs (Katsube et al., 2009; Zhang et al., 2009; Liu and Liou, 2011). Both the Dabie and Hong'an belts contain five metamorphic belts from low-grade to UHP metamorphic belts (Zhang et al., 2009; Liu and Liou, 2011). The UHP belts in the Dabie orogen are mainly composed of gneisses with eclogite blocks/lenses, which have microdiamond-inclusions (Xu et al., 2005). Eclogite lenses/blocks in the Hong'an

**Fig. 4.** Stratigraphic columns of the Qinling Orogenic Belt and its adjacent areas (modified after 1:250,000 geological map; Dong and Santosh, 2016; Zhang et al., 1993; S.M. Zhang et al., 2014). There is no vertical scale. The black line means conformable contact; the dashed line means parallel unconformity; the jagged line means angular unconformity; and the red line means fault contact. The red star means continental collision between two adjacent blocks. Abbreviations: A-Archean; Pz-Proterozoic; PP-Paleoproterozoic; MP-Mesoproterozoic; NP-Neoproterozoic; c-Cambrian; O-Ordovician; S-Silurian; D-Devonian; C-Carboniferous; P-Permian; T-Triassic; J-Jurassic; K-Cretaceous.

**Table 1**

Summary of geological and geochemical characteristics of granitoids and related mafic rocks from early Mesozoic intrusions in the Qinling Orogenic Belt.

Intrusion	Longitude (E)	Latitude (N)	Stage	Tectonic unit	Rock type	SiO <sub>2</sub> (wt%)	Mg# <sup>a</sup>	Age	Initial <sup>87</sup> Sr/ <sup>86</sup> Sr	$\epsilon$ Nd(t)	$\epsilon$ Hf(t)	$\delta^{18}$ O	Temperature (°C) <sup>b</sup>
Xiahe	102.67	35.22	Stage I	W-SQB	ABG(+MME)	60.18–69.18	39–58	-248–244 Ma	0.70718–0.70804	-8.9–-6.2	-26.2–-4.0	688–754	
Hejiazhuang	106.56	34.00	Stage I	M-SQB	ABG(+MME)	66.60–70.00	50–58	-248 Ma		-4.8–+8.8	708–757		
Meiwu	103.08	34.98	Stage I	W-SQB	ABG + BG MME	58.46–77.10 56.72–62.08	28–70 62–65	-244–240 Ma -240 Ma	0.70685–0.70793 0.70701–0.70765	-8.5–-3.5 -7.0–-2.1	-5.4–+3.0 -4.9–0.0	672–736	
Xiekeng	102.45	35.56	Stage I	W-SQB	D + ABG	52.43–64.72	43–66	-244–242 Ma	0.70595–0.70753	-4.5–-1.1	+0.2–+5.4	682–709	
Shuangpengxi	102.33	35.56	Stage I	W-SQB	ABG	63.05–63.85	49–50	-242 Ma	0.70813–0.70853	-8.0–-7.6	-4.8–-3.5	703–726	
Tongren	101.88	35.45	Stage I	W-SQB	ABG	63.75–67.04	47–54	-241 Ma	0.70762–0.70824	-7.9–-7.5	-5.8–-0.6	682–728	
Zhongchuan	105.00	34.33	Stage I	W-SQB	ABG MME	68.61–72.50 55.52–61.03	39–41 41–46	-236 Ma -237 Ma		-15.7–0.0 -13.4–+4.0		713–756	
Maixiu	105.00	34.33	Stage I	W-SQB	A	53.75–57.29	46–69	-234 Ma	0.70782–0.71226	-9.3–-7.7			
Wulong	108.25	33.50	Stage II	E-SQB	ABG(+MME)	60.65–67.97	50–63	-233–227 Ma	0.70494–0.70662	-6.8–-3.6	-12.8–+2.8	671–730	
Zhongchuan	105.00	34.33	Stage II	W-SQB	ABG	67.61–71.00	38–39	-232 Ma			-14.5–-2.0	720–763	
Zhangjiaba	106.34	33.45	Stage II	M-SQB	ABG MME	58.92–71.11 52.98–54.36	49–63 58–59	-230 Ma -230 Ma			-5.4–-3.2	683–749	
Xinyuan	106.22	33.50	Stage II	M-SQB	ABG MME	63.35–69.57 52.40–56.85	38–51 50–57	-229 Ma -229 Ma			-10.1–2.5 -6.3–-4.6	694–751	
Cuihuashan	108.85	33.95	Stage II	NQB	BG	69.20–72.03	32–38	-227 Ma	0.70309–0.70422	-2.0–-0.2	-2.8–+0.2	688–762	
Zhashui	109.25	33.63	Stage III	E-SQB	ABG(+MME)	69.61–71.56	40–43	-225 Ma			-5.7–+4.4	704–741	
Wenquan	105.25	34.60	Stage III	W-SQB	ABG + BG MME	65.21–73.19 52.90–60.50	26–52 52–72	-225–216 Ma -218 Ma	0.70634–0.70759	-5.5–-5.0	-3.5–-1.8	703–778	
Caoping	109.50	33.78	Stage III	E-SQB	ABG + BG MME	60.11–73.20 50.02–65.18	36–65 41–71	-224–213 Ma -216 Ma	0.70424–0.70567 0.70457–0.70520	-3.0–-0.6 -2.5–-0.3	-8.6–+6.8 +0.5–+3.5	4.4–6.0	694–747
Guangtoushan	106.67	33.43	Stage III	M-SQB	BG + TMG	68.23–76.80	27–47	-224–218 Ma	0.70490–0.70960	-3.7–-1.6	-14.6–1.4	683–785	
Yanzhiba	108.50	33.42	Stage III	E-SQB	ABG + TMG	65.30–74.35	6–57	-222–211 Ma	0.70413–0.70663	-12.7–-3.6	-3.5–+7.7	685–753	
Dongjiangkou	108.98	33.75	Stage III	E-SQB	ABG MME(+Mafic dike)	62.83–69.42 50.48–64.66	56–66 47–75	-221–214 Ma -223–217 Ma	0.70412–0.70673 0.70477–0.70589	-8.0–-3.9 -6.3–-0.7	-25.5–+3.3 -17.7–+13.2	6.1–10.0 5.7–7.3	682–762
Laocheng	108.35	33.50	Stage III	E-SQB	ABG(+MME)	62.10–72.90	36–65	-221–210 Ma	0.70413–0.70533	-5.6–-2.4	-14.5–+9.0	651–773	
Lüjing	104.60	34.28	Stage III	W-SQB	BG	66.92–77.58	16–42	-221 Ma				714–775	
Zhongchuan	105.00	34.33	Stage III	W-SQB	ABG MME	68.35–75.28 53.92–64.61	29–47 37–48	-220–216 Ma -219 Ma	0.70528–0.71042 0.70695	-7.1 -4.7	-6.7–+2.2 -0.8	703–767	
Xiba	107.20	33.67	Stage III	M-SQB	ABG MME	61.55–71.10 56.10	51–61 55	-219 Ma -218 Ma	0.70619–0.70821 0.70607	-8.6–-5.4 -7.1	-28.2–+0.6	661–760	
Wulong	108.25	33.50	Stage III	E-SQB	ABG MME	69.16–71.05 46.97–58.70	37–41 41–65	-218 Ma -220 Ma	0.70443–0.70627	-6.4–-2.2 -10.1–+2.0	-10.2–+9.9 -10.1–+2.0	702–752	

(continued on next page)

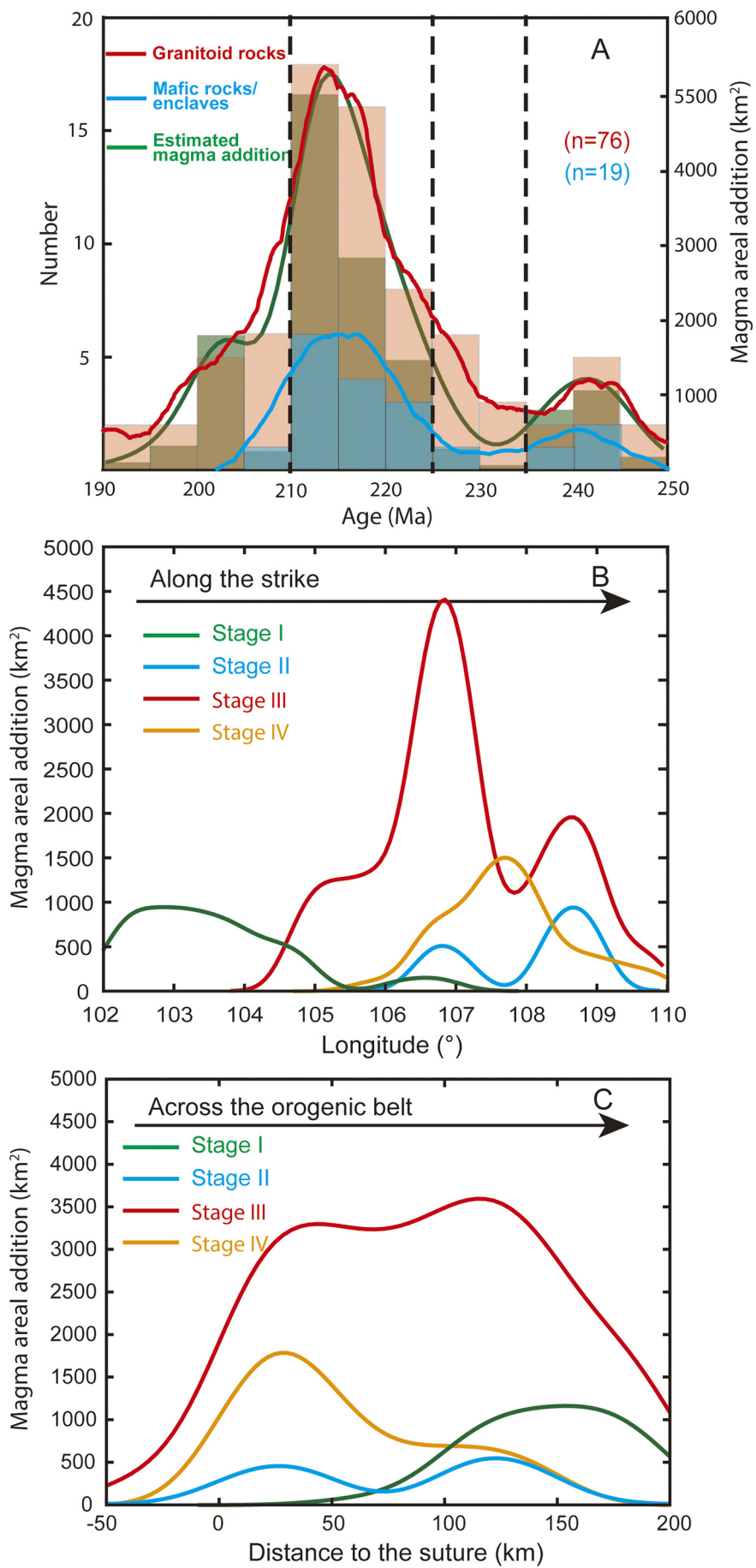
**Table 1** (continued)

Intrusion	Longitude (E)	Latitude (N)	Stage	Tectonic unit	Rock type	SiO <sub>2</sub> (wt%)	Mg# <sup>a</sup>	Age	Initial <sup>87</sup> Sr/ <sup>86</sup> Sr	$\varepsilon$ Nd(t)	$\varepsilon$ Hf(t)	$\delta^{18}$ O	Temperature (°C) <sup>b</sup>
Longcaoping	107.98	33.75	Stage III	E-SQB	D	55.20–57.69	41–49	~217 Ma					
Taoyuanpu	106.82	33.69	Stage III	M-SQB	ABG(+MME)	61.97–68.63	51–63	~216 Ma			−19.5–−4.7		653–709
Huosaodian	106.93	33.53	Stage III	M-SQB	ABG(+MME)	58.37–74.32	28–66	~215 Ma			−9.2–−4.2		697–734
Jiangjiaping	106.37	33.48	Stage III	M-SQB	TMG	74.30–75.45	16–36	~215 Ma			−7.0–−5.2		755–765
Mishuling	105.75	34.03	Stage III	M-SQB	ABG	60.96–65.12	41–47	~215–213 Ma	0.70677–0.70739	−9.2–−5.8	−12.5–+4.8		702–773
					MME	51.91–59.10	47–61	~212 Ma	0.70702–0.70709	−6.5–−6.4	−1.6–+5.2		
Shahewan	109.71	33.78	Stage III	E-SQB	ABG	63.76–70.00	46–68	~214–210 Ma	0.70516–0.70590	−3.4–−0.6	−6.0–+5.0	4.8–5.4	666–776
					MME	50.50–58.35	47–68	~214–210 Ma	0.70528–0.70531	−1.8–−1.1	−8.8–+6.1		
Huayang	107.38	33.55	Stage III	M-SQB	BG	62.27–68.95	38–55	~214–210 Ma			−8.7–+2.1	5.3–9.0	680–790
					Mafic xenolith	46.90–49.85	68–73	~218–213 Ma			−6.8–+4.4	5.9–6.4	
Huangzhuguan	105.65	33.95	Stage III	W-SQB	ABG	62.44–73.32	48–59	~214 Ma					671–687
Xichahe	107.75	33.47	Stage III	M-SQB	D	56.98–64.40	53–67	~212 Ma	0.70547–0.70646	−3.7–−1.6			628–711
Liuba	106.93	33.61	Stage III	M-SQB	D + ABG	56.16–63.59	58–65	~211 Ma	0.70825–0.70961	−8.4–−3.8	−17.7–−3.8		
					MME			~215 Ma	0.70802	−7.3			
Miba	105.83	34.50	Stage III	W-SQB	ABG	58.19–68.85	40–61	~211 Ma					656–736
					MME	51.81–58.06	59–63	~211 Ma					
Luchuba	105.00	34.08	Stage III	W-SQB	ABG	64.15–71.29	46–57	~211 Ma	0.70793–0.70853	−6.8–−5.8	−2.9–−1.8		685–733
Qinlingliang	107.20	34.25	Stage III	NQB	ABG	64.80–65.00	50–51	~210 Ma	0.70595–0.70603	−4.4–−4.2	−7.5–−1.0		701–735
					MME	55.00–57.00	57–62	~211 Ma	0.70599–0.70612	−5.5–−4.0	−7.2–−2.6		
Laojunshan	107.67	34.15	Stage III	NQB	ABG	65.00–66.28	47–50	~214 Ma	0.70605–0.70631	−4.3–−4.2			686–712
					MME	49.20–62.50	56–68	~214 Ma	0.70460–0.70608	−3.4–−3.2			
Baoji	107.33	34.20	Stage III	NQB	D + ABG + BG	53.20–75.33	24–67	~217–210 Ma	0.70497–0.70830	−12.6–−2.5	−13.4–+5.3		712–785
Shimen	106.12	34.39	Stage III	NQB	BG	74.45–78.83	33–42	~220 Ma					730
Guanshan	106.67	34.77	Stage III	NQB	BG	67.79–74.55	29–49	~225 Ma			−6.6–−0.8		719–755
Yanzhibia	108.50	33.42	Stage IV	E-SQB	BG + TMG	70.99–77.30	16–83	~209–201 Ma			−6.4–+5.9		710–761
Wulong	108.25	33.50	Stage IV	E-SQB	ABG	63.84–71.30	38–49	~208 Ma	0.70444–0.70522	−5.6–−3.1	−8.4–+3.2		713–780
					MME	52.86–55.78	51–66	~208 Ma					
Yangba	105.8	33.1	Stage IV	Bikou	ABG	66.60–69.08	51–54	~207 Ma	0.70521–0.70611	−4.4–−3.3	−9.3–+3.9		704–718
					MME	56.39–61.33	55–60	~208 Ma	0.70517–0.70570	−3.8	−11.0–+8.2		
Longcaoping	107.97	33.67	Stage IV	E-SQB	BG	67.07–75.81	32–44	~207–189 Ma					702–779
Huayang	107.38	33.60	Stage IV	M-SQB	BG	64.30–76.70	2–51	~210–194 Ma			−14.7–+1.9	5.2–9.3	703–862
Zhashui	109.15	33.67	Stage IV	E-SQB	ABG(+MME)	68.33–72.22	34–55	~204–199 Ma	0.70445–0.70589	−4.8–−4.1	−3.5–+7.6	4.7–5.7	694–768
Erdaohexiang	106.83	33.27	Stage IV	M-SQB	ABG	59.61–67.73	52–59	~202 Ma			−10.1–−5.0		694–730
Baoji	107.00	34.25	Stage IV	NQB	BG	71.61–76.29	19–29	~206–190 Ma	0.70701–0.71216	−17.1–−5.5	−18.7–+4.3		725–796

Abbreviation: W-SQB, West South Qinling Belt; M-SQB, Middle South Qinling Belt; E-SQB, East South Qinling Belt; NQB, North Qinling Belt; MME, Mafic magmatic enclave; D, diorite; A, Andesite; ABG, Amphibole-bearing granitoid; BG, Biotite granite; TMG, Two-mica granite.

<sup>a</sup> Mg# = 100 Mg/(Mg + Fetotal) in atomic ratio.

<sup>b</sup> Temperature calculation is after Boehnke et al. (2013).



occur within gneiss in the HP-UHP belts, and minor coesite inclusions in garnet are present (Zhang and Liou, 1996; Zhang et al., 2009). The Tongbai Block contains two orogenic systems including the northern Paleozoic and the southern Mesozoic orogenic systems, which correspond to the North Qinling Belt and Hong'an Block, respectively (Wu and Zheng, 2013; X. Liu et al., 2015). Instead of the UHP metamorphic signatures, the Tongbai Complex is mainly composed of late Mesozoic granite with metamorphic enclaves of Neoproterozoic gneisses, marble and retrograde HP eclogites (Liu et al., 2010; X. Liu et al., 2015). All the HP-UHP gneisses and eclogites show Neoproterozoic protolith ages and Triassic metamorphic ages (Ames et al., 1996; Ayers et al., 2002; Cheng et al., 2011; Feng et al., 2020; Liu and Liou, 2011; Schmidt et al., 2008, 2011; Wang et al., 2010; L. Wang et al., 2014; Xia et al., 2018; Zhang et al., 2009; Zheng et al., 2018; Zhou et al., 2015). The basement in the Tongbai-Hong'an-Dabie-Sulu Orogenic Belt was intruded by late Mesozoic granites with more enriched Sr-Nd-Hf isotopic compositions compared to the early Mesozoic granites in the Qinling Orogenic Belt (Fig. 2; Chen et al., 2002; Hu et al., 2018; X. Wang et al., 2013; Zhao et al., 2017). These granites were formed in a post-collisional setting (e.g., Zhao et al., 2017), or related to delamination caused by the subduction of the Pacific Ocean (e.g., Huang et al., 2008; Zhu et al., 2018).

### 3. Geochronological and geochemical features of the early Mesozoic magmatic rocks in the Qinling Orogenic Belt

New whole-rock geochemical and zircon U-Pb-Hf-O isotopic data and published data on the whole-rock geochemistry and whole-rock Sr-Nd isotopes of granitoid intrusions in the Qinling Orogenic Belt are presented in Supplementary Information 1. A description of the analytical methods, cathodoluminescence (CL) images of zircons, and zircon U-Pb concordia diagrams from this study are presented in Supplementary Information 2. The compiled data on the Hf-O isotopes and formation ages of mafic rocks and granitoid rocks in the Qinling Orogenic Belt are presented in Supplementary Information 3 and 4, respectively. The whole-rock geochemical data were carefully screened for possible alteration (e.g., high loss on ignition samples). A simplified summary of granitoid intrusions in the Qinling Orogenic Belt, including their sample locations, petrological features, geochemical data, whole-rock Sr-Nd isotopes, zircon Hf-O isotopes, and U-Pb ages, is compiled and are presented in Table 1. We calculated the Zr saturation temperature of granitoids according to Boehnke et al. (2013).

#### 3.1. Spatial and temporal distribution of early Mesozoic granitoid rocks

Early Mesozoic granitoid intrusions are widespread in the Qinling Orogenic Belt, mainly in the South Qinling Belt (Fig. 3). According to our compilation, the early Mesozoic magmatism has two magmatic peaks, including ~250–235 Ma (Peak I) and 225–210 Ma (Peak II) (Fig. 5). Based on a magmatic lull during ~235–225 Ma and a lack of mafic magma during ~210–190 Ma, the early Mesozoic tectonic stages may be divided into four stages, including Stage I (~250–235 Ma), Stage II (~235–225 Ma), Stage III (~225–210 Ma), and Stage IV (~210–190 Ma) (Fig. 5A). On the basis of the exposure of these granitoid intrusions, we estimate the amount of magma addition during the early Mesozoic. The result is consistent with the age probability density plot, indicating that the age populations for the Qinling orogen intrusions reflect the magmatic flux through time (Fig. 5A).

The spatial distribution of the granitoid intrusions in the Qinling Orogenic Belt show time-dependent features (Figs. 3 and 5). The Stage I magmatism (~250–235 Ma) mainly occurred in the western South

Qinling Belt, with the exception of the Hejiazhuang intrusion outcrops in the middle South Qinling Belt (Yang et al., 2014). The outcrop area of Stage I magmatism was ~2000 km<sup>2</sup> (Fig. 5A). The magmatic intensity of the Stage II (~235–225 Ma) was extremely low, with an exposed area of only ~400 km<sup>2</sup>, and the granitoid intrusions are sporadically distributed in the Qinling Orogenic Belt (Fig. 5A). Intense magmatism was generated in the Qinling Orogenic Belt during the Stage III (~225–210 Ma), with an outcrop area of ~10,000 km<sup>2</sup> (Fig. 5A). The Stage IV magmatism (~210–190 Ma) has an exposed area of ~2500 km<sup>2</sup> and outcrops mainly in the middle and eastern South Qinling Belt (Fig. 5A). The spatial distribution of granitoid intrusions suggests that early Mesozoic magmatism migrated from the west to the east and from north to south (Fig. 5B and C).

#### 3.2. Whole-rock geochemical and isotopic features of early Mesozoic magmatic rocks

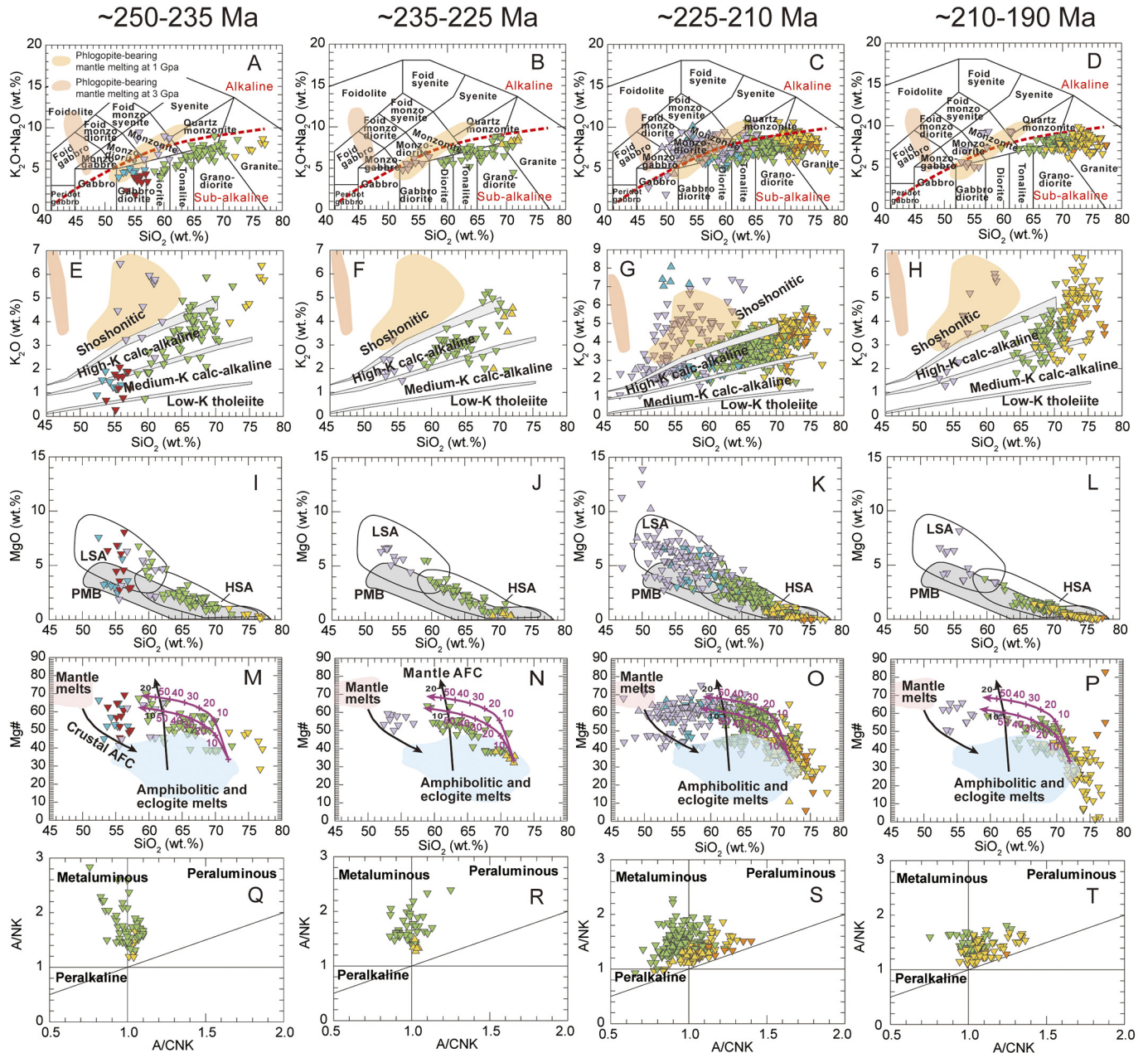
The early Mesozoic magmatic rocks in the Qinling Orogenic Belt may be divided into three categories of andesite/diorite, granitoid, and mafic magmatic enclaves (MME)/xenoliths (Table 1). The granitoids can be further subdivided into amphibole-bearing granitoids, biotite granite, and two-mica granite (Table 1). The same rock type shows similar geochemical features. Stage I is characterized by andesite/diorite and amphibole-bearing granitoids with MME and minor biotite granite. Stage II magmatic rocks are mainly amphibole-bearing granitoids with MME and biotite granite. Stage III is characterized by abundant amphibole-bearing granitoids with MME and minor diorite, biotite granite and two-mica granite. Stage IV magmatic rocks are mainly biotite granite and amphibole-bearing granitoids with minor two-mica granite and MME.

##### 3.2.1. Andesites/diorites

The andesites and diorites are rare in the Qinling Orogenic Belt. The Maixiu andesites in the western South Qinling Belt belong to medium-K calc-alkaline series and have intermediate SiO<sub>2</sub> contents (53.75–57.29 wt%), medium to high MgO contents (2.78–8.05 wt%) and Mg# values (46–69) (Fig. 6A, E, I and M; Li et al., 2013). The andesites are characterized by slightly steep REE patterns normalized by chondrite with medium (La/Yb)<sub>N</sub> ratios (5.46–9.38) and weak negative Eu anomalies (Eu/Eu\* = 0.73–0.94) (Fig. 7A; Li et al., 2013). These andesites have high Cr contents (133–797 ppm) and are enriched in large ion lithophile elements (LILE) (e.g., Rb, Ba, and Sr), and display negative Nb-Ta anomalies and negative P anomalies in primitive mantle-normalized multi-element patterns (Fig. 8A; Li et al., 2013). The andesites all have low εNd(t) values (−9.3 to −7.7) and high (<sup>87</sup>Sr/<sup>86</sup>Sr)<sub>i</sub> ratios (0.70787 to 0.71226) (Fig. 9B; Li et al., 2013).

Some dioritic rocks are associated with granitoids (Baoji, Liuba, Longcaoping, Xichahe, and Xiekeng) in the Qinling Orogenic Belt and have intermediate SiO<sub>2</sub> contents (52.43–64.40 wt%) and medium to high-K calc-alkaline features, except for the Baoji dioritic rocks (appinites), which have a shoshonitic feature (Fig. 6A, C, E and G). Most of them have high MgO contents (2.50–7.62 wt%) and Mg# values (41–67) (Fig. 6I, K, M, and O). The calc-alkaline diorites exhibit weakly to strongly steep chondrite-normalized REE patterns with variable (La/Yb)<sub>N</sub> ratios (3.09–22.52) and negative to positive Eu anomalies (0.67–1.14) (Fig. 7A and B). In primitive mantle-normalized multi-element patterns, the dioritic rocks are enriched in LILE with negative Nb-Ta anomalies and negative P anomalies (Fig. 8A and B). Some calc-alkaline diorites (Xiekeng, Xichahe) exhibit low to medium (<sup>87</sup>Sr/<sup>86</sup>Sr)<sub>i</sub> ratios (0.70547 to 0.70753) and slightly negative εNd(t) values

**Fig. 5.** Temporal-spatial distribution of early Mesozoic magmatic rocks in the Qinling Orogenic Belt. (A) Histograms and probability density plots of the crystallization ages of the granitoid rocks and mafic rocks/MME formed during the early Mesozoic from the Qinling Orogenic Belt. To minimize the sampling bias, only one age datum is selected for each pluton if the between-sample age difference is lower than 3 Myr. Magma addition is also estimated based on the distribution area of granitoid intrusions in the Qinling Orogenic Belt during the early Mesozoic. The data of the early Mesozoic magmatic rocks are cited from the Table 1 and Supplementary Information 4. (B) Estimated magma additions of different stages along the strike during the early Mesozoic. (C) Estimated magma additions of different stages across the orogenic belt during the early Mesozoic. The suture represents the Mianlue suture.



North Qinling Belt: ▲ MME/mafic xenolith ▲ diorite ▲ amphibole-bearing granitoid ▲ biotite granite

South Qinling Belt: ▼ MME/mafic xenolith ▼ andesite ▼ diorite ▼ amphibole-bearing granitoid ▼ biotite granite ▼ two-mica granite

**Fig. 6.** Geochemical features of the major elements of the granitoids and mafic rocks formed during different stages in the Qinling Orogenic Belt. (A-D) Total alkali versus  $\text{SiO}_2$  diagram (after Middlemost, 1994); (E-H)  $\text{K}_2\text{O}$  versus  $\text{SiO}_2$  diagram (after Rollinson, 1993); (I-L)  $\text{MgO}$  versus  $\text{SiO}_2$  diagram (after Martin et al., 2005); (M-P)  $\text{Mg}\#$  versus  $\text{SiO}_2$  diagram (after Stern and Kilian, 1996); (Q-T)  $\text{A}/\text{NK}$  (molar  $\text{Al}_2\text{O}_3/(\text{Na}_2\text{O} + \text{K}_2\text{O})$ ) versus  $\text{A}/\text{CNK}$  (molar  $\text{Al}_2\text{O}_3/(\text{CaO} + \text{Na}_2\text{O} + \text{K}_2\text{O})$ ) diagram (after Maniar and Piccoli, 1989). The data are cited from Supplementary Information 1. The ranges of phlogopite-bearing mantle melting melts are from Condamine and Médard (2014) and Condamine et al. (2016). In the  $\text{Mg}\#$  versus  $\text{SiO}_2$  diagram, the field of melts derived from the partial melting of amphibolitic rocks and eclogites were obtained in experimental studies (Rapp and Watson, 1995; Rapp et al., 1999; Smithies, 2000; Sisson et al., 2005). The mixing trends illustrate mixing between MME and granitoid rocks starting with the monzogranite sample from the Zhashui intrusion and MME samples published by X. Wang et al. (2011) and Jiang et al. (2012).

(−4.5 to −1.1) (Fig. 9B). The Liuba diorites have strongly negative  $\epsilon\text{Hf(t)}$  values (−17.7 to −3.8) (Fig. 9B). As for the shoshonitic diorites, they have very steep chondrite-normalized REE patterns with high  $(\text{La/Yb})_N$  ratios (15.78–29.21) and negative to positive Eu anomalies (0.67–1.14) (Fig. 7B). These samples are extremely enriched in LILE, especially Ba, and show negative Nb-Ta anomalies in primitive mantle-normalized multi-element patterns (Fig. 8B). Concerning isotopic features, they have quite a large range of  $\epsilon\text{Hf(t)}$  values (Fig. 10C; −12.7 to +5.3).

### 3.2.2. Mafic magmatic enclaves/mafic xenoliths

The mafic magmatic enclaves/mafic xenoliths are characterized by low to intermediate  $\text{SiO}_2$  contents (46.90–65.18 wt%) and high-K calc-alkaline to shoshonitic features (Fig. 6A–H). These low- $\text{SiO}_2$  mafic rocks exhibit variable  $\text{MgO}$  contents (1.05–13.91 wt%) and  $\text{Mg}\#$  values (37–75) (Fig. 6I–P). Most mafic rocks show steep chondrite-normalized REE patterns with high  $(\text{La/Yb})_N$  ratios (most of 3.30–26.88) and moderately negative to no Eu anomalies (most of 0.56–1.04) (Fig. 7C–F). In

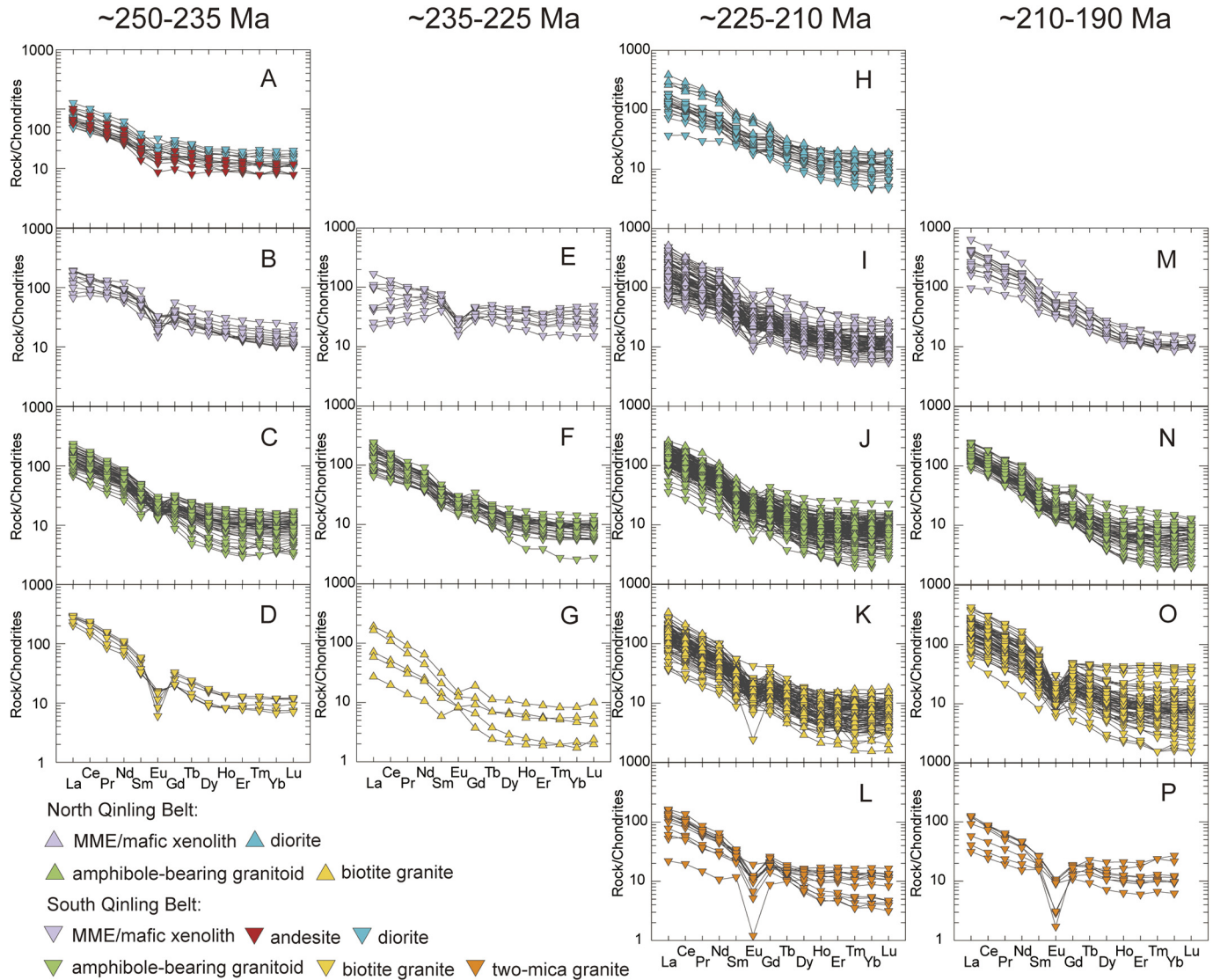


**Fig. 7.** Chondrite-normalized REE diagrams for the granitoids and mafic rocks formed during different stages in the Qinling Orogenic Belt (normalizing values after Sun and McDonough (1989)). (A–D) Magmatic rocks formed during Stage I; (E–G) Magmatic rocks formed during Stage II; (H–L) Magmatic rocks formed during Stage III; (M–P) Magmatic rocks formed during Stage IV..

the primitive mantle-normalized multi-element diagrams, they are all enriched in LILE and have negative Nb-Ta-P-Ti anomalies (Fig. 8C–F). Their  $(^{87}\text{Sr}/^{86}\text{Sr})_i$  ratios are 0.70457 to 0.70802, the  $\epsilon\text{Nd(t)}$  values are  $-7.3$  to  $-0.3$ , the  $\epsilon\text{Hf(t)}$  values are between  $-17.7$  and  $+13.2$ , and the  $\delta^{18}\text{O}$  values are  $+5.66$  to  $+7.32$  (Figs. 9–11).

### 3.2.3. Granitoid rocks

The amphibole-bearing granitoids exhibit intermediate to high  $\text{SiO}_2$  contents (58.19–74.32 wt%) and belong to a high-K calc-alkaline series with metaluminous to peraluminous signatures ( $A/\text{CNK} = 0.66$ –1.27) (Fig. 6E–H and Q–T). Most amphibole-bearing granitoids have medium to high  $\text{MgO}$  contents (0.19–6.82 wt%) and  $\text{Mg}\#$  values (28–70) (Fig. 6I–P). These samples all display steep chondrite-normalized REE patterns with generally high  $(\text{La/Yb})_N$  ratios (6.82–73.63) and moderately negative to slightly positive Eu anomalies (most between 0.59 and 1.10) (Fig. 7G–J). These samples have similar primitive mantle-normalized multi-element patterns which are enriched in LILE and negative Nb-Ta-P-Ti anomalies (Fig. 8G–J). These amphibole-bearing granitoids have variable isotopic features, such as  $(^{87}\text{Sr}/^{86}\text{Sr})_i$  ratios of 0.70412

to 0.70961,  $\epsilon\text{Nd(t)}$  values of  $-9.2$  to  $-0.6$ ,  $\epsilon\text{Hf(t)}$  values of  $-37.2$  to  $+9.9$ , and  $\delta^{18}\text{O}$  values of  $+4.75$  to  $+10.01$  (Figs. 9–11).

The biotite granites and two-mica granites show similar geochemical features. These granites are characterized by a high  $\text{SiO}_2$  content (64.44–78.83 wt%), high-K calc-alkaline to shoshonitic characteristics, and from metaluminous to mainly peraluminous features (0.78–2.39) (Fig. 6E–H, Q–T). These high- $\text{SiO}_2$  rocks show generally low  $\text{MgO}$  contents (0.01–1.74 wt%) and  $\text{Mg}\#$  (2–55, except for one sample with abnormally high  $\text{Mg}\#$  value of 83, due to an extremely low  $\text{TiO}_2$  content) (Fig. 6I–P). These samples display relatively flat to steep chondrite-normalized REE patterns with variable  $(\text{La/Yb})_N$  ratios (1.46–88.89) and commonly weak to strong negative Eu anomalies (most are 0.28–0.96) (Fig. 7K–P). In the primitive mantle-normalized multi-element diagrams, biotite granites and two-mica granites are uniformly enriched in LILE and showed distinct negative Nb-Ta-P-Ti anomalies (Fig. 8K–P). These biotite granites and two-mica granites also have variable isotopic features, including  $(^{87}\text{Sr}/^{86}\text{Sr})_i$  ratios of 0.70309 to 0.71216,  $\epsilon\text{Nd(t)}$  values of  $-17.7$  to  $-0.2$ ,  $\epsilon\text{Hf(t)}$  values of  $-18.7$  to  $+5.9$ , and  $\delta^{18}\text{O}$  values of  $+5.22$  to  $+9.25$ , with a more enriched signature than that of amphibole-bearing granitoid (Figs. 9–11).

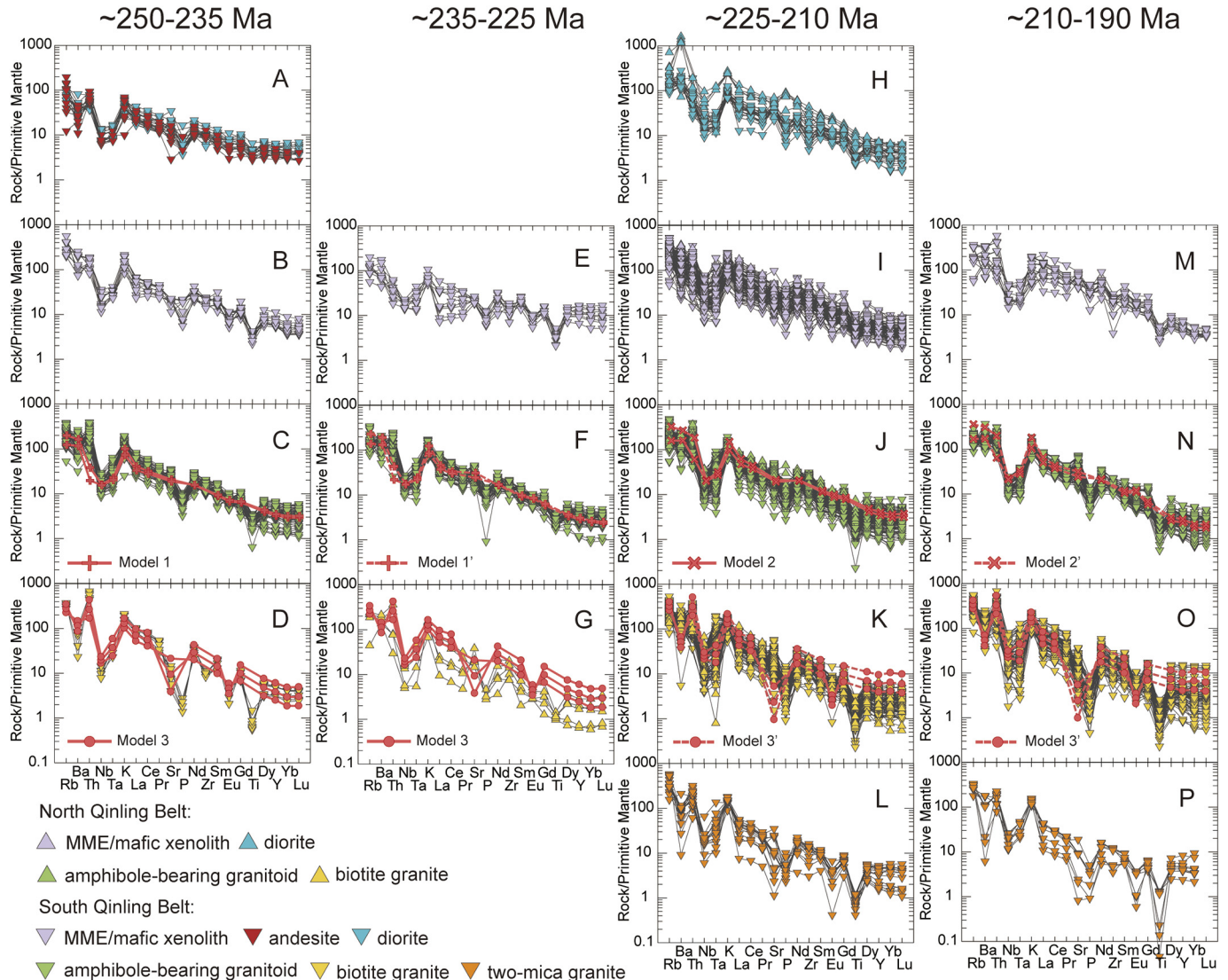


**Fig. 8.** Primitive mantle-normalized trace element spider diagrams for the granitoids and mafic rocks formed during different stages in the Qinling Orogenic Belt (normalizing values after Sun and McDonough (1989)). (A–D) Magmatic rocks formed during Stage I; (E–G) Magmatic rocks formed during Stage II; (H–L) Magmatic rocks formed during Stage III; (M–P) Magmatic rocks formed during Stage IV. The calculated models are shown in the Table 2. The calculated melts of Model 1 and Model 1' show a mixing ratio of 6:4 between felsic melts and mantle-derived melts (MME) with different residual minerals and melting degrees, as the source rock is 08LY2-14. The calculated melts of Model 2 and Model 2' show a mixing ratio of 8:2 between felsic melts and mantle-derived melts (MME) with different residual minerals and melting degrees, as the source rock is 08LY2-8. The calculated melts of Model 3 (starting material of 16HY06-3) and Model 3' (starting material of 14HY04-3) show fractionated melts. The source rocks and starting materials are from Hu et al. (2016b, 2018). The MME is the lowest-SiO<sub>2</sub> MME sample published by Jiang et al. (2012).

#### 4. Discussion

##### 4.1. Nature of magmatic sources and basements in the Qinling Orogenic Belt

The sources of early Mesozoic magmatism in the North and the South Qinling Belt are different according to the captured/inherited zircons, whole-rock Sr-Nd and zircon Hf isotopes (Figs. 9–13). Based on our compilation, the spectrum of ages for inherited/captured zircons in the granitoids from the North Qinling Belt are mainly early Paleozoic, Neoproterozoic, and Paleoproterozoic (Fig. 12). The early Paleozoic magmatic rocks are mainly arc-related I- and S-type granitoids, and Neoproterozoic and Paleoproterozoic rocks are the main basement (Patiño Douce, 1999; Wang et al., 2009; Zhang et al., 2013). In contrast, the inherited/captured zircons in the granitoids from the South Qinling Belt are dominated by early Paleozoic and Neoproterozoic zircons (Fig. 12). Considering that the South Qinling Belt was a forearc/foreland basin during the Paleozoic (Yan et al., 2006a, 2006b, 2007), the early Paleozoic zircons could come from the sedimentary rocks, and the

Neoproterozoic zircons come from the basement (Dong et al., 2017; Hu et al., 2016b; Ling et al., 2008).

From an isotopic perspective, the relatively uniform values of whole-rock Sr-Nd isotopes ( $(^{87}\text{Sr}/^{86}\text{Sr})_i = 0.7046$  to  $0.7080$ ;  $\epsilon\text{Nd(t)} = -7.3$  to  $-0.3$ ) from the MME contrast with the wide range of zircon Hf data ( $\epsilon\text{Hf(t)} = -17.7$  to  $+13.2$ ), reflecting homogenization of the whole-rock isotopes (Figs. 9 and 10). Overall, multiple sources are involved in the formation of the MME, including enriched lithospheric mantle, depleted asthenospheric mantle, and enriched crustal sources (Figs. 9 and 10). The coeval mafic dikes and xenoliths showing isotopically evolved features indicate that the enriched lithospheric mantle is the primary source of mafic magma (Hu et al., 2018; Qin et al., 2010a; Wang et al., 2007). The andesites with enriched isotopic features ( $(^{87}\text{Sr}/^{86}\text{Sr})_i = 0.7079$  to  $0.7123$ ;  $\epsilon\text{Nd(t)} = -9.3$  to  $-7.7$ ) were proposed to be a result of mixing of subducted sediments and lithospheric mantle (Fig. 9B; Li et al., 2013). The diorite have large variations of isotopic features, indicating the involvement of crustal materials ( $(^{87}\text{Sr}/^{86}\text{Sr})_i = 0.7055$  to  $0.7075$ ;  $\epsilon\text{Nd(t)} = -4.5$  to  $-1.1$ ;  $\epsilon\text{Hf(t)} = -15.3$  to  $+5.4$ ). Therefore,

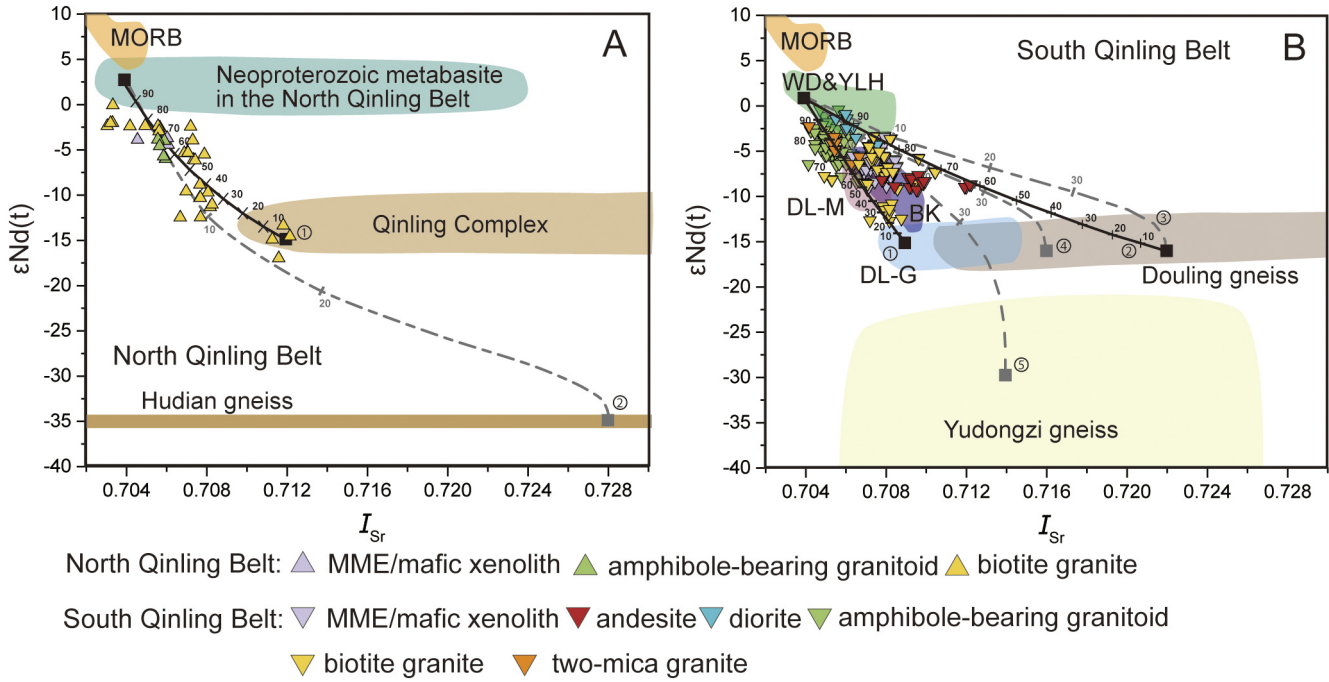


**Fig. 9.** Plots of whole-rock  $\epsilon_{\text{Nd}}(t)$  versus initial Sr isotopic ratios ( $I_{\text{Sr}}$ ) of the granitoids and MME in the North Qinling Belt (A) and South Qinling Belt (B). This figure illustrates the trends of simple mixing and crustal assimilation-fractional crystallization (AFC), and the modeling parameters are shown in Table 3. The data of basements and end-members are from: MORB (mid-ocean ridge basalt; Tribuzio et al., 2004); North Qinling Belt Neoproterozoic metabasite (H. Wang et al., 2013); Qinling Complex (S.-B. Zhang et al., 2006); Hudian granitoid gneiss (Yang, 2017); Wudang and Yaolinghe (WD&YLH; Xia et al., 2008; Zhu et al., 2014); Bikou (BK; Xia et al., 2007); Douling mafic rocks (DL-M; Yang et al., 2011); Douling granitoids (DL-G; Yang et al., 2011); Douling gneiss (Shen et al., 1997); Yudongzi gneiss (Zhang et al., 2001). The data of the early Mesozoic granitoids and MME are cited from the Table 1 and Supplementary Information 1.

we suggest that most mafic and intermediate rocks were derived from an enriched lithospheric mantle and experienced interaction with the crustal materials (Figs. 9 and 10).

The granitoid rocks were mainly derived from the basement in the different belts. The early Mesozoic granitoids in the North Qinling Belt show a relatively large range of initial isotope ratios suggesting magma mixing and/or source mixing (Figs. 9 and 10; Table 3).

According to our calculation, the juvenile Neoproterozoic metabasaltic rocks and old Qinling Complex were the most prominent crustal sources for granitoids in the North Qinling Belt (Fig. 9A; Table 3). Contour mapping of Sr-Nd-Hf isotopes suggest that more juvenile materials were involved in the generation of granitoids in the eastern relative to the western North Qinling Belt (Fig. 13).

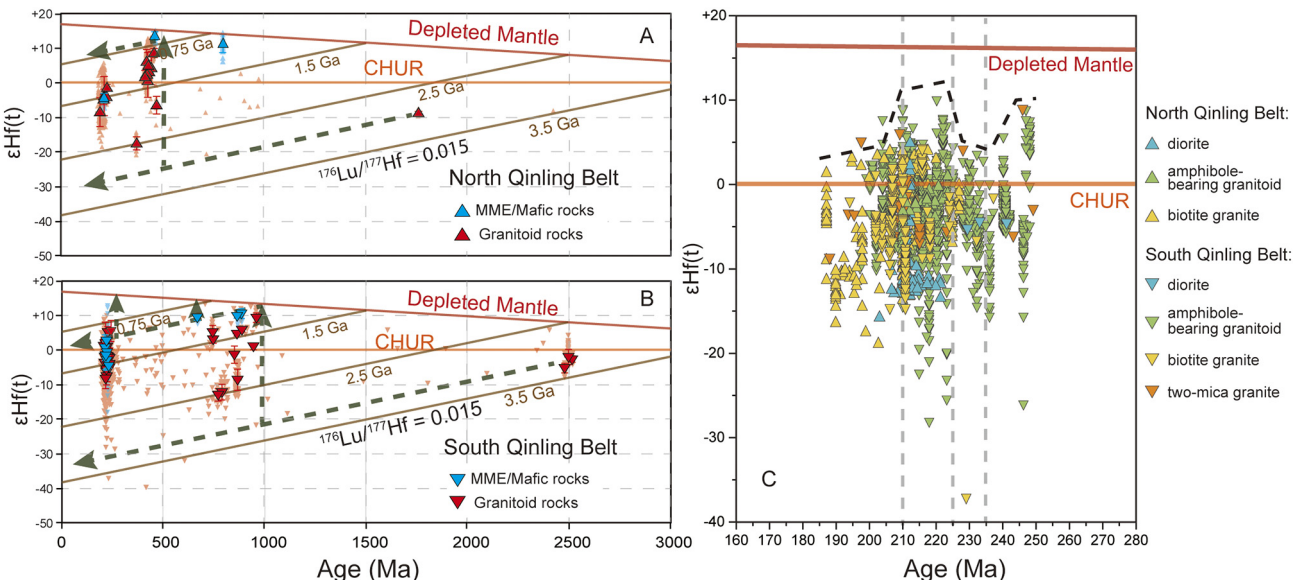


**Fig. 10.** Plots of the zircon  $\epsilon_{\text{Hf}}(t)$  versus age of the granitoids and MME/mafic rocks in the North Qinling Belt (A) and South Qinling Belt (B), and the granitoids formed during early Mesozoic in the Qinling Orogenic Belt (C). The data of Archean to Paleozoic rocks are from: Proterozoic rocks in the North Qinling Belt (Yang, 2017; X. Wang et al., 2013); Paleozoic rocks in the North Qinling Belt (Guo, 2010; Lei, 2010; Lü et al., 2014; Qin et al., 2014, 2015; Qin, 2016; H. Wang et al., 2016; Yang, 2017); Archean rocks in the South Qinling Belt (Hu et al., 2013; Y. Wu et al., 2014); Neoproterozoic rocks in the South Qinling Belt (Hu et al., 2016b; Liu, 2011; Liu et al., 2014; M. Yan et al., 2014; Zhang et al., 2016, 2018). The data of the early Mesozoic granitoids and MME/mafic rocks are cited from the Table 1 and Supplementary Information 3.

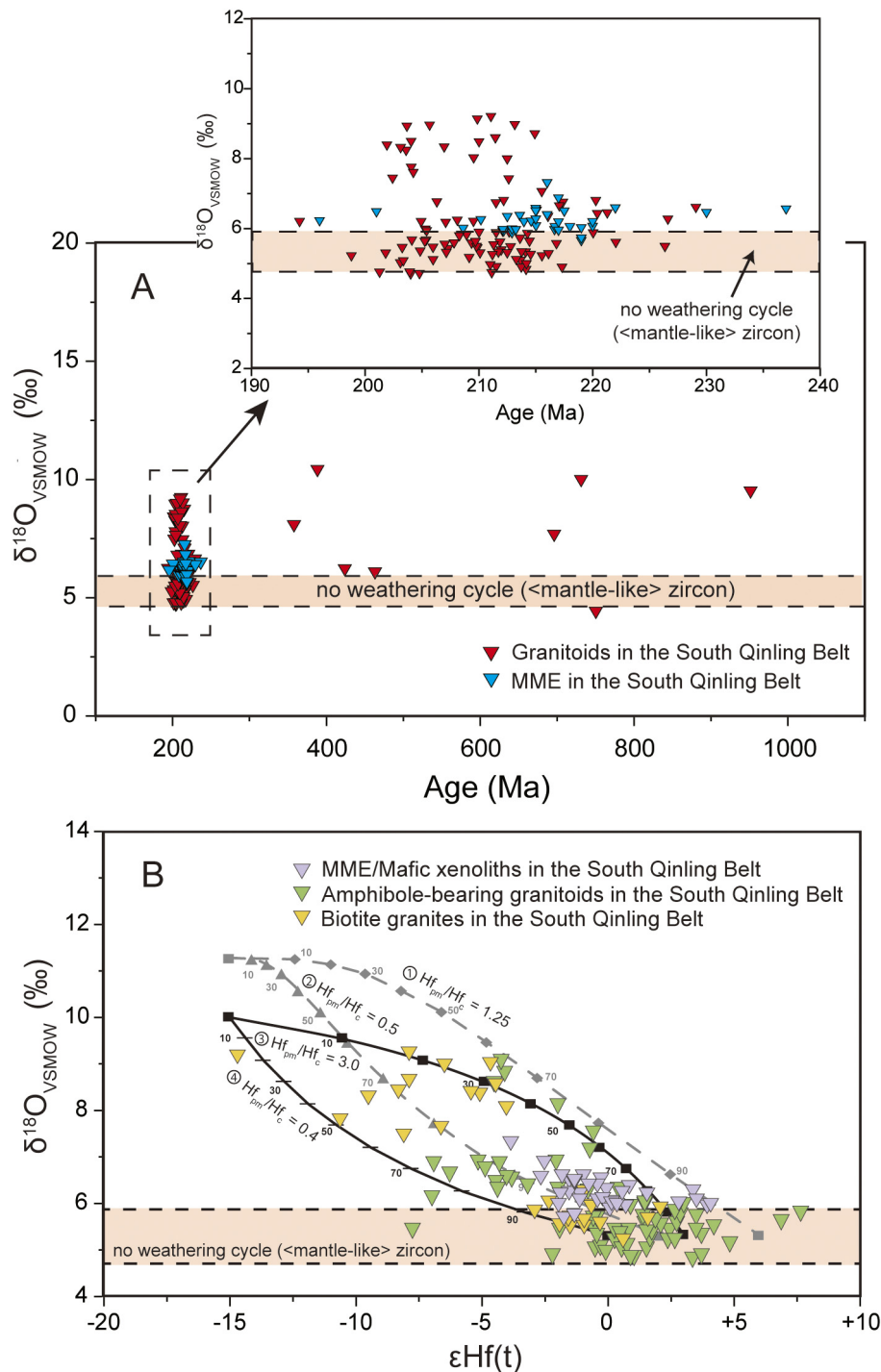


**Fig. 11.** Plot of the zircon  $\delta^{18}\text{O}$  versus age (A) and  $\delta^{18}\text{O}$  versus  $\epsilon\text{Hf}(t)$  (B) of the granitoid rocks and MME/mafic rocks in the South Qinling Belt. This figure illustrates the trends of crustal assimilation-fractional crystallization (AFC) (curves 1 and 2) and simple mixing (curves 3 and 4). The ratio of the Hf concentrations in the parental magma (pm) and crustal (c) end members ( $\text{Hf}_{\text{pm}}/\text{Hf}_c$ ) are indicated for each. The  $\delta^{18}\text{O}$  for the mantle-like zircon is from Valley et al. (1998). The modeling parameters are shown in Table 4.

The magma sources of granitoids in the South Qinling Belt are more complex. Three different sources may have contributed to the genesis of the granitoid magmas, including Neoarchean basement rocks, Neoproterozoic metaigneous rocks, and Neoproterozoic metasedimentary rocks (Figs. 8–10). A three end-member mixing model for whole-rock Sr-Nd isotopes indicates that a mixed source of Neoproterozoic mafic rocks, Douling Neoproterozoic granitoids and Douling Neoarchean gneisses is plausible (Fig. 9B; Table 3). Additionally, the zircon Hf-O isotopic features indicate that they were formed by partial melting of the Neoproterozoic metaigneous rocks and metasedimentary rocks (Fig. 11; Table 4).

Therefore, Neoproterozoic basement rocks are interpreted to be the major crustal source of granitoids in the South Qinling Belt. The temporal variations of granitoid Hf isotopic ratios show more juvenile signatures during the two magmatic peaks, which indicates that melts from the depleted mantle or juvenile crust were involved (Fig. 10C). Contour mapping of Sr-Nd-Hf isotopes shows that enriched materials exist in all three segments (western, middle, and eastern) in the South Qinling Belt (Fig. 13), which argues against different basements in the South Qinling Belt. The variations in isotopic features in the North and South Qinling Belts reflect different contributions of diverse magmatic sources (Figs. 9–11, and 13).

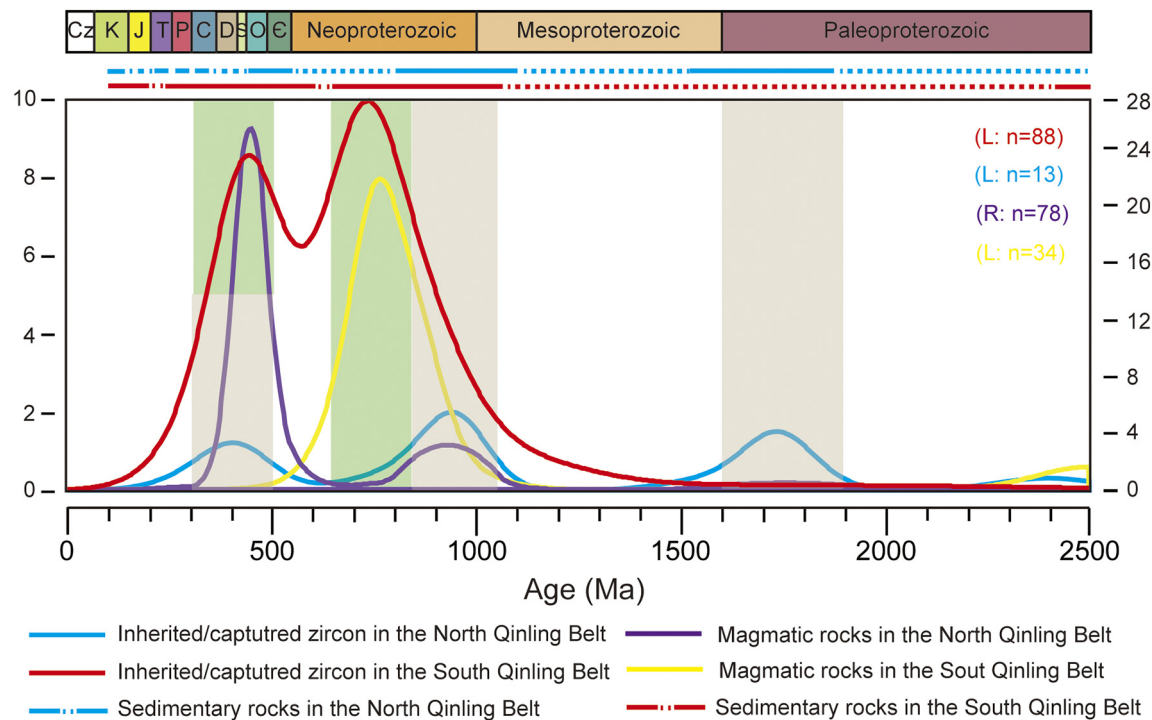


**Fig. 12.** Probability density plots of the inherited/captured zircons in the North Qinling Belt and South Qinling Belt and their comparison to the magmatic rocks (prior to Mesozoic) and sedimentary rocks in the North Qinling Belt and South Qinling Belt. L refers to the left ordinate and R refers to the right ordinates. Abbreviations: e-Cambrian; O-Ordovician; S-Silurian; D-Devonian; C-Carboniferous; P-Permian; T-Triassic; J-Jurassic; K-Cretaceous; Cz-Cenozoic. The data are cited from the Supplementary Information 4.

#### 4.2. Petrogenesis of early Mesozoic magmatic rocks in the Qinling Orogenic Belt

##### 4.2.1. MME/Xenoliths/andesite-dioritic rocks

Based on field observations (phenocryst transfer from host granitoids to MME), microscopic features (acicular apatite in the MME), whole-rock geochemical features and the absence of old inherited zircons, we suggest that the MME originated from the mantle-derived melts and were injected into a large volume of felsic magma (Browne et al., 2006). These features indicate that they are mingling products of both mantle- and crust-sourced melts. The MME have relatively consistent geochemical features and are similar to the mafic xenoliths (Hu et al., 2016a, 2017b, 2018; Jiang et al., 2010, 2012; Qin et al., 2010a, 2010b, 2013; X. Wang et al., 2011). The geochemical and isotopic characteristics indicate that they were derived from an enriched mantle source. Based on experimental data, the high-K calc-alkaline to shoshonitic compositions are comparable to those of melts derived from a phlogopite-bearing lithospheric mantle (Figs. 6 and 14; Condamine and Médard, 2014; Condamine et al., 2016). Their relatively high Rb/Sr (generally  $>0.1$ ) and low Ba/Rb (generally  $<20$ ) ratios also suggest that the melts were in equilibrium with phlogopite (Fig. 14; Furman and Graham, 1999). Therefore, the MME/mafic xenoliths are proposed to be derived mainly from the partial melting of phlogopite-bearing metasomatized lithospheric mantle and then injected into a felsic magma with mush (Hu et al., 2016a, 2017b; Wang et al., 2007). This process enabled them to be captured, and captured some early crystallized granitoid phenocrysts with textural features of fast crystallization.

The geochemical features of andesites/dioritic rocks show clear changes with time (Figs. 11–14). All these rocks have high MgO contents and Mg# values, which are indicative of a large portion of mantle-derived melts (Fig. 6; Martin et al., 2005; Rapp and Watson, 1995; Stern and Kilian, 1996). The ~250–235 Ma andesites were proposed to be derived from the partial melting of a mantle wedge that was metasomatized by subducted sediments, whereas the coeval diorites

were likely derived from the partial melting of a metasomatized mantle wedge modified by subduction fluid (Figs. 6 and 14; Li et al., 2013; X. Li et al., 2015). Most diorites formed during ~225–210 Ma show a geochemical affinity to the coeval MME, indicating that they have a similar petrogenesis (Fig. 14B and E). Some ~225–210 Ma diorites show enrichment in Ba, K<sub>2</sub>O and LREE and an amphibole-bearing trend in the Rb/Sr vs. Ba/Sr diagram (Fig. 14). These diorites resemble high Ba-Sr appennines in the Caledonian Orogen, which was formed by carbonate-dominated metasomatism and low-degree partial melting of the mantle (Fowler et al., 2008). The emplacement of a ~235 Ma carbonatite in the Qinling orogen may support this inference (Xu et al., 2014). The differences between the andesites and dioritic rocks were chiefly caused by diverse enrichment materials and various melting degrees. Collectively, the mafic rocks and associated andesitic/dioritic rocks are primarily formed by the partial melting of metasomatized lithospheric mantle, and their geochemical diversity reflects the heterogeneity of lithospheric mantle and infracrustal AFC processes.

##### 4.2.2. Granitoid rocks

The early Mesozoic amphibole-bearing granitoids are one of the most important lithologies in the Qinling Orogenic Belt. The majority have elevated MgO and Mg# values compared to experimental melts suggesting that mantle-sourced melts were involved (Fig. 6I-P; Martin et al., 2005; Qian and Hermann, 2013; Rapp and Watson, 1995; Stern and Kilian, 1996). Major and trace-element mixing modeling suggests that the mixture ratios of mafic/felsic melts was approximately 1:9 to 4:6 (Figs. 6M-P and 8G-J; Table 2). Therefore, the mantle-derived magma not only provided heat for the melting of continental crust but also mixed with crust-derived melts in different proportions. The relatively low Th/La (<0.5) of most amphibole-bearing granitoids argues against the idea that abundant supracrustal sediments were involved (Fig. 15A-D; Hu et al., 2018; Q. Wang et al., 2016). In source discrimination diagrams, the amphibole-bearing granitoids mainly plot in the area of partial melting of basaltic to tonalitic rocks (Fig. 15E-L; Altherr et al., 2000; Moyen, 2009; Otamendi and Patiño Douce, 2001; Patiño Douce,

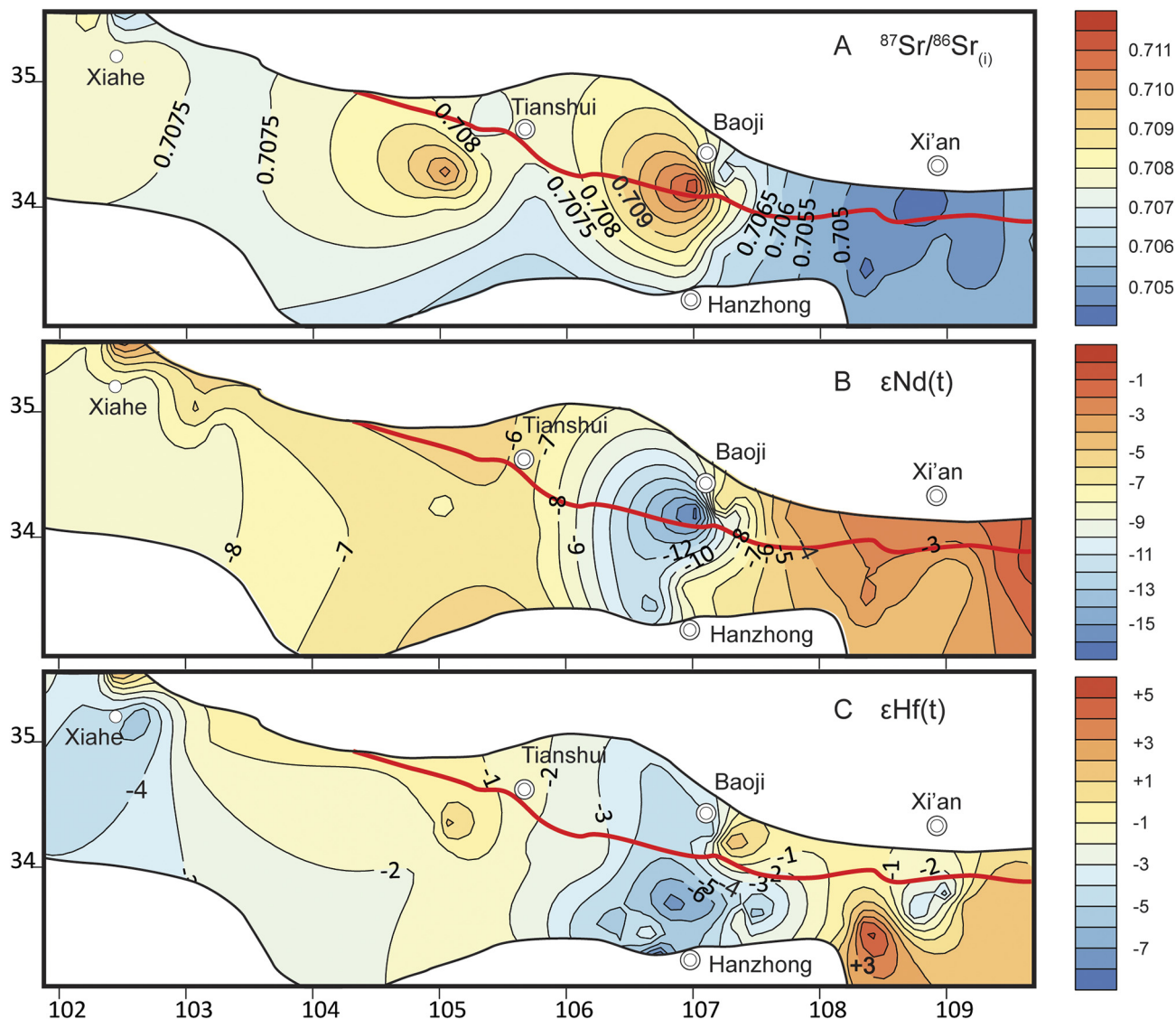


**Fig. 13.** Contour map of the initial Sr isotopic ratios (A),  $\epsilon_{\text{Nd}}(\text{t})$  values (B), and  $\epsilon_{\text{Hf}}(\text{t})$  values (C) of the granitoids in the Qinling Orogenic Belt. The contour maps were drawn by the Surfer software, and the Kriging interpolation method was used. The isotopic data of the early Mesozoic granitoids are cited from the Supplementary Information 1 and 3.

1999; Q. Wang et al., 2016). Our trace-element modeling demonstrates that the partial melting of Neoproterozoic mafic rocks at various crustal depths and subsequent mixing with mafic magma in different proportions could have produced these granitoid assemblages (Fig. 8; Hu et al., 2017b). The elevated zircon O isotopes and Th/La ratios of some samples suggest the assimilation of metasedimentary rocks during the magma emplacement (Figs. 11 and 15A-D). The samples dominantly plot in the F1 and F2 field in the Sr/Y vs. La/Yb diagram, suggesting that they are in equilibrium with garnet and amphibole in the middle to lower crust (Fig. 15M-P; Q. Wang et al., 2016). These granitoids have generally low melting temperatures ( $< 770^{\circ}\text{C}$ ) indicating a relatively high-water content in the source region (Collins and Richards, 2008). Except for the Hejiazhuang granitoids, which may be derived from subducted oceanic slab (Yang et al., 2014), all amphibole-bearing granitoids from Stage I show low Sr/Y and La/Yb ratios (Fig. 15M). The increasing Sr/Y and La/Yb ratios of granitoids from Stage I to Stage III suggest increased crustal thicknesses (Fig. 15M-P). These granitoids mainly follow Trend I in source discrimination diagrams and show increased Sr/Y and decreased Dy/Yb ratios with increasing SiO<sub>2</sub>, illustrating the fractionation of amphibole (Fig. 15E-L; Davidson et al., 2007; Hu et al., 2018). In summary, the amphibole-bearing granitoids were

primarily formed by the partial melting of Neoproterozoic metagneous rocks in the middle to lower crust, mixed with melts generated from enriched mantle, and experienced assimilation and fractional crystallization during their ascent.

The high SiO<sub>2</sub> biotite granites and two-mica granites, which were dominantly formed in Stage III and IV, show low MgO contents and Mg# values, suggesting that they were chiefly generated by partial melting of a pure crustal source (Fig. 5; Martin et al., 2005; Patiño Douce, 1999; Qian and Hermann, 2013; Rapp and Watson, 1995; Stern and Kilian, 1996). Therefore, the coeval mantle-derived melts only provided the heat for crustal melting and did not mix with these crust-derived melts. Some samples show a mantle-like zircon O isotopic feature, indicating that metagneous rocks are in their source (Figs. 11). However, most samples have high zircon O isotopes and plot in the fields of melts derived from metagreywackes and pelites, suggesting that metasedimentary rocks are their primary sources (Figs. 11 and 15; Altherr et al., 2000; Moyen, 2009; Otamendi and Patiño Douce, 2001; Patiño Douce, 1999; Q. Wang et al., 2016). Such features reflect the heterogeneity of the magmatic sources. The biotite granites and two-mica granites mainly display fractionated REE patterns with clearly negative Eu anomalies and depletion of Ba and Sr, indicating strong

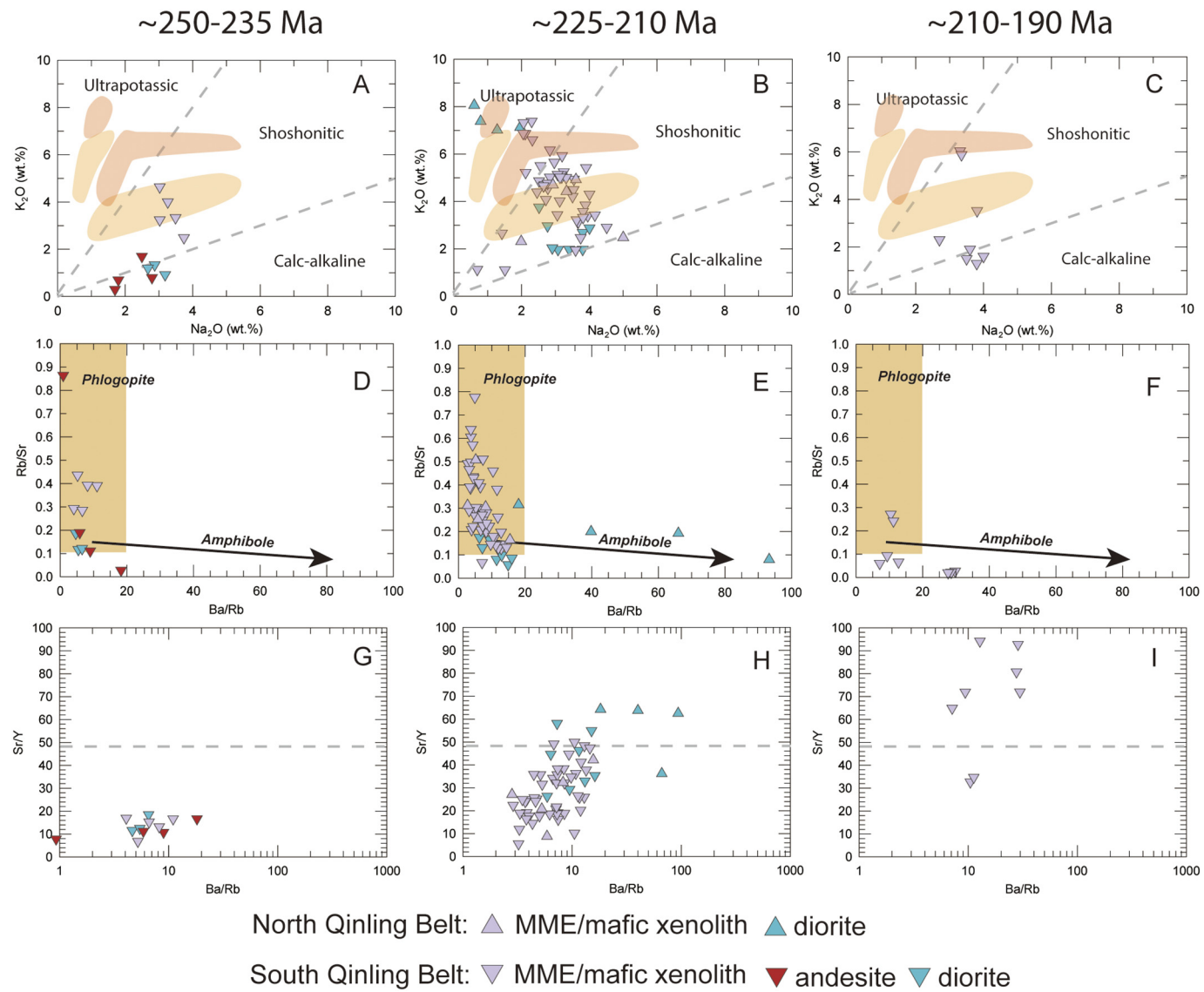


**Fig. 14.** Geochemical features of MME/mafic xenolith and andesite/diorite with Mg# values higher than 60 that formed during different stages in the Qinling Orogenic Belt. (A–C)  $K_2O$  versus  $Na_2O$  diagram (after Peccerillo and Taylor, 1976); (D–F)  $Rb/Sr$  versus  $Ba/Rb$  diagram (after Yang et al., 2004); (G–I)  $Sr/Y$  versus  $Ba/Rb$  diagram.

fractionation of feldspar (Figs. 7 and 8; Hu et al., 2018). The fractionation of feldspar would gradually increase the Th/La ratio and decrease the Sr/Y ratios, but a very high Th/La ( $>1.0$ ) most likely reflects the involvement of sediments (Fig. 15A–D; Hu et al., 2018; Q. Wang et al., 2016). It is interesting that these biotite granites and two-mica granites, unlike the amphibole-bearing granitoids, mainly plot in the F2 field in the Sr/Y vs. La/Yb diagram and systematically have higher La/Yb relative to Sr/Y (Fig. 15). This phenomenon is a result of the partial melting of sedimentary rocks in the middle or upper crust (Moyen, 2009; Otamendi and Patiño Douce, 2001). Compared to the amphibole-bearing granitoids, these pure crustal-derived granites show relatively higher Zr-saturation temperatures, indicating their relatively low water contents in the magmatic source (Supplementary Information 1; Collins and Richards, 2008; Weinberg and Hasalová, 2015). Therefore, these biotite granites and two-mica granites were formed by the partial melting of mainly metasedimentary rocks with minor metaigneous rocks and experienced the fractionation of feldspar.

#### 4.3. Crust-mantle interaction during the early Mesozoic in the Qinling Orogenic Belt

Stage I magmatism is characterized by calc-alkaline intermediate to felsic compositions, especially andesites and diorites, in the western South Qinling Belt (Figs. 3 and 16A). The generally low temperatures of granitoids ( $< 740^\circ\text{C}$ ) indicate that crustal melting during this stage was under water-present conditions (Fig. 16B; Miller et al., 2003; Weinberg and Hasalová, 2015). In consideration of their petrogenesis, crust-mantle interaction in a lower crustal MASH (melting, assimilation, storage, and homogenization) zone was an important mechanism during this stage (Stern, 2002; Bachmann and Huber, 2016).

Magmatism during Stage II is rare and is recognized as a magmatic gap. Few magmatic intrusions with intermediate and calc-alkaline features were exposed in the middle South Qinling Belt and North Qinling Belt (Figs. 3 and 5). The results of mixing modeling suggest that the weak magmatism is a feature of neglected crust-mantle mixing in Stage II, indicating weak crust-mantle interaction (Figs. 5 and 6).

**Table 2**

Trace elements modeling for the granitoid rocks in the Qinling Orogenic Belt.

Elements	Co 08LY2-14	MME		Kd		Kd		Kd		Kd		Model 1 (PM + Mix)		Model 1' (PM + Mix)	
		HYS-1-2	PI	Hb	Cpx	Grt	Opx	Rt	(30/40/16/3/10.7/0.3)	F = 0.1	F = 0.4	(15/43/16/15/10.7/0.3)	F = 0.1	F = 0.4	
Rb	30	117	0.1	0.18	0.032	0.009	0.003	0.001	0.11	138.20	85.54	0.11	142	86	
Ba	345	1221	0.21	0.28	0.1	0.017	0.003	0.015	0.19	1247.51	890.24	0.19	1304	900	
Th	0.55	2.6	0.032	0.017	0.04	0	0.11	0.54	0.04	3.53	1.82	0.04	3.60	1.83	
K	10,460	21,551	0.4	0.33	0.037	0.02	0.002	0	0.26	27,475	19,923	0.26	30,267	20,538	
Nb	10.1	13.3	0.06	1.1	0.8	0	0.8	52.6	0.83	12.48	12.07	0.83	12.30	11.96	
Ta	0.7	0.86	0.035	0.43	0.5	0.22	0.2	99.5	0.59	1.01	0.90	0.59	0.98	0.89	
La	15.9	25.5	0.45	0.36	0.49	0.39	0.4	0.237	0.41	30.44	24.93	0.41	31	25	
Ce	35	61	0.267	0.63	0.84	0.69	0.31	0.296	0.52	61.30	53.86	0.52	58	52	
Sr	443	257	1.7	0.36	0.17	0.01	0.009	0.048	0.68	475	431	0.68	639	503	
Nd	21	29	0.203	2.2	0.86	0.603	0.47	0.4	1.15	23	23	1.15	22	23	
Sm	4.54	5.7	0.165	2.38	1.6	2.035	0.46	2.4	1.37	4.32	4.50	1.37	3.98	4.23	
Eu	1.42	1.81	3.1	1.39	1.5	0.515	0.34	0.25	1.78	1.22	1.30	1.78	1.34	1.41	
Gd	4.26	5.58	0.125	2.3	1.35	6.975	0.17	0.01	1.40	4.11	4.29	1.40	3.42	3.67	
Dy	4.41	4.76	0.112	2.68	1.6	28.6	0.26	0.0008	2.25	3.15	3.42	2.25	2.41	2.59	
Er	2.29	2.84	0.084	2.47	1.33	42.8	0.43	0.675	2.56	1.71	1.85	2.56	1.33	1.41	
Y	21	24.7	0.1	1.31	5.5	22	0.91	0.4	2.19	16.0	17.2	2.19	12.7	13.7	
Yb	2.18	2.52	0.09	2.1	1.3	43	0.77	0.0158	2.45	1.58	1.71	2.45	1.20	1.27	
Lu	0.34	0.34	0.092	1.7	1.4	39	0.71	0.016	2.18	0.24	0.26	2.18	0.17	0.18	
Elements	Co 08LY2-9	MME		Kd		Kd		Kd		Model 2 (PM + Mix)		Model 2' (PM + Mix)			
		HYS-1-2	PI	Hb	Cpx	Grt	Opx	Rt	(30/40/20/4.5/5.2/0.3)	F = 0.1	F = 0.4	(15/40/20/19.5/5.2/0.3)	F = 0.1	F = 0.4	
Rb	47	117	0.1	0.18	0.032	0.009	0.003	0.001	0.11	213	104	0.10	226	106	
Ba	588	1221	0.21	0.28	0.1	0.017	0.003	0.015	0.20	1946	1153	0.17	2123	1185	
Th	2.52	2.60	0.032	0.017	0.04	0	0.11	0.54	0.03	16.20	5.33	0.03	16.7	5.36	
K	14,394	21,551	0.4	0.33	0.037	0.02	0.002	0	0.26	38,749	25,012	0.20	44,990	26,368	
Nb	13.3	13.3	0.06	1.1	0.8	0	0.8	52.6	0.82	15.39	14.61	0.81	15.5	14.7	
Ta	0.92	0.86	0.035	0.43	0.5	0.22	0.2	99.5	0.60	1.32	1.14	0.63	1.28	1.12	
La	23	25.5	0.45	0.36	0.49	0.39	0.4	0.237	0.42	44	33	0.41	45	34	
Ce	51	61	0.267	0.63	0.84	0.69	0.31	0.296	0.55	81	68	0.61	75	65	

(continued on next page)

**Table 2** (continued)

Elements	Co 08LY2-9	Model 2 (PM + Mix)								Model 2' (PM + Mix)				
		MME HYS 1-2	Kd Pl	Kd Hb	Kd Cpx	Kd Grt	Kd Opx	Kd Rt	D(Pl/Hb/Cpx/Grt/Opx/Rt) (30/40/20/4.5/5.2/0.3)	Mix (8/2) F = 0.1	Mix (8/2) F = 0.4	D(Pl/Hb/Cpx/Grt/Opx/Rt) (15/40/20/19.5/5.2/0.3)	Mix (6/4) F = 0.1	Mix (6/4) F = 0.4
Sr	372	257	1.7	0.36	0.17	0.01	0.009	0.048	0.69	465	417	0.44	656	501
Nd	32	29	0.203	2.2	0.86	0.603	0.47	0.4	1.17	28	29	1.23	27	28
Sm	7.04	5.7	0.165	2.38	1.6	2.035	0.46	2.4	1.44	5.16	5.59	1.72	4.55	5.07
Eu	2.52	1.81	3.1	1.39	1.5	0.515	0.34	0.25	1.83	1.52	1.71	1.44	1.81	1.96
Gd	6.88	5.58	0.125	2.3	1.35	6.975	0.17	0.01	1.55	4.80	5.25	2.58	3.39	3.94
Dy	6.93	4.76	0.112	2.68	1.6	28.6	0.26	0.0008	2.73	3.12	3.68	7.00	1.82	2.16
Er	4.28	2.84	0.084	2.47	1.33	42.8	0.43	0.675	3.23	1.71	2.03	9.64	0.96	1.12
Y	35	24.7	0.1	1.31	5.5	22	0.91	0.4	2.69	16.0	18.8	5.98	10.0	12.0
Yb	3.77	2.52	0.09	2.1	1.3	43	0.77	0.0158	3.10	1.55	1.84	9.54	0.85	1.00
Lu	0.56	0.34	0.092	1.7	1.4	39	0.71	0.016	2.78	0.24	0.28	8.62	0.13	0.15
Model 3														
Elements	Co	Kd	Kd	D(Pl/Kf)	FC			Co 14HY04-3	Kd	Kd	D(Pl/Kf)	FC		
	16HY06-3	Pl	Kf	(70/30)	F = 0.8	F = 0.5	F = 0.3		Pl	Kf	(70/30)	F = 0.8	F = 0.5	F = 0.3
Rb	128	0.05	1.75	0.56	141	174	218	158	0.05	1.75	0.56	174	215	269
Ba	1148	0.36	4.30	1.54	1017	788	598	545	0.36	4.30	1.54	483	374	284
Th	11.5	0.05	0.02	0.04	14.2	22	37	14.4	0.05	0.02	0.04	17.8	28	46
K	22,497	0	1	0	25,209	32,037	41,571	30,882	0	1	0	34,604	43,977	57,065
Nb	11.0	0.88	0.16	0.66	11.9	13.9	16.5	14.9	0.88	0.16	0.66	16.1	18.8	22
Ta	0.80	0.13	0.02	0.10	0.98	1.50	2.37	0.62	0.13	0.02	0.10	0.76	1.16	1.84
La	31	0.46	0.15	0.37	35	48	66	27	0.46	0.15	0.37	31	41	57
Ce	61	0.40	0.06	0.30	71	99	141	52	0.40	0.06	0.30	60	84	120
Sr	655	2.80	2.60	2.74	444	196	81	171	2.80	2.60	2.74	116	51	21
Nd	22.5	0.29	0.05	0.22	27	39	58	20.0	0.29	0.05	0.22	24	34	51
Sm	3.63	0.23	0.20	0.22	4.32	6.23	9.27	3.75	0.23	0.20	0.22	4.46	6.43	9.58
Eu	1.11	1.30	2.10	1.54	0.98	0.76	0.58	0.67	1.30	2.10	1.54	0.59	0.46	0.35
Gd	3.28	0.15	0.20	0.17	3.95	5.85	8.96	3.44	0.15	0.20	0.17	4.14	6.14	9.40
Dy	1.87	0.11	0.06	0.10	2.29	3.50	5.55	2.89	0.11	0.06	0.10	3.53	5.40	8.57
Er	0.86	0.08	0.01	0.06	1.06	1.65	2.66	1.65	0.08	0.01	0.06	2.04	3.17	5.12
Y	9.20	0.10	0.08	0.09	11.3	17.2	27	15.2	0.10	0.08	0.09	18.6	28	45
Yb	0.73	0.02	0.03	0.02	0.91	1.44	2.37	1.69	0.02	0.03	0.02	2.10	3.33	5.48
Lu	0.11	0.01	0.01	0.01	0.14	0.22	0.36	0.23	0.01	0.01	0.01	0.29	0.46	0.77

Note: The Model 1, Model 1', Model 2, and Model 2' are based on the batch melting model ( $Cl = Co/[D + F*(1-D)]$ ) and simple mixing model (the number in the bracket means the ratio of granitoid melt to MME). The Model 3 and Model 3' are based on the Rayleigh fractional crystallization model ( $Cl = Co^*F^{(D-1)}$ ).

Partition coefficients (Kd) of minerals are from <http://earthref.org/GERM/>.

Abbreviation: D denotes the bulk distribution coefficients; Co, the weight concentration of elements in the source rock (ppm); Cl, the weight concentration of elements in the melt (ppm); F, the fraction of melt produced (partial melting) or the fraction of remaining melt (fractional crystallization). Pl, Plagioclase; Hb, Hornblende; Cpx, Clinopyroxene; Grt, Garnet; Opx, Orthopyroxene; Rt, Rutile.

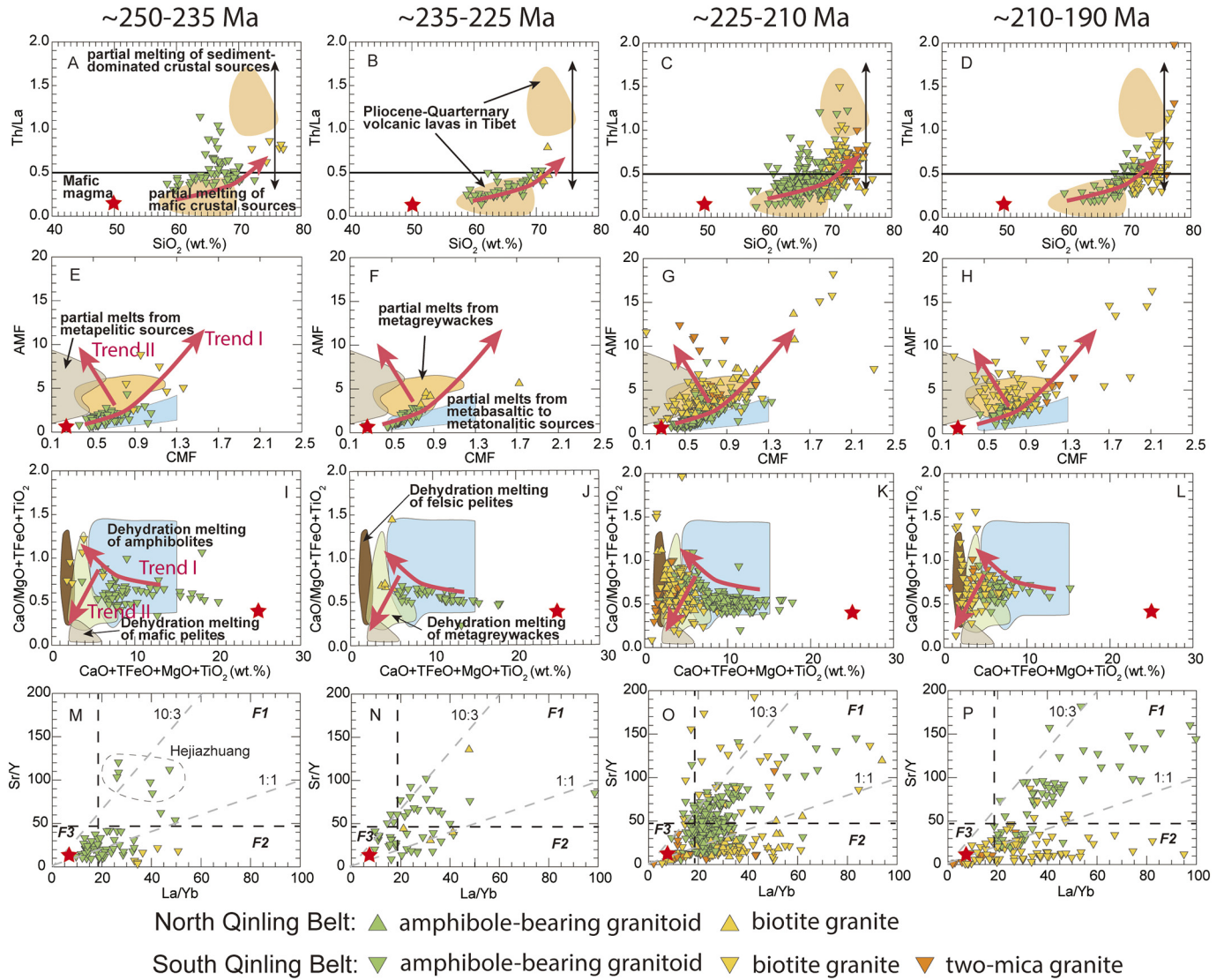


**Fig. 15.** Geochemical features of granitoid rocks formed during different stages in the Qinling Orogenic Belt. (A–D) Th/La versus SiO<sub>2</sub> diagram (after Q. Wang et al., 2016); (E–H) AMF (molar Al<sub>2</sub>O<sub>3</sub>/(MgO + FeOT)) versus CMF (molar CaO/(MgO + FeOT)) diagram (after Altherr et al., 2000); (I–L) CaO/(FeOT + MgO + TiO<sub>2</sub>) versus CaO + FeOT + MgO + TiO<sub>2</sub> (wt.%) diagram (after Patiño Douce, 1999); (M–P) Sr/Y versus La/Yb diagram. The red star represents the composition of mantle-derived melts (MME). The Trend I represents the process of amphibole-dominated fractionation, and Trend II represents the process of plagioclase-dominated fractionation.

The Stage III magmatism is characterized by extensive granitoid intrusions with abundant coeval mafic rocks. The MME are widely distributed in the Stage III granitoid intrusions, illustrating intensive mantle-derived magmatism during this stage (Deng et al., 2016; Hu et al., 2016a, 2017b, 2018; Qin et al., 2010a, 2013; X. Wang et al., 2011). The mantle-derived magmatism during this stage shows a younging trend from the east to the west, which is possibly caused by the gradual migration of heat flow in the mantle depth (Fig. 16C; Hu et al., 2016a). The significant crust-mantle magma mixing results in a broad range of SiO<sub>2</sub> contents and zircon Hf isotopic ratios (Figs. 8, 10 and 16A). Compared to Stage II, the average temperatures of these granitoids are slightly higher, although the temperature range is similar, considering the uncertainties, which may be related to the high water contents of these magmas, as evidenced by abundant amphibole-bearing granitoids (Fig. 16B). In the deep crust, mantle-derived melts provide enough heat for the extensive melting of crustal rocks and mix with them. At middle to shallow crustal levels, the mafic magma is mingled with crustal-derived magmas.

Stage IV magmatism is characterized by dominantly high-SiO<sub>2</sub> metasedimentary rocks-derived granites, which are sporadically distributed in the Qinling Orogenic Belt but coeval mafic magmatic rocks are extremely limited (Figs. 3, 6–11 and 16A). In this regard, the crust-mantle magma interaction is insignificant, and the mantle heat flow was not high enough during this stage due to lacking hydrous mantle-derived magma, as evidenced by minor amphibole-bearing granitoids only forming in the early times of this stage (Fig. 6). In general, the metasedimentary rocks have a lower melting point compared to the metaigneous rocks (Weinberg and Hasalová, 2015). Therefore, without extensive mantle-derived melts providing heat to the crust, the increasing temperatures of granitoids (720–800 °C) were most likely caused by a low water content in the source (Fig. 16B).

**Table 3**  
Parameters used for whole-rock Sr-Nd isotopic modeling.

Simple mixing model				
	Sr (ppm)	Initial Sr	Nd (ppm)	$\epsilon_{\text{Nd}}(t)$
NQB Neoproterozoic metabasite (curve 1 and 2 in A)	220	0.704	16	2.5
NQB Qinling Complex (curve 1 in A)	150	0.712	20	-15
SQB Wudang & Yaolinghe Group (curve 1-5 in B)	250	0.704	15	1
SQB Douling granitoid (curve 1 in B)	350	0.709	25	-15
SQB Douling gneiss (1) (curve 2 in B)	350	0.722	30	-16
Assimilation and fractional crystallization (AFC) model				
D(Sr) = 3.0	D(Nd) = 1.3	r = 0.6		
	Sr (ppm)	Initial Sr	Nd (ppm)	$\epsilon_{\text{Nd}}(t)$
NQB Neoproterozoic metabasite (curve 1 and 2 in A)	220	0.704	16	2.5
NQB Hudian gneiss (curve 2 in A)	200	0.728	60	-35
SQB Wudang & Yaolinghe Group (curve 1-5 in B)	250	0.704	15	1
SQB Douling gneiss (1) (curve 3 in B)	350	0.722	30	-16
SQB Douling gneiss (2) (curve 4 in B)	350	0.716	30	-16
SQB Yudongzi gneiss (curve 5 in B)	400	0.714	15	-30

Note: D denotes the partition coefficient of Hf element; r is assimilation rate.

The partition coefficients are from <https://earthref.org/GERM/KDD/>.

The simple mixing model and AFC model are based on DePaolo (1981).

#### 4.4. Crustal thickness, structural features, metamorphism, and sedimentary records during the Mesozoic and their implications for tectonic evolution

##### 4.4.1. Crustal thickness and related structural features in the Qinling Orogenic Belt

Hu et al. (2017a) provided a method by which to estimate the crustal thickness (Moho depth) of continental collisional belts and applied it to the Qinling Orogenic Belt. In this paper, we added some new data and recalculated the Mesozoic Moho depth of the Qinling Orogenic Belt (Fig. 17; Table 5).

Based on our calculation, the North Qinling Belt had a quite uniform (~50 km) Moho depth during the Mesozoic, suggesting that continental collision may have had little influence on the North Qinling Belt, which is also supported by the following evidence (Fig. 17A). First, the paucity of magmatism in the North Qinling Belt and the absence of significant deformation during the early Mesozoic in the North Qinling Belt

indicate that interactions between continental blocks were not intense (Fig. 3; Dong et al., 2018; Li et al., 2007; Li et al., 2013). Second, major thrust faults and folds in the North Qinling Belt were not formed in the Mesozoic but were predominantly formed in the Paleozoic (Dong et al., 2018; Li et al., 2013). Third, the exhumation history of the basement rocks in the North Qinling Belt suggests no uplift or exhumation during the early Mesozoic (Dong et al., 2018). Therefore, it is reasonable to infer that the North Qinling Belt was generally stable during the early Mesozoic (G.-L. Wu et al., 2014; Dong et al., 2018). The present crustal thickness in the North Qinling Belt (~40 km) is thinner than our estimates for the Moho depth during the early Mesozoic, indicating crustal thinning and extension during the Cretaceous to Cenozoic (Fig. 17A; Hu et al., 2006).

The South Qinling Belt, as the locus of continental collision, showed significant changes in crustal thickness during the Mesozoic. The Moho depth increased from the early to middle Triassic at a slow rate from

**Table 4**  
Parameters used for zircon Hf-O isotopic modeling.

Assimilation and fractional crystallization (AFC) model				
D(Hf) = 0.42	r = 0.7	$\Delta O = -1.6$	Hf (ppm)	$\epsilon_{\text{Hf}}(t)$
Low $\delta^{18}\text{O}$ end member 1 (curve 1)			6	+6.0
Low $\delta^{18}\text{O}$ end member 2 (curve 2)			2	+2.0
High $\delta^{18}\text{O}$ end member 1 (curve 1 and 2)			4	-15.0
Simple mixing model				
			Hf (ppm)	$\epsilon_{\text{Hf}}(t)$
Low $\delta^{18}\text{O}$ end member 3 (curve 3)			6	+3.0
High $\delta^{18}\text{O}$ end member 2 (curve 3)			2	-15.0
Low $\delta^{18}\text{O}$ end member 4 (curve 4)			4	+0.0
High $\delta^{18}\text{O}$ end member 3 (curve 4)			10	-15.0

Note: D denotes the partition coefficient of Hf element; r is assimilation rate;  $\Delta O = \delta_{\text{zircon}} - \delta_{\text{magma}} = \delta_{\text{zircon}} - \delta_{\text{whole-rock}} = -0.0612 \times \text{SiO}_2 (\text{wt}\%) + 2.5$  (Valley et al., 2005), where  $\text{SiO}_2 = 62.5 (\text{wt}\%)$  is used in this study.

The partition coefficients are from <https://earthref.org/GERM/KDD/>.

The AFC model and simple mixing model are based on DePaolo (1981).

**Table 5**

Data subsets of calculated Moho depth in Qinling Orogenic Belt.

Location	Intrusion	Avg. longitude	Avg. latitude	Avg. age (Ma)	std	Sr/Y	std	Moho (km) <sup>a</sup>	Uncertainty	(La/Yb) <sub>N</sub>	std	Moho (km) <sup>b</sup>	Uncertainty
NQB	Cuihuashan	108.85	33.95	227.00	0.00	37.52	9.65	53	9	18.04	5.21	50	13
NQB	Guanshan	106.67	34.77	225.00	1.00					19.63	3.25	53	12
NQB	Laojunshan	107.67	34.15	214.00	0.00	33.78	9.22	51	9	18.60	2.09	51	11
NQB	Baoji	107.22	34.23	213.24	2.02	24.74	7.46	45	8	18.40	5.43	51	13
NQB	Qinlingliang	107.20	34.25	210.00	0.00	33.85	0.19	51	7	17.32	0.39	49	10
NQB	Mangling	110.46	33.83	158.44	1.94					19.24	3.14	52	11
NQB	Taibai	107.75	34.08	152.50	0.00					16.02	2.21	47	11
NQB	Muhuguan	109.50	34.00	149.00	0.00	39.38	2.98	55	7	20.18	4.23	54	12
SQB	Xiahe	102.72	35.21	245.82	2.09	28.97	7.38	48	8	12.61	2.09	40	11
SQB	Xiekeng	102.45	35.56	243.20	1.10	14.87	3.96	38	6				
SQB	Meiwu	103.32	34.99	242.00	1.15	26.99	9.65	46	9	14.44	4.06	44	13
SQB	Maixiu	101.83	35.27	234.00	0.00	12.63	2.57	37	6				
SQB	Wulong	108.25	33.50	232.43	0.98					18.24	4.49	51	12
SQB	Zhangjiaba	106.34	33.44	230.00	0.00	34.74	2.28	52	7	15.25	4.44	46	13
SQB	Wulong	108.25	33.50	227.00	0.00					15.56	1.92	46	11
SQB	Zhashui	109.25	33.63	225.00	0.00	28.61	4.95	47	7	14.53	4.55	44	13
SQB	Guangtoushan	106.63	33.36	224.00	0.00					15.25	4.12	46	12
SQB	Yanzhiba	108.50	33.42	222.00	0.00					22.94	4.03	57	12
SQB	Dongjiangkou	108.95	33.73	218.79	1.51					16.27	3.59	48	12
SQB	Xiba	107.20	33.67	218.50	0.52					16.69	4.16	48	12
SQB	Wulong	108.25	33.50	218.00	0.00					23.66	4.80	58	12
SQB	Caoping	109.52	33.78	217.63	3.45	33.44	6.65	51	8	13.30	4.78	42	14
SQB	Longcaoping	107.98	33.75	217.00	0.00	21.33	3.57	43	6				
SQB	Taoyuanpu	106.83	33.69	216.00	0.00					13.47	4.06	42	13
SQB	Huoshadian	106.93	33.53	215.00	0.00	50.99	6.50	62	9	15.44	2.74	46	11
SQB	Dongjiangkou	108.98	33.75	214.00	0.00					15.12	1.82	45	10
SQB	Huangzhuguang	105.65	33.95	214.00	0.00	38.15	1.91	54	7	12.15	0.62	39	10
SQB	Shahewan	109.71	33.76	212.83	1.85	45.87	8.59	59	9	19.41	2.61	52	11
SQB	Xichahe	107.75	33.47	212.00	0.00					14.36	5.53	44	15
SQB	Miba	105.83	33.50	211.00	0.00	36.63	6.34	53	8	18.30	2.76	51	11
SQB	Laocheng	108.35	33.50	210.33	0.58					38.49	7.16	71	14
SQB	Huayang	107.50	33.57	207.00	0.00					31.56	1.82	66	12
SQB	Erdaohexiang	106.75	33.23	202.00						24.65	7.46	59	14
SQB	Zhashui	109.24	33.63	200.92	1.38	24.11	8.66	44	8	14.82	3.89	45	12
SQB	Huayang	107.38	33.55	195.00	1.41					13.90	1.63	43	10
SQB	Longcaoping	107.96	33.67	189.00	0.00	24.01	2.63	44	6	15.78	4.47	47	13
SQB	XWY	109.63	33.59	147.23	2.28					12.19	2.61	40	11
SQB	BCTS	109.60	33.50	144.82	1.25					16.16	3.24	47	12
SQB	XY	109.83	33.63	142.50	0.53					17.07	4.32	49	12

Notes: SQB - South Qinling Belt; NQB - North Qinling Belt; Avg. - Average; std. - standard deviation.

XY - Xiaguanfang-Yuanzijie; XWY - Xiaohekou-Wagou-Yuanjiangou; BCTS - Baishagou-Chigou-Tudigou-Shuangyuangou.

n denotes the value is normalized to chondritic values of McDonough and Sun (1995).

<sup>a</sup> represents estimated Moho depth based on Sr/Y value.<sup>b</sup> represents estimated Moho depth based on (La/Yb)<sub>N</sub> value.

~35–45 km to ~40–50 km from ~250 to 230 Ma (Fig. 17B). Thermochronological and geochronological studies suggest that initial deformation started at ~250–230 Ma in the eastern South Qinling Belt and is slightly younger (~230–220 Ma) in the western South Qinling Belt, reflecting the obliquity of the collisional process (Fig. 17C; Hacker et al., 2004; Ratschbacher et al., 2003; Oh and Kusky, 2007; Wang et al., 2019). The Moho depth increased significantly after ~225 Ma and reached a maximum of ~60–70 km during 220–210 Ma in the South Qinling Belt (Fig. 17B). The crustal thickening took place mainly in the middle and eastern South Qinling Belts, which is also supported by the existence of minor terrestrial sedimentation in the western South Qinling Belt during the late Triassic (Li et al., 2014; Hu et al., 2017a). Detailed structural studies revealed that the crustal deformation and surface uplift mainly happened during late Triassic in the middle and eastern South Qinling Belt (Liang et al., 2015; Li et al., 2017). The orientation of the major structures in the South Qinling Belt reflect a change in the direction of compression from NE-SW to NW-SE during this stage (Hacker et al., 2004; Y. Li et al., 2015; Ratschbacher et al., 2003). The oblique collision and block rotation controlled the change of the compressional direction and coeval transpressional strike-slip movement during this stage (J. Li et al., 2018; Liang et al., 2015; G.-L. Wu et al., 2014). Locations near the rotation axis will be under the compressional stress for a longer time, resulting in a thicker crust. Together

with distribution of magmatic rocks, the addition of voluminous magmatism may have also contributed to the crustal thickening (D.C. Zhu et al., 2015). The crustal thickness in the South Qinling Belt (mainly the middle segment) decreased after ~210 Ma and reached ~45 km at ~200 Ma (Fig. 17B; H. Li et al., 2016; Hu et al., 2017a; Song et al., 2018). Some granitoid intrusions in the South Qinling Belt exhibited fast cooling rates (~20 °C/Ma) after their emplacement (< 210 Ma), indicating rapid regional uplift and denudation rates (F. Wang et al., 2014). The exhumation of granulite in the South Qinling Belt during this stage is also documented (Z.Q. Zhang et al., 2002). Transtensional and extensional faults formed locally in the Qinling Orogenic Belt during ~210–180 Ma (Liang, 2009; Yang et al., 2015b). Because of the absence of mountain roots or mafic lower crust under the Qinling Orogenic Belt at present (Song et al., 2018; Teng et al., 2014), crustal thinning during this stage may have been accomplished by delamination and gravitational collapse.

#### 4.4.2. Metamorphism in the Qinling Orogenic Belt and Tongbai-Hong'an-Dabie-Sulu Orogenic Belt during the early Mesozoic

In the Qinling Orogenic Belt, the HP metamorphism is documented by greenschist to blueschist-facies metamorphism (ca. 0.4–0.8 GPa; 350–450 °C) in the northern Wudang core complex (Fig. 18A, F and G; Eide and Liou, 2000; Ratschbacher et al., 2003). High-pressure granulite

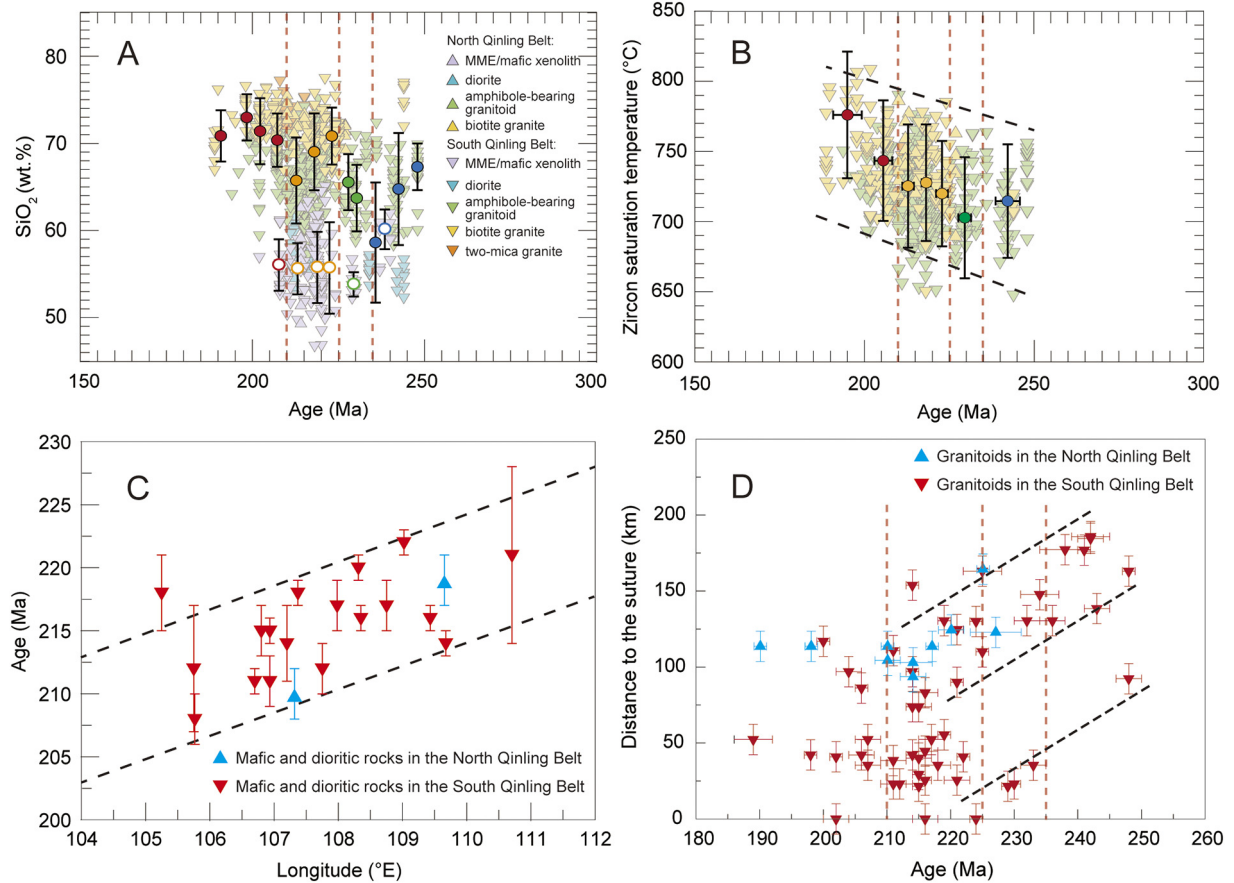


**Fig. 16.** (A) Plot of  $\text{SiO}_2$  versus age of rocks formed during different stages in the Qinling Orogenic Belt. The circle with an error bar represents the median value with the standard deviation. (B) The zircon saturation temperature versus age diagram for granitoids formed during different stages in the Qinling Orogenic Belt. The circle with the error bar represents the average value with the standard deviation. (C) Age versus longitude diagram for mafic and dioritic rocks formed during Stage III and IV in the Qinling Orogenic Belt. (D) Age versus distance to the suture of granitoid intrusions in the Qinling Orogenic Belt. Age data are presented as the weighted mean age with  $2\sigma$  errors. The data are cited from Supplementary Information 4.

in the Mianlue suture zone ( $800$ – $860$   $^{\circ}\text{C}$ ,  $1.2$ – $1.5$  GPa) experienced retrogression at  $\sim 215$  Ma (Fig. 18F and G; Liang et al., 2013). The amphibolite to granulite facies metamorphism ( $720$ – $780$   $^{\circ}\text{C}$ ,  $0.6$  GPa) in the Foping area is related to the crustal thickening during continental collision (Fig. 18A, F and G; Dong and Santosh, 2016; Wei et al., 1998; Yang et al., 1999; Z.Q. Zhang et al., 2002). The granulite-facies metamorphism occurred around 220 Ma and continued until  $\sim 205$ – $195$  Ma (Chen et al., 2019; Liu et al., 2019; Yang et al., 1999).

The Tongbai-Hong'an-Dabie-Sulu Orogenic Belt, on the other hand, preserves HP-UHP terranes (Ames et al., 1996; Ayers et al., 2002; Cheng et al., 2011; Feng et al., 2020; Liu and Liou, 2011; Schmidt et al., 2008, 2011; Wang et al., 2010; L. Wang et al., 2014; Xia et al., 2018; Zhang et al., 2009; Zheng et al., 2018; Zhou et al., 2015). The Tongbai HP blueschists and eclogites ( $460$ – $610$   $^{\circ}\text{C}$ ,  $1.3$ – $2.0$  GPa), and the Hong'an-Dabie-Sulu UHP eclogites (coesite-bearing) ( $520$ – $650$   $^{\circ}\text{C}$ ,  $2.5$ – $2.9$  GPa for Hong'an;  $630$ – $850$   $^{\circ}\text{C}$ ,  $2.8$ – $3.8$  GPa for Dabie;  $680$ – $880$   $^{\circ}\text{C}$ ,  $2.9$ – $4.3$  GPa for Sulu) record the evolutionary process of subducted continental crust (Figs. 2 and 18; Xu et al., 2003; Wu and Zheng, 2013; Zheng et al., 2018). Geochronological data show that the UHP prograde metamorphism occurred at  $\sim 255$ – $235$  Ma (Fig. 18B-E; Liu and Liou, 2011; Schmidt et al., 2011; Zhang et al., 2009; Zheng et al., 2018; Zhou et al., 2015). The earliest HP rocks ( $\sim 255$  Ma) are described from the Tongbai Orogen (Unit I), where is proposed to be site of the initial collision (X. Liu et al., 2008). However, we suggest that this could be the result of the shallower subduction depth in the Tongbai Orogen. Unit I started exhumation, whereas at the same time the continental subduction continued in the Dabie-Sulu-Hong'an Orogen. This implication is supported by the time of the peak metamorphism in the

Dabie-Sulu-Hong'an Orogen, which is coeval with the retrogression time of HP rocks (unit I) in the Tongbai Orogen (Fig. 18; Liu and Liou, 2011; Wu and Zheng, 2013; Zhou et al., 2015). The recrystallization of eclogite was at approximately 225–215 Ma, and amphibolite-facies retrogression occurred at  $\sim 215$ – $200$  Ma (Fig. 18; F.L. Liu et al., 2006; Zhao et al., 2006; Zheng et al., 2018).

The compiled data suggest that metamorphic pressures decreased from the Sulu-Dabie-Hong'an-Tongbai Orogenic Belt to the Qinling Orogenic Belt (Figs. 2 and 18G; Liu et al., 2010; X. Liu et al., 2015). Liu et al. (2010) proposed that the differences in metamorphic pressure reflect the continental subduction depth decrease from the east to the west. Some researchers proposed that the lack of HP-UHP rocks in the Qinling Orogenic Belt might be a result of limited exhumation and/or exposure (Qin et al., 2010a, 2013). However, the exposure of lower crustal granulites and the significant uplift and denudation since the Mesozoic indicate that the exhumation of UHP rocks should have been viable if they existed (Hu et al., 2006; F. Wang et al., 2014; Wei et al., 1998). Therefore, we consider that the absence of UHP rocks in the Qinling Orogenic Belt might have resulted from lack of deeply subducted continental crust, which may be related to the soft collision in the Qinling Orogenic Belt caused by the rotation of the South China Block (Liu et al., 2010; X. Liu et al., 2015; Zhao and Coe, 1987; Zhu et al., 1998). Moreover, the Qinling Orogenic Belt has high geothermal gradients of  $\sim 20$ – $30$   $^{\circ}\text{C}/\text{km}$  compared to the Sulu-Dabie-Hong'an-Tongbai Orogen ( $\sim 5$ – $10$   $^{\circ}\text{C}/\text{km}$ ) (Figs. 2 and 18G). The hot regime in the Qinling Orogenic Belt contributes to the extensive magmatism. The cold regime in the Sulu-Dabie-Hong'an-Tongbai Orogen is related to the deep subduction of the

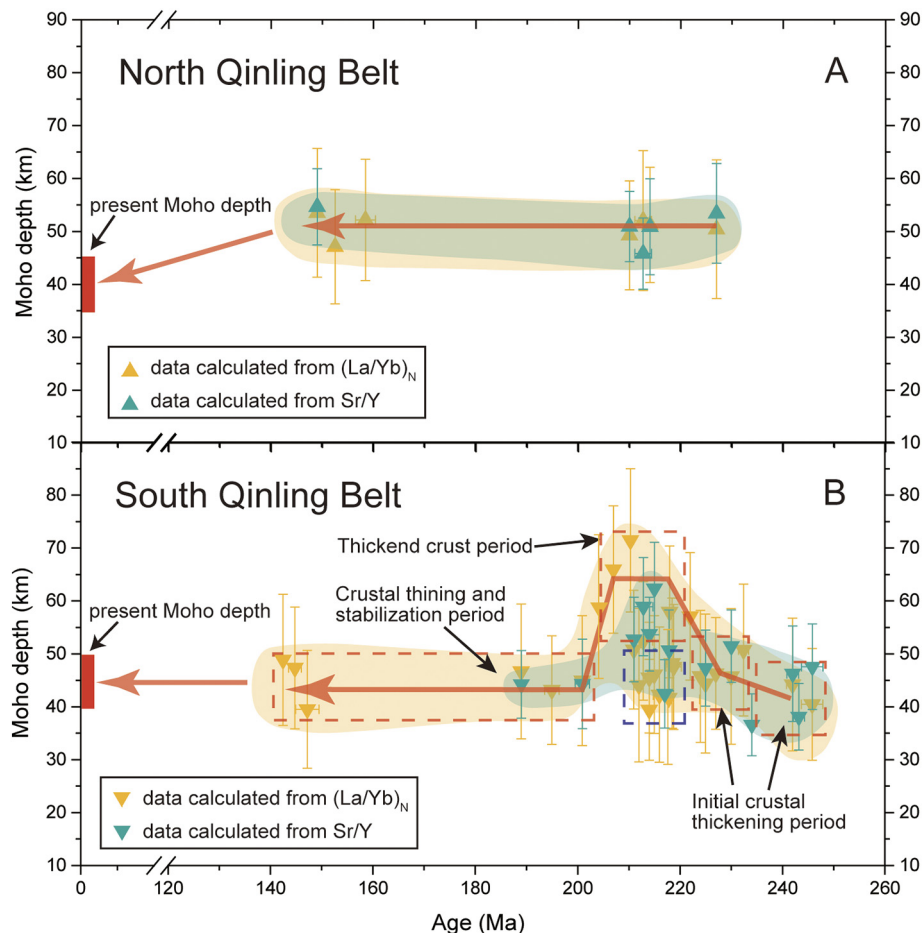


**Fig. 17.** Changes of the calculated crustal thickness from Sr/Y and  $(\text{La}/\text{Yb})_N$  over time for the North Qinling Belt (A) and South Qinling Belt (B) (modified after Hu et al., 2017a). Data used for calculation are listed in Table 5. See the text for details.

continental crust (Schmidt et al., 2011; Zhang et al., 2009; Zheng, 2008; Zheng et al., 2018).

The geochronological data for the metamorphism indicate that the prograde metamorphism in the Tongbai-Hong'an-Dabie-Sulu Orogenic Belt was coeval with the Stage I magmatism in the Qinling Orogenic Belt. The timing of the peak metamorphism of the Tongbai-Hong'an-Dabie-Sulu Orogenic Belt is generally the same as that of Stage II magmatism. The timing of HP recrystallization and retrogression was contemporaneous with granulite facies metamorphism and Stage III-IV magmatism in the Qinling Orogen (Fig. 18A-E). Accordingly, in combination with paleomagnetic data, an oblique subduction-collision process is well constrained here (Zhao and Coe, 1987; Zhu et al., 1998; Liu et al., 2010; X. Liu et al., 2015). Initial continental collision occurred in the eastern Dabie-Sulu Orogen in late Permian, while the oceanic subduction continued in the Qinling Orogenic Belt. As the subducted continental crust in the Dabie-Sulu area reached depths of up to ~120 km, the continental collision started in the Qinling Orogenic Belt and inhibited magmatism. Afterwards, high geothermal gradients in the Qinling Orogenic Belt promoted intense magmatism and granulite facies metamorphism. These were coeval with the retrogression of the HP/UHP rocks and minor alkaline magmatism and migmatization in the Tongbai-Hong'an-Dabie-Sulu Orogenic Belt, indicating a transition from compression to extension along the whole orogenic belt.

#### 4.4.3. Sedimentation in the hinterland and foreland basin systems

The sedimentation in the forearc-hinterland basin systems show lengthwise and horizontal differences in sedimentary facies. In the

western South Qinling Belt, a large range of Early to Middle Triassic sandstones show active continental margin affinities with coeval intermediate to felsic volcanic rocks, reflecting a forearc basin setting (Fig. 4; Guo et al., 2012; Z. Yan et al., 2014; Yan et al., 2012, 2020; Li et al., 2013). The Upper Triassic strata in the western South Qinling Belt are composed of sandstones and conglomerates with interbedded volcanic rocks, which represent terrigenous deposition (Fig. 4; Li et al., 2014; S.M. Zhang et al., 2014). In the middle and eastern South Qinling Belt, Early Triassic carbonates are locally exposed and are conformably overlain by the Middle Triassic sandstones and siltstones, and the Upper Triassic strata are missing, indicating gradual tectonic uplift (Fig. 4; Lai et al., 1995; S.M. Zhang et al., 2014). The changes of sedimentary facies along the South Qinling Belt indicates that the uplift was westward. As for the North Qinling Belt only the terrestrial Upper Triassic Wulichuan Formation is exposed (Fig. 4; S.M. Zhang et al., 2014). These geological features suggest that the uplift of the South Qinling Belt started no later than the late Triassic and that the uplift began from the east to the west.

The foreland basin system in the northern margin of the SCB mainly shows horizontal diachronous changes of the sedimentary facies (Fig. 19). The Middle Triassic Badong Formation in the Zigui, Dangyang and Southeast Hubei Basins consists of siltstone and mudstone with carbonate nodules, representing a tidal flat environment (Fig. 19; Liu et al., 2005; Liu and Zhang, 2013). The Middle Triassic strata in the western Sichuan Basin are composed of shallow marine carbonate, reflecting a shallow marine environment (Fig. 19; Meng et al., 2005). The missing upper part of the Badong Formation in the Dangyang and Southeast

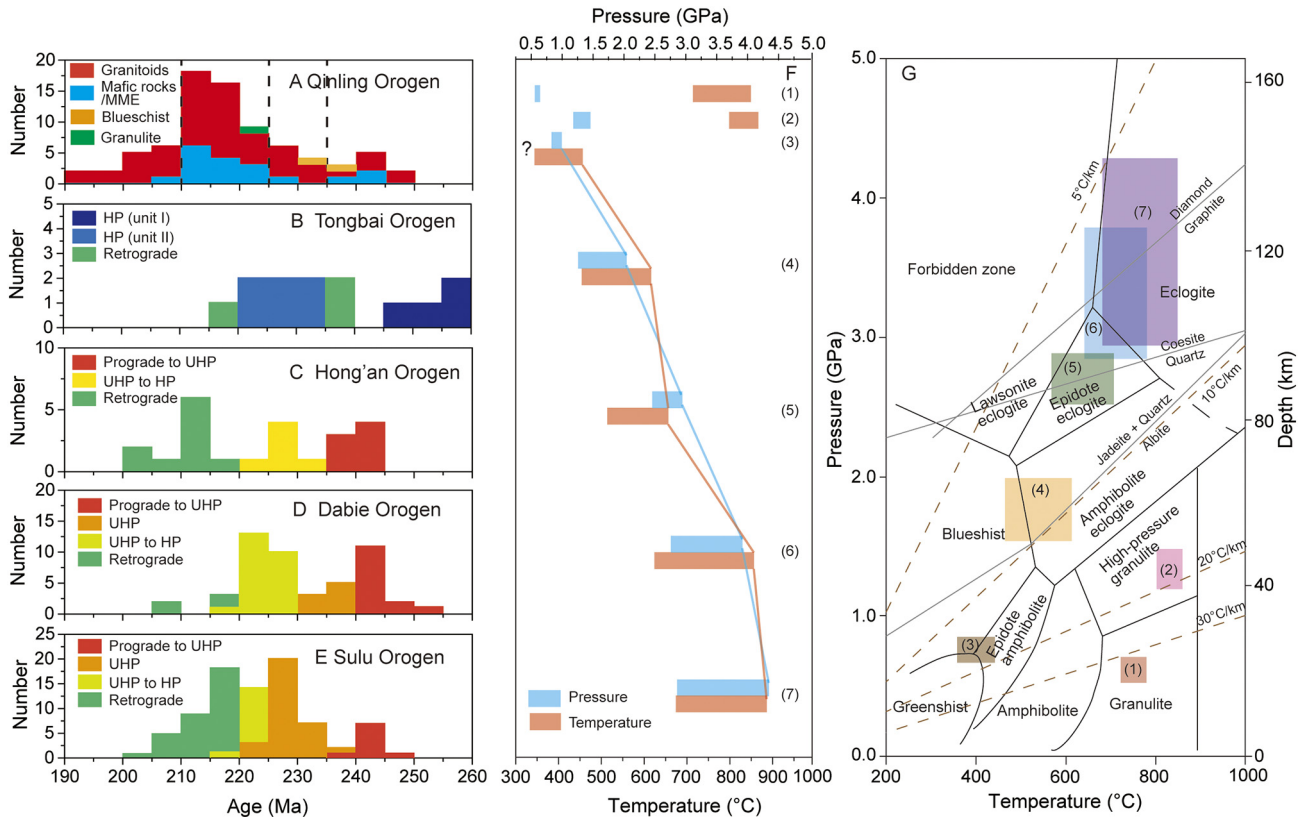


**Fig. 18.** Comparison of metamorphism and magmatism in the Qinling Orogenic Belt and Tongbai-Hong'an-Dabie-Sulu Orogenic Belt. (A–E) Histograms of the crystallization ages of magmatic rocks and metamorphic ages of HP-UHP rocks in the Qinling Orogenic Belt and THDSOB. (F and G) P-T conditions of peak metamorphism in the Qinling Orogenic Belt and Tongbai-Hong'an-Dabie-Sulu Orogenic Belt. The data are cited from Ames et al. (1996); Ayers et al. (2002); Chen et al. (2007); Cheng et al. (2008, 2010, 2011); X.Y. Gao et al. (2011); Hacker et al. (2006); Li et al. (2000); F.L. Liu et al. (2004); X.C. Liu et al. (2004); F.L. Liu et al. (2006); D. Liu et al. (2006); F.L. Liu et al. (2008); Liu et al. (2010, 2012); Liu and Liu (2011); Mattauer et al. (1985); Ratschbacher et al. (2003); Schmidt et al. (2008); Wan et al. (2005); Y.B. Wu et al. (2008); Wu et al. (2011); Wu and Zheng (2013); Zhang et al. (2009); Zhao et al. (2006); Zheng et al. (2005); Zheng (2008); Zheng et al. (2018) and references therein. The number (1 and 2) mean granulite in the Qinling Orogenic Belt; the number (3) means blueschist in the Qinling Orogenic Belt; and the number (4–7) mean eclogite in the Tongbai, Hong'an, Dabie Orogen, and Sulu Orogenes, respectively.

Hubei Basins and eastern Zigui Basin indicates that tectonic uplift started during the middle Triassic (Fig. 19; Li et al., 2008). The deposition of Upper Triassic strata in the Dangyang and Southeast Hubei Basins suggests a change from a delta/lake to a river environment (Fig. 19; Chen et al., 2011; Liu and Zhang, 2013). However, in the Zigui Basin, no river deposition was identified during the late Triassic (Chai et al., 2016). As for the Sichuan Basin, a transition of the sedimentary environment from shallow marine (Ma'an tang Formation) to tidal flat (Xiaotangzi Formation), and then to delta/lake (Xujiache Formation) during the Triassic is recognized (Fig. 19; Meng et al., 2005; Shi et al., 2012; Zheng et al., 2009; Zou et al., 2003). Overall, the change time of sedimentary environment from marine to continent shows a younging trend from east to west (Fig. 19). Therefore, the closing times of oceanic basins and the tectonic uplift times of the foreland become younger from east to west during the Triassic to early Jurassic (Li et al., 2014; Zhao et al., 2020). The paleocurrent directions show that the provenance of the Upper Triassic to Lower Jurassic strata are from the Qinling Orogenic Belt (Chai et al., 2016; Liu et al., 2005; Liu and Zhang, 2013). The tectonic uplift of the hinterland should have been at the middle Triassic to provide materials to the foreland basins.

The western Songpan-Ganzi Basin is characterized by Triassic deep-water turbidite sedimentation, which is proposed to be an analogue to the present Mediterranean Sea (Gürer and van Hinsbergen, 2019; Jian et al., 2019; Pullen et al., 2008; Spakman et al., 2018). Provenance and paleocurrent studies reveal that sediments were transported from the northern/northeastern Qinling Orogenic Belt from over 1000 km away (S. Liu et al., 2015). This finding also supports the uplifting of the Qinling Orogenic Belt during the middle Triassic.

As summarized above, it clearly reflects a westward-younging migration of the closure of the ocean basin and filling of the foreland basins (Fig. 19). The westward-directed lateral migration of depocenters in the foreland basin system also reflects the diachronous closure of the Paleo-Tethys Ocean and oblique collision processes (Liu and Zhang, 2013; S. Liu et al., 2015; Malatesta et al., 2013). Considering that sedimentary records usually represent an upper time limit, the results of the collision times obtained from sedimentary records are similar to those from the metamorphic rocks discussed above. Therefore, the collision time is proposed to be the late Permian to early Triassic in the east and the middle to late Triassic in the west. The increasing proportions of late Triassic igneous detrital zircons (~225–200 Ma) from the Upper Triassic to Early Jurassic strata in the foreland basins demonstrate that mountain building and uplifting of the Qinling Orogenic Belt started during the middle Triassic and was increasingly denuded from the late Triassic to Jurassic (Chai et al., 2016; Liu et al., 2005; Meng et al., 2005, 2019). This finding is in accordance with the estimated crustal thickness changes as previously mentioned (Fig. 17). The occurrence of the Upper Triassic strata in the North Qinling Belt also illustrates that the North Qinling Belt did not undergo strong tectonic uplift and shortening during the Triassic continental collision. The high mountain of the South Qinling Belt was built during the middle to late Triassic and provided a great deal of materials to the foreland, hinterland and continental interior basins (Meng et al., 2019). The Upper Jurassic terrestrial deposits in the South Qinling Belt indicate that regional extension was developed there, which is also consistent with the inferences from the estimated crustal thickness and metamorphic records (Figs. 17 and 18).

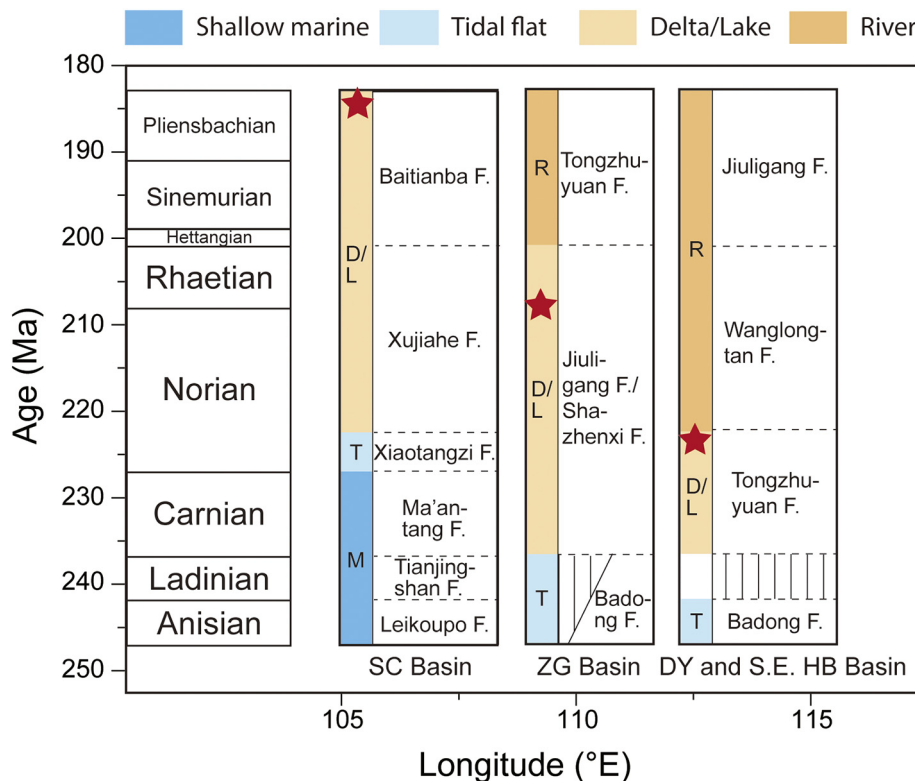


**Fig. 19.** Middle Triassic through Lower Jurassic stratigraphic unit names with sedimentary facies and foreland basin names with locations across the northern Yangtze region (modified after Chai et al., 2016; Chen et al., 2011; Liu et al., 2005; Liu and Zhang, 2013; Meng et al., 2005). The vertical ruled pattern represents unconformities and missing strata. The red star represents depocenters during different stages.

## 5. Tectonic evolution of the Qinling Orogenic Belt during the early Mesozoic

Based on our overview on the magmatism, metamorphism, sedimentation, structures and crustal thickness of the Qinling Orogenic Belt during the early Mesozoic, we present a synthesis of the tectonic evolution of the Qinling Orogenic Belt and related outcomes for different aspects.

### 5.1. Stage I

According to the metamorphic and sedimentary data presented above and paleomagnetic data, the initial continental collision occurred in the late Permian in the Dabie-Sulu Orogenic Belt (Figs. 18 and 19; ~260–250 Ma; Zhao and Coe, 1987; Zhu et al., 1998). At the same time, the magmatic and sedimentary records indicate that a remnant ocean still existed in the west Qinling (S. Liu et al., 2015; Yan et al., 2020). In the Dabie-Sulu Orogen, the continuing subduction of continental crust prevented the melting of lithospheric mantle, and the magmatism was mainly distributed in the western South Qinling Belt during this stage (Figs. 3 and 5; Zheng et al., 2013). The perpendicular distance of granitoid intrusions to the suture zone becomes closer from Stage I to Stage II (Fig. 16D), which was most likely caused by the slab roll-back of the subducted oceanic slab (Kusky et al., 2014; X. Zhu et al., 2015; D.C. Zhu et al., 2015). We speculate that flat subduction happened in the middle and eastern South Qinling Belt while the slab roll-back started in the western South Qinling Belt, resulting in such a distribution pattern of the magmatic rocks. The flat subduction caused the uplift of the upper plate (Horton, 2018), and this could have resulted in the lack of deposition of Upper Permian to Middle Triassic strata in the middle and eastern South Qinling Belt compared to the abundant coeval deposition in the western South Qinling Belt (Fig. 2; Horton,

2018; Yan et al., 2020). Therefore, the west Qinling should be associated with oceanic subduction, whereas continental collision was initiated in the Dabie-Sulu area during ~250–235 Ma (Fig. 20A).

### 5.2. Stage II

Continental collision started along the Qinling Orogenic Belt between ~235–225 Ma. The reasons behind this conclusion are: (1) the existence of a magmatic gap during this stage (Fig. 5); (2) no Upper Triassic strata present in the hinterland basins; (3) the transition of sedimentary facies from marine to nonmarine in the foreland basins (Fig. 19); (4) blueschist-facies metamorphism and thrust/folding deformation in the Wudang area during ~237 to 226 Ma (Hacker et al., 2004; Mattauer et al., 1985; Ratschbacher et al., 2003; Wang et al., 2019); (5) the deformation of ophiolites (~227 to 223 Ma) from the Mianlue suture zone in the western South Qinling Belt (Li et al., 1999; Chen et al., 2010); and (6) the emplacement of the Guangtoushan intrusion (~224 to 218 Ma) in the middle South Qinling Belt, crossing the suture zone (Fig. 16D; Deng et al., 2016). Based on these lines of evidence, we suggest that continental collision in the Qinling Orogenic Belt started prior to ~227 Ma in the western Qinling Orogen and ~235 Ma in the eastern Qinling Orogen (Fig. 20B). Magmatic rocks during this stage were located closer to the suture zone than those were formed during the Stage I (~250–235 Ma), representing continued slab roll-back (Fig. 16D; Li et al., 2013). The slightly increased crustal thickness during this stage is consistent with the uplift and crustal deformation in the South Qinling Belt (Fig. 17).

### 5.3. Stage III

A significant magmatic flare-up event occurred during the late Triassic (~225–210 Ma), forming widespread granitoid intrusions with

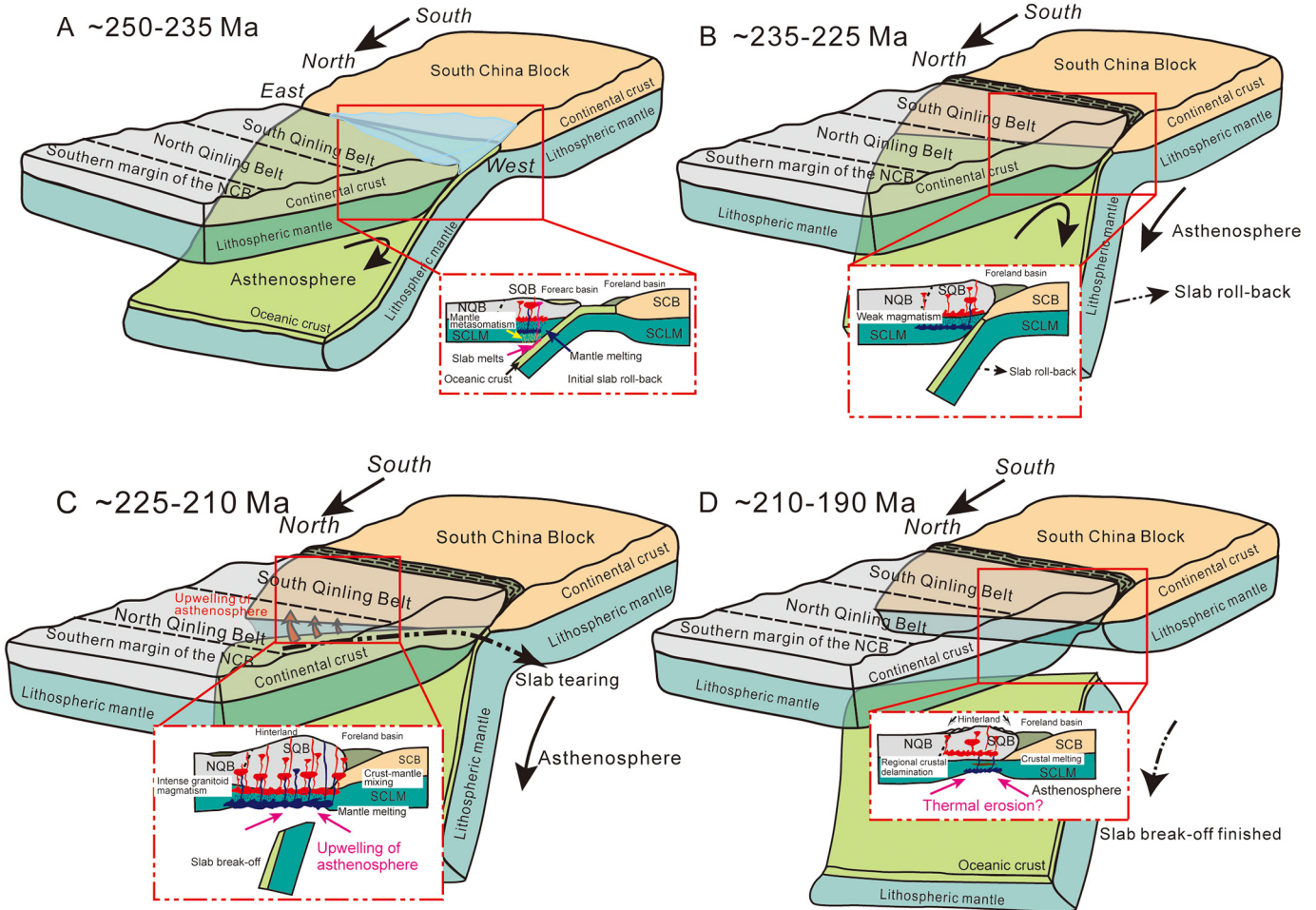


**Fig. 20.** Schematic diagram of the tectonic evolution model during the early Mesozoic in the Qinling Orogenic Belt. (A) Continental collision at Tongbai-Hong'an-Dabie-Sulu Orogenic Belt and oceanic subduction in the Qinling Orogenic Belt during ~250–235 Ma. (B) Continental collision and slab roll-back in the Qinling Orogenic Belt during ~235–225 Ma. (C) Westward slab break-off together with slab roll-back in the Qinling Orogenic Belt during ~225–210 Ma, inducing upwelling of the asthenosphere and melting of the sub-continental lithosphere and continental crust. (D) Orogenic gravitational collapse and regional crustal delamination in the Qinling Orogenic Belt during ~210–190 Ma. See the text for details.

abundant MME. The strong mantle–crust interaction suggests that the crustal heat flow became quite high during this stage, which is also evidenced by the granulite facies metamorphism in the South Qinling Belt during this stage (Fig. 18; Liang et al., 2013; Yang et al., 1999). However, the melting temperature was not very high due to fluid and melt buffer actions under the relatively high water content in the magma. The high crustal heat flow during this stage is interpreted to be related to slab break-off (Deng et al., 2016; S.W. Liu et al., 2011; Jiang et al., 2010; Qin et al., 2013; Sun et al., 2002; Yang et al., 2012a), slab roll-back (Brun and Faccenna, 2008; Zheng et al., 2018; Jiang et al., 2010; Sternai et al., 2014), or lithospheric delamination (Gögüş et al., 2017).

Slab roll-back is generally associated with regional extension of the upper plate (e.g., Kusky et al., 2014; Wortel and Spakman, 2000), which is contrary to the geological observations in the Qinling Orogen during this time. The perpendicular distance between the granitoid intrusions and the suture zone show no trend during this period, and the suddenly widespread magmatism during this stage was clearly related to a special mechanism (Fig. 16D). Moreover, the increasing sediment input into the foreland basins indicates that high mountains were built during this stage (S. Liu et al., 2015; Meng et al., 2019). Therefore, we consider that slab roll-back by itself is not enough to account for the tectonic history during Stage III. Although lithospheric delamination could cause massive melting of the crust and mantle and induce tectonic uplift according to some authors (Kay and Kay, 1993; Lustrino, 2005),

but not others (Ducea et al., 2013), the precondition of a thickened crust or lithosphere is questionable in the Qinling Orogenic Belt. According to our estimation, the crust was not thick enough to be delaminated before this stage (Fig. 17). Moreover, the contemporary Upper Triassic deposition and granitoid magmatism in the North Qinling Belt were contrary to the outcomes of the lithospheric delamination, suggesting that no tectonic uplift occurred in the North Qinling Belt during this stage. Therefore, we argue against lithospheric delamination during this stage. Another potential process is the forced delamination of the continental mantle lithosphere by shallow subduction of the oceanic lithosphere (Bird, 1979). This process can result in extensive magmatism, surface uplift, exhumation of the deeply subducted continental crust, and strong magmatism on the lower plate (Duretz and Gerya, 2013). However, only a few intrusions are exposed in the lower plate (Bikou Terrane), and the strong continental lithosphere of the old and cold SCB was unlikely to be decoupled during collision (Fig. 3; Duretz and Gerya, 2013; Gögüş and Ueda, 2018; Magni et al., 2013). Hence, this mechanism also does not match the geological observations.

Here, we propose a model that combines both slab roll-back and slab break-off. When applying the slab break-off model, many aspects need to be considered (Garzanti et al., 2018). Modeling studies suggest that continued slab roll-back would cause very steep dip angles of the slab, which favor slab break-off (Menant et al., 2016). Rheological juxtaposition of the strong lithosphere of the SCB and oceanic lithosphere could

cause slab break-off during collision (Dai et al., 2018; Magni et al., 2013; Chowdhury et al., 2017). A recent numerical model suggests that slab break-off commonly occurs in locations too deep to generate extensive magmatism, which may be the case in the Dabie-Sulu Orogen (Freeburn et al., 2017). In the Dabie-Sulu Orogen, deep continental subduction depths show that the slab break-off depth should have been deep, prohibiting the formation of extensive magmatism. The magmatism in the Dabie-Sulu Orogen mainly formed during the Late Mesozoic, reflecting a different melting mechanism compared to the Qinling Orogenic Belt (Zhao et al., 2018; Zhu et al., 2018). The continental collision was diachronous along the Dabie-Sulu to Qinling Orogenic Belt, and the depths of break-off may have been different (Liu et al., 2010). Because of the lack of UHP rocks, we prefer to interpret the depth of slab break-off as relatively shallow. After the slab break-off, the deep subduction of continental crust was hampered due to the lack of slab pull in the Qinling Orogenic Belt, which may have also caused the retrogression of HP granulite in the suture zone (Liang et al., 2013). The shallow slab break-off could have generated extensive crustal and mantle melting with rapid tectonic uplift (Atherton and Ghani, 2002; Duretz et al., 2011; Schildgen et al., 2014; F. Wang et al., 2014).

Modeling studies examined oblique collisions and suggested that slab break-off can begin at the edge where the collision starts and propagate toward the other end (Boutelier and Cruden, 2018; van Hunen and Allen, 2011; Wortel and Spakman, 2000). This prediction is broadly consistent with the collisional process in the Qinling-Dabie Orogen. The break-off happened at ~10–20 Ma after the onset of collision and the propagation rate was ~10–15 cm/year in the Qinling-Dabie Orogen. The results herein are basically the same as those of the numerical studies (Boutelier and Cruden, 2018; Duretz et al., 2011). Regional extension and uplift may be restricted to the area above where slab break-off occurred (Boutelier and Cruden, 2018). These modeling results are in good accordance with the geological observations in the Qinling-Dabie Orogen. All the magmatism is distributed north of the Ningshan Fault, which may indicate that the front location of the subducted oceanic crust is just along this fault zone (Fig. 3). Therefore, we propose that westward slab break-off (tear) together with slab roll-back occurred during ~225–210 Ma (Fig. 20C).

#### 5.4. Stage IV

Mantle-derived magmatism waned significantly after ~210 Ma, and the granitoid magmatism was characterized by high silica contents with fractionated features in the Qinling Orogenic Belt (Figs. 5 and 16). The magma source was dominated by middle crustal metasedimentary rocks, and the melting temperature of the metasedimentary rocks was similar to our calculation (720–800 °C), reflecting a decreased water content in the source (Fig. 16; Collins and Richards, 2008). The lack of magma derived from metaigneous rocks and lithospheric mantle indicates that the mantle heat flow was not high enough. The granulite-facies metamorphism during this stage confirmed the continued high heat flow and dry environment in the lower crust (Chen et al., 2019; Liu et al., 2019). The decompression of the upper continental crust promoted the further partial melting of the crustal materials, especially metasedimentary rocks (Liu et al., 2019). We interpret the magmatism during this stage to be related to the extensional collapse of the Qinling Orogenic Belt (Fig. 20D). The extensional detachment faults, intermontane basins and deposition during the Lower Jurassic in the South Qinling Belt indicate regional orogenic extension during ~205–160 Ma (Fig. 4; Yang et al., 2016). This implication is also in accordance with our calculation of the crustal thickness during this stage (Fig. 17). Geophysical data show that the crust of Qinling Orogenic Belt is mainly made of intermediate to felsic rocks, indicating that lower crustal delamination happened after crustal thickening (Guo and Chen, 2016; Song et al., 2018; Teng et al., 2014). The scale of crustal delamination may have also been restricted due to the limited crustal thickening area, which is supported by the absence of extensive crustal melting

during this stage and by the magmatism being mainly distributed in the middle South Qinling Belt, unlike the Himalaya orogen (Chung et al., 2005). Delamination shortly after slab break-off could have resulted in isostatic uplift, increased gravitational potential energy, and driven extension in the orogen (Gögüs and Ueda, 2018).

#### 6. Critical features of oblique continental collisional orogens

The Qinling Orogenic Belt and its continuation in the Dabie-Sulu Orogen define an oblique continental collisional belt. Such an orogen has some typical features that contrast with subduction zones and head-on continent-continent collisional belts (e.g., the Himalayas) (Streule et al., 2010; Stern, 2002). Previous studies mainly focused on tectonic processes and structural deformations of oblique collisional orogens and determined that large strike-slip faults and extrusion of blocks are the most important features of an oblique collisional belt (England and Thompson, 1986; Godin et al., 2006; Harris et al., 1986; S. Li et al., 2018; Streule et al., 2010; Sylvester, 1998). However, other aspects are seldom evaluated. Some researchers mentioned that the oblique collisional process should be more magmatically active compared to those affected by orthogonal collision, e.g., the British Caledonides (Dewey and Strachan, 2003; Miles et al., 2016). The following are six critical features of oblique collisional orogens concluded based on our overview of the Qinling Orogenic Belt.

1. The spatial and temporal distribution of magmatism is asymmetric along the orogenic belt and melting mechanisms change during the oblique collision process. As the initial continental collision starts at one side, the magmatism will cease after collision and be prohibited by the deep continental subduction, whereas the subduction of the oceanic slab continues at the other side. Therefore, the distribution of arc-related magmatism is asymmetric. The magmatism in the area of deep subduction of the continent will be limited even during the exhumation stage. However, on the other side without deep subduction of the continent, intensive magmatism could be generated by the syn-collisional slab roll-back and break-off, e.g., the Caledonian orogen (Dewey and Strachan, 2003; Miles et al., 2016; Streule et al., 2010). With respect to the Zagros orogen, which is formed by an oblique collision between Eurasia and Arabia, there is no deep subduction of the continental crust (Kaban et al., 2018). The distribution of collisional-related magmatism also shows an asymmetric pattern in which the emplacement ages are older in the earlier collision area (Chiu et al., 2013; Lin et al., 2020). Therefore, the collisional-related magmatism is also asymmetric, and the melting mechanisms are distinct during different stages of continental collision.
2. The peak metamorphic pressure gradually decreases and the geothermal gradient increases from the initial collisional side to the other side. The cold subduction and deep slab break-off depth hinder the production of magma (Atherton and Ghani, 2002; Freeburn et al., 2017). In contrast, the shallow slab break-off depth not only increases the geothermal gradient but also promotes intensive magmatism (Atherton and Ghani, 2002; Freeburn et al., 2017). Such dual geothermal gradients coexisting simultaneously in the same belt is one of the most unique features of oblique collisional belts.
3. The deposition in foreland basins shows a diachronous feature. The changes of sedimentary facies from marine to terrestrial directly reflect the history of the closure of the oceanic basin and the uplift of foreland basins along the orogenic belt. This is one of the basic features of the oblique collisional belt, which has been observed in many belts (e.g., the Zagros orogen, Pirouz et al., 2015; the Mediterranean orogen, McCay and Robertson, 2012).
4. The deposition of hinterland basins and the thermochronological data of intrusions reflect differential uplift along the orogen. The uplift of the oblique collisional belt starts from initial collision side and gradually progresses toward the other side. The highest uplift rate is regional and is due to upwelling of the asthenosphere possibly induced by shallow slab break-off and subsequent delamination (Boutelier and Cruden, 2018).
5. Crustal thickening is not uniform along the strike of the orogen (e.g., the Zagros orogen, Shad

**Manaman et al., 2011**). The thickening of the crust is controlled by crustal deformation and underplated mafic magma. The stress field will change during the oblique collision process with block rotation (J. Li et al., 2018; Liang et al., 2015). Of course, the underplated mafic magma also provides a major contribution (X. Zhu et al., 2015; D.C. Zhu et al., 2015). 6. The delamination of the orogenic root and collapse of the orogen happen after crustal thickening. Unlike the Himalayan orogen with abundant post-collisional magmatism, the post-collisional magmatism could be weak due to limited and diachronous delamination (Chung et al., 2005; F. Wang et al., 2014). These features may be partially observed in the orogen and have variable changes due to different rheological properties and viscosities of the blocks and other physical parameters (e.g., the convergence rate and angle of collision) during continental collision (Andrić et al., 2018; Liao and Gerya, 2016; Vogt et al., 2017). By combining these features, we can reconstruct the evolutionary history of an oblique collision orogen.

## 7. Conclusions

The early Mesozoic magmatism (~250–180 Ma) in the Qinling Orogenic Belt is divided into four stages. The rock associations, melting conditions and magmatic mechanisms are distinct at different stages. Stage I magmatism is characterized by calc-alkaline andesites, diorites, and granitoids in the western South Qinling Belt. Stage II is recognized as a magmatic gap. Stage III magmatism is characterized by extensive granitoid intrusions with abundant coeval mafic rocks. Stage IV magmatism is characterized by dominantly high-silica granite derived from metasedimentary rocks. The primary magmatic source of granitoid rocks is the Proterozoic basement in the North Qinling Belt and South Qinling Belt. Mafic magma is derived from the metasomatized lithospheric mantle. Intracrustal magma mixing and fractionation contribute to the diverse geochemical composition of granitoids.

The collision between the SCB and NCB was oblique and diachronous along the Qinling-Dabie orogenic belt and can be subdivided into four stages according to their patterns of magmatism. The Qinling Orogenic Belt experienced oceanic plate subduction while deep continental subduction had already initiated in the Dabie-Sulu Orogen during Stage I (~250–235 Ma). Subduction-related magmatism and its emplacement moving toward the suture zone is related to slab roll-back process. The initial continental collision started at Stage II (~235–225 Ma) in the Qinling Orogenic Belt and was characterized by low-volume magmatism, a transition of sedimentary facies from marine to nonmarine in the foreland basins, and the gradual tectonic uplift and crustal thickening of the orogenic belt with compressional deformation. The continued slab roll-back and westward detachment of the oceanic slab during Stage III (~225–210 Ma) induced the upwelling of the asthenosphere and resulted in the extensive melting of metasomatized lithospheric mantle and lower crust, causing the significant crustal thickening, regional rapid uplift and transpressive strike-slip movement of the Qinling Orogenic Belt and coeval exhumation of HP-UHP rocks in the Tongbai-Hong'an-Dabie-Sulu Orogenic Belt. The rapid rate of denudation and extensional faults during Stage IV (~210–190 Ma) indicate the gravitational collapse and regional delamination of the thickened lower crust, producing high-SiO<sub>2</sub> granite with a limited input of mafic magma.

Six critical features of oblique-collisional orogens are inferred based on the Qinling-Dabie orogen. These features include the asymmetric distribution pattern of magmatism along the orogenic belt and distinct melting mechanisms over time; the peak metamorphic pressure gradually decreasing and the geothermal gradient increasing from the initial collisional side to the other side; the diachronous deposition in the foreland basins; the differential uplift history of the orogen; the non-uniform crustal thickening along the orogen; the regional delamination of the orogenic root and the collapse of the orogen after crustal thickening. These features can be applied to other orogenic belts to reconstruct their tectonic evolution and interpret asymmetrical phenomena along the belt.

Supplementary data to this article can be found online at <https://doi.org/10.1016/j.gr.2020.07.006>.

## Declaration of competing interest

The authors declare that they have no known competing financial interests or personal relationships that could have appeared to influence the work reported in this paper.

## Acknowledgments

Associated Editor Prof. Yunpeng Dong and four anonymous reviewers are thanked for their constructive and thoughtful reviews, which greatly improved the manuscript. We want to thank Li Chen, Bin Yang, and Libin Gu for help with CL imaging, whole-rock major and trace element analyses, Fang Ma, Xiaoxiao Ling, Xiaoping Xia, Mengning Dai, Honglin Yuan, and Zhaochu Hu for assistance with zircon U-Pb-Hf-O isotopic analyses. Our study gets much support from Zongqi Wang, Zhen Yan, Qiugen Li, Pengtao Yang, Ming Yan, Zhengbin Deng, Jinghao Fu, and Maojiang Wang in both field work and laboratory analysis. S.W.L acknowledges support from the National Projects of Scientific and Technological Support [grant number 2011BAB04B05], China Geological Survey [grant number 1212011085534]. F.Y.H. acknowledge support from National Natural Science Foundation of China [grant number 41902055], and China Postdoctoral Science Foundation [grant number 2018M640177]. M.N.D. acknowledges support from US National Science Foundation [grant number EAR 1725002] and the Romanian Executive Agency for Higher Education, Research, Development and Innovation Funding projects [grant numbers PN-III-P4-ID-PCE-2016-0127, PN-III-P4-ID-PCCF-2016-0014]. T.K acknowledges support from Natural Science Foundation of China [grant number 91755213].

## References

- Altherr, R., Holl, A., Hegner, E., Langer, C., Kreuzer, H., 2000. High-potassium, calc-alkaline I-type plutonism in the European Variscides: northern Vosges (France) and northern Schwarzwald (Germany). *Lithos* 50, 51–73.
- Ames, L., Gaozhi, Z., Baocheng, X., 1996. Geochronology and isotopic character of ultrahigh-pressure metamorphism with implications for collision of the Sino-Korean and Yangtze cratons, central China. *Tectonics* 15, 472–489.
- Andrić, N., Vogt, K., Matenco, L., Cvetković, V., Cloetingh, S., Gerya, T., 2018. Variability of orogenic magmatism during Mediterranean-style continental collisions: a numerical modelling approach. *Gondwana Res.* 56, 119–134.
- Angiboust, S., Yamato, P., Hertgen, S., Hyppolito, T., Bebout, G.E., Morales, L., 2017. Fluid pathways and high-P metasomatism in a subducted continental slice (Mt. Emilius klippe, W. Alps). *J. Metamorph. Geol.* 35, 471–492.
- Atherton, M.P., Ghani, A.A., 2002. Slab breakoff: a model for Caledonian, Late Granite syn-collisional magmatism in the orthotectonic (metamorphic) zone of Scotland and Donegal, Ireland. *Lithos* 62, 65–85.
- Ayers, J.C., Dunkle, S., Gao, S., Miller, C.F., 2002. Constraints on timing of peak and retrograde metamorphism in the Dabie Shan ultrahigh-pressure metamorphic belt, east-central China, using U-Th-Pb dating of zircon and monazite. *Chem. Geol.* 186, 315–331.
- Bachmann, O., Huber, C., 2016. Silicic magma reservoirs in the Earth's crust. *Am. Mineral.* 101, 2377–2404.
- Bader, T., Ratschbacher, L., Franz, L., Yang, Z., Hofmann, M., Linnemann, U., Yuan, H., 2013. The heart of China revisited. I. Proterozoic tectonics of the Qin mountains in the core of supercontinent Rodinia. *Tectonics* 32, 661–687.
- Bao, Z.W., Wang, C.Y., Zeng, L.J., Sun, W.D., Yao, J.M., 2015. Slab break-off model for the Triassic syn-collisional granites in the Qinling orogenic belt, Central China: zircon U-Pb age and Hf isotope constraints. *Int. Geol. Rev.* 57, 492–507.
- Bea, F., 2012. The sources of energy for crustal melting and the geochemistry of heat-producing elements. *Lithos* 153, 278–291.
- Bird, P., 1979. Continental delamination and the Colorado Plateau. *J. Geophys. Res. -Sol. Ea.* 84, 7561–7571.
- Boehnke, P., Watson, E.B., Trail, D., Harrison, T.M., Schmitt, A.K., 2013. Zircon saturation revisited. *Chem. Geol.* 351, 324–334.
- Boutelier, D., Cruden, A.R., 2018. Exhumation of (U) HP/LT rocks caused by diachronous slab breakoff. *J. Struct. Geol.* 117, 251–255.
- Browne, B.L., Eichelberger, J.C., Patino, L.C., Vogel, T.A., Dehn, J., Uto, K., Hoshizumi, H., 2006. Generation of porphyritic and equigranular mafic enclaves during magma recharge events at Unzen Volcano, Japan. *J. of Petrol.* 47, 301–328.
- Brun, J.-P., Faccenna, C., 2008. Exhumation of high-pressure rocks driven by slab rollback. *Earth Planet. Sci. Lett.* 272, 1–7.
- Cao, H., Li, S., Zhao, S., Yu, S., Li, X., Somerville, I.D., 2016. Detrital zircon geochronology of Neoproterozoic to early Paleozoic sedimentary rocks in the North Qinling Orogenic

- Belt: implications for the tectonic evolution of the Kuanping Ocean. *Precambrian Res.* 279, 1–16.
- Chai, R., Yang, J.H., Du, Y.S., Ding, D.S., 2016. Middle Triassic-Early Jurassic sedimentary record in the Zogui Basin and implication for the Qinling Indosian collisional orogenesis. *Geol. Sci. Tech. Info.* 35, 43–49 (in Chinese with English abstract).
- Chen, B., Jahn, B.M., Wei, C., 2002. Petrogenesis of Mesozoic granitoids in the Dabie UHP complex, Central China: trace element and Nd-Sr isotope evidence. *Lithos* 60, 67–88.
- Chen, R.X., Zheng, Y.F., Zhao, Z.F., Tang, J., Wu, F.Y., Liu, X.M., 2007. Zircon U-Pb age and Hf isotope evidence for contrasting origin of bimodal protoliths for ultrahigh-pressure metamorphic rocks from the Chinese Continental Scientific Drilling project. *J. Metamorph. Geol.* 25, 873–894.
- Chen, H., Hu, J.M., Wu, G.L., Gao, W., 2010. Study on the intracontinental deformation of the Mian-Lue suture belt, western Qinling. *Acta Petrol. Sin.* 26, 1277–1288 (in Chinese with English abstract).
- Chen, L.Q., Guo, R.T., Zhong, Y., 2011. Sedimentary facies constitutional features and their response to tectonic control of the Upper Triassic strata in the Jingmen-Dangyang basin. *Geol. China* 38, 1446–1453 (in Chinese with English abstract).
- Chen, L., Liu, X., Qu, W., Hu, J., 2014. U-Pb zircon ages and geochemistry of the Wuguan complex in the Qinling orogen, central China: implications for the late Paleozoic tectonic evolution between the Sino-Korean and Yangtze cratons. *Lithos* 192, 192–207.
- Chen, Y., Li, W., Yuan, X., Badal, J., Teng, J., 2015. Tearing of the Indian lithospheric slab beneath southern Tibet revealed by SKS-wave splitting measurements. *Earth Planet. Sci. Lett.* 413, 13–24.
- Chen, L., Liu, Z., Liu, X., Liu, S., 2019. Metamorphism and its relation of magmatism of the Foping Geiss Dome in the South Qinling Tectonic Belt. *Earth Sci.* 44, 4178–4185 (in Chinese with English abstract).
- Chen, L., Liu, X., Qu, W., Hu, J., 2020. Metamorphic evolution and  $^{40}\text{Ar}/^{39}\text{Ar}$  geochronology of the Wuguan complex, eastern Qinling area, China: implications for the late Paleozoic tectonic evolution of the Qinling orogen. *Lithos* 358–359, 105415.
- Cheng, H., King, R.L., Nakamura, E., Vervoort, J.D., Zhou, Z., 2008. Coupled Lu-Hf and Sm-Nd geochronology constrains garnet growth in ultra-high-pressure eclogites from the Dabie orogen. *J. Metamorph. Geol.* 26, 741–758.
- Cheng, H., DuFrane, S.A., Vervoort, J.D., Nakamura, E., Zheng, Y.F., Zhou, Z.Y., 2010. Protracted oceanic subduction prior to continental subduction: new Lu-Hf and Sm-Nd geochronology of oceanic-type high-pressure eclogite in the western Dabie orogen. *Am. Mineral.* 95, 1214–1223.
- Cheng, H., Zhang, C., Vervoort, J.D., Li, X.H., Li, Q.L., Zheng, S., Cao, D.D., 2011. Geochronology of the transition of eclogite to amphibolite facies metamorphism in the North Qinling orogen of central China. *Lithos* 125, 969–983.
- Chiu, H.-Y., Chung, S.-L., Zarinkoub, M.H., Mohammadi, S.S., Khatib, M.M., Iizuka, Y., 2013. Zircon U-Pb age constraints from Iran on the magmatic evolution related to Neotethyan subduction and Zagros orogeny. *Lithos* 162–163, 70–87.
- Chowdhury, P., Gerya, T., Chakraborty, S., 2017. Emergence of silicic continents as the lower crust peels off on a hot plate-tectonic Earth. *Nat. Geosci.* 10, 698–703.
- Chung, S.-L., Chu, M.-F., Zhang, Y., Xie, Y., Lo, C.-H., Lee, T.-Y., Lan, C.-Y., Li, X., Zhang, Q., Wang, Y., 2005. Tibetan tectonic evolution inferred from spatial and temporal variations in post-collisional magmatism. *Earth-Sci. Rev.* 68, 173–196.
- Collins, W.J., Richards, S.W., 2008. Geodynamic significance of S-type granites in circum-Pacific orogens. *Geology* 36, 559–562.
- Condamine, P., Médard, E., 2014. Experimental melting of phlogopite-bearing mantle at 1 GPa: implications for potassian magmatism. *Earth Planet. Sci. Lett.* 397, 80–92.
- Condamine, P., Médard, E., Devidal, J.-L., 2016. Experimental melting of phlogopite-peridotite in the garnet stability field. *Contrib. Mineral. Petro.* 171, 95.
- Dai, L., Li, S., Li, Z.-H., Somerville, I., Suo, Y., Liu, X., Gerya, T., Santosh, M., 2018. Dynamics of exhumation and deformation of HP-UHP orogens in double subduction-collision systems: numerical modeling and implications for the Western Dabie Orogen. *Earth-Sci. Rev.* 182, 68–84.
- Davidson, J., Turner, S., Handley, H., Macpherson, C., Dosseto, A., 2007. Amphibole “sponge” in arc crust? *Geology* 35, 787–790.
- Davies, J.H., von Blanckenburg, F., 1995. Slab breakoff: a model of lithosphere detachment and its test in the magmatism and deformation of collisional orogens. *Earth Planet. Sci. Lett.* 129, 85–102.
- Deng, Z., Liu, S., Zhang, W., Hu, F., Li, Q., 2016. Petrogenesis of the Guantoushan granitoid suite, central China: implications for Early Mesozoic geodynamic evolution of the Qinling Orogenic Belt. *Gondwana Res.* 30, 112–131.
- DePaolo, D.J., 1981. Trace element and isotopic effects of combined wallrock assimilation and fractional crystallization. *Earth Planet. Sci. Lett.* 53, 189–202.
- Dewey, J.F., 1977. Suture zone complexities: a review. *Tectonophysics* 40, 53–67.
- Dewey, J.F., Strachan, R.A., 2003. Changing Silurian-Devonian relative plate motion in the Caledonides: sinistral transposition to sinistral transtension. *J. Geol. Soc.* 160, 219–229.
- Diwu, C.R., Sun, Y., Liu, L., Zhang, C.L., Wang, H.L., 2010. The disintegration of Kuanping Group in the North Qinling orogenic belts and Neo-proterozoic N-MORB. *Acta Petrol. Sin.* 26, 2025–2038 (in Chinese with English abstract).
- Dong, Y.P., Santos, M., 2016. Tectonic architecture and multiple orogeny of the Qinling Orogenic Belt, Central China. *Gondwana Res.* 29, 1–40.
- Dong, Y.P., Zhou, M.F., Zhang, G.W., Zhou, D.W., Liu, L., Zhang, Q., 2008. The Grenvillian Songshugou ophiolite in the Qinling Mountains, Central China: implications for the tectonic evolution of the Qinling orogenic belt. *J. Asian Earth Sci.* 32, 325–335.
- Dong, Y.P., Zhang, G.W., Neubauer, F., Liu, X.M., Genser, J., Hauzenberger, C., 2011. Tectonic evolution of the Qinling orogen, China: review and synthesis. *J. Asian Earth Sci.* 41, 213–237.
- Dong, Y., Liu, X., Neubauer, F., Zhang, G., Tao, N., Zhang, Y., Zhang, X., Li, W., 2013. Timing of Paleozoic amalgamation between the North China and South China Blocks: evidence from detrital zircon U-Pb ages. *Tectonophysics* 586, 173–191.
- Dong, Y.P., Yang, Z., Liu, X.M., Zhang, X.N., He, D.F., Li, W., Zhang, F.F., Sun, S.S., Zhang, H.F., Zhang, G.W., 2014. Neoproterozoic amalgamation of the Northern Qinling terrain to the North China Craton: constraints from geochronology and geochemistry of the Kuanping ophiolite. *Precambrian Res.* 255, 77–95.
- Dong, Y., Sun, S., Yang, Z., Liu, X., Zhang, F., Li, W., Cheng, B., He, D., Zhang, G., 2017. Neoproterozoic subduction-accretionary tectonics of the South Qinling Belt, China. *Precambrian Res.* 293, 73–90.
- Dong, Y., Neubauer, F., Genser, J., Sun, S., Yang, Z., Zhang, F., Cheng, B., Liu, X., Zhang, G., 2018. Timing of orogenic exhumation processes of the Qinling Orogen: evidence from  $^{40}\text{Ar}/^{39}\text{Ar}$  dating. *Tectonics* 37, 4037–4067.
- Ducea, M.N., Chapman, A.D., 2018. Sub-magmatic arc underplating by trench and forearc materials in shallow subduction systems: a geologic perspective and implications. *Earth-Sci. Rev.* 185, 763–779.
- Ducea, M.N., Saleeby, J.B., 1996. Buoyancy sources for a large, unrooted mountain range, the Sierra Nevada, California: evidence from xenolith thermobarometry. *J. Geophys. Res.-Sol. Ea.* 101, 8229–8244.
- Ducea, M.N., Seclaman, A.C., Murray, K.E., Jianu, D., Schoenbohm, L.M., 2013. Mantle-drip magmatism beneath the Altiplano-Puna plateau, central Andes. *Geology* 41, 915–918.
- Ducea, M.N., Saleeby, J.B., Bergantz, G., 2015. The architecture, chemistry, and evolution of continental magmatic arcs. *Annu. Rev. Earth Planet. Sci.* 43, 299–331.
- Duretz, T., Gerya, T.V., 2013. Slab detachment during continental collision: influence of crustal rheology and interaction with lithospheric delamination. *Tectonophysics* 602, 124–140.
- Duretz, T., Gerya, T.V., May, D.A., 2011. Numerical modelling of spontaneous slab breakoff and subsequent topographic response. *Tectonophysics* 502, 244–256.
- Eide, E.A., Liou, J.G., 2000. High-pressure blueschists and eclogites in Hong'an: a framework for addressing the evolution of high- and ultrahigh-pressure rocks in central China. *Lithos* 52, 1–22.
- England, P.C., Thompson, A., 1986. Some thermal and tectonic models for crustal melting in continental collision zones. *Geol. Soc. Spec. Publ.* 19, 83–94.
- Feng, P., Wang, L., Brown, M., Wang, S.J., Li, X.W., 2020. Separating multiple episodes of partial melting in polygenetic crust: an example from the Haiyangsu complex, northern Sulu belt, eastern China. *Geol. Soc. Am. Bull.* 132, 1235–1256.
- Fowler, M.B., Kocks, H., Derbyshire, D.P.F., Greenwood, P.B., 2008. Petrogenesis of high Ba-Sr plutons from the Northern Highlands Terrane of the British Caledonian Province. *Lithos* 105, 129–148.
- Freeburn, R., Bouilhol, P., Maunder, B., Magni, V., van Hunen, J., 2017. Numerical models of the magmatic processes induced by slab breakoff. *Earth Planet. Sci. Lett.* 478, 203–213.
- Fu, D., Kusky, T.M., Wilde, S.A., Polat, A., Huang, B., Zhou, Z.P., 2018. Early Paleozoic collisional-related magmatism in the eastern North Qilian orogen, northeastern Tibet: a linkage between accretionary and collisional orogenesis. *Geol. Soc. Am. Bull.* 131, 1031–1056.
- Furman, T., Graham, D., 1999. Erosion of lithospheric mantle beneath the East African Rift system: geochemical evidence from the Kivu volcanic province. *Lithos* 48, 237–262.
- Gao, S., Yang, J., Zhou, L., Li, M., Hu, Z.C., Guo, J.L., Yuan, H.L., Gong, H.J., Xiao, G.Q., Wei, J.Q., 2011a. Age and growth of the Archean Kongling terrain, South China, with emphasis on 3.3 Ga granitoid gneisses. *Am. J. Sci.* 311, 153–182.
- Gao, X.Y., Zheng, Y.F., Chen, Y.X., 2011b. U-Pb ages and trace elements in metamorphic zircon and titanite from UHP eclogite in the Dabie orogen: constraints on P-T-t path. *J. Metamorph. Geol.* 29, 721–740.
- Gargani, E., Radloff, G., Malusà, M.G., 2018. Slab breakoff: a critical appraisal of a geological theory as applied in space and time. *Earth-Sci. Rev.* 177, 303–319.
- Godin, L., Grujic, D., Law, R.D., Searle, M.P., 2006. Channel flow, ductile extrusion and exhumation in continental collision zones: an introduction. *Geol. Soc. Spec. Publ.* 268, 1–23.
- Göğüş, O.H., Ueda, K., 2018. Peeling back the lithosphere: controlling parameters, surface expressions and the future directions in delamination modeling. *J. Geodyn.* 117, 21–40.
- Göğüş, O.H., Pysklywec, R.N., Şengör, A.M.C., Gün, E., 2017. Drip tectonics and the enigmatic uplift of the Central Anatolian Plateau. *Nat. Commun.* 8, 1538.
- Guo, C.L., 2010. Petrogenesis and Formation Mechanism of Xizhuanghe Granitic Pluton in the Erlangping Area of Eastern Qinling Orogenic Belt. Northwest Univ., Xi'an, pp. 1–60 (in Chinese with English abstract).
- Guo, Z., Chen, Y.J., 2016. Crustal structure of the eastern Qinling orogenic belt and implication for reactivation since the Cretaceous. *Tectonophysics* 683, 1–11.
- Guo, X., Yan, Z., Wang, Z., Hou, K., Fu, C., Li, J., 2012. Middle Triassic arc magmatism along the northeastern margin of the Tibet: U-Pb and Lu-Hf zircon characterization of the Gangcha complex in the West Qinling terrane, central China. *J. Geol. Soc.* 169, 327–336.
- Guo, J.L., Gao, S., Wu, Y.-B., Li, M., Chen, K., Hu, Z.-C., Liang, Z.-W., Liu, Y.-S., Zhou, L., Zong, K.-Q., Zhang, W., Chen, H.-H., 2014. 3.45Ga granitic gneisses from the Yangtze Craton, South China: implications for Early Archean crustal growth. *Precambrian Res.* 242, 82–95.
- Guo, J.L., Wu, Y.B., Gao, S., Jin, Z.M., Zong, K.Q., Hu, Z.C., Chen, K., Chen, H.H., Liu, Y.S., 2015. Episodic Paleoproterozoic-Paleoproterozoic (3.3–2.0 Ga) granitoid magmatism in Yangtze craton, South China: implications for late Archean tectonics. *Precambrian Res.* 270, 246–266.
- Gürer, D., van Hinsbergen, D.J.J., 2019. Diachronous demise of the Neotethys Ocean as a driver for non-cylindrical orogenesis in Anatolia. *Tectonophysics* 760, 95–106.
- Hacker, B.R., Ratschbacher, L., Liou, J.G., 2004. Subduction, collision and exhumation in the ultrahigh-pressure Qinling-Dabie orogen. *Geol. Soc. Spec. Publ.* 226, 157–175.
- Hacker, B.R., Wallis, S.R., Ratschbacher, L., Grove, M., Gehrels, G., 2006. High-temperature geochronology constraints on the tectonic history and architecture of the ultrahigh-pressure Dabie-Sulu Orogen. *Tectonics* 25, TC5006.

- Harris, N.B., Pearce, J.A., Tindle, A.G., 1986. Geochemical characteristics of collision-zone magmatism. *Geol. Soc. Spec. Publ.* 19, 67–81.
- Hildebrand, R.S., 2013. Mesozoic assembly of the North American cordillera. *Geol. Soc. Am. Spec. Pap.* 495, 169.
- Horton, B.K., 2018. Tectonic regimes of the central and southern Andes: Responses to variations in plate coupling during subduction. *Tectonics* 37, 402–429.
- Hu, J., Chen, H., Qu, H., Wu, G., Yang, J., Zhang, Z., 2012. Mesozoic deformations of the Dabashan in the southern Qinling orogen, central China. *J. Asian Earth Sci.* 47, 171–184.
- Hu, S., Raza, A., Min, K., Kohn, B.P., Reiners, P.W., Ketcham, R.A., Wang, J., Gleadow, A.J.W., 2006. Late Mesozoic and Cenozoic thermotectonic evolution along a transect from the north China craton through the Qinling orogen into the Yangtze craton, central China. *Tectonics* 25, TC6009.
- Hu, J., Liu, X., Chen, L., Qu, W., Li, H., Geng, J., 2013. A ~2.5 Ga magmatic event at the northern margin of the Yangtze craton: evidence from U-Pb dating and Hf isotope analysis of zircons from the Douling Complex in the South Qinling orogen. *Chinese Sci. Bull.* 58, 3564–3579.
- Hu, F., Liu, S., Zhang, W., Deng, Z., Chen, X., 2016a. A westward propagating slab tear model for Late Triassic Qinling Orogenic Belt geodynamic evolution: insights from the petrogenesis of the Caoping and Shahewan intrusions, central China. *Lithos* 262, 486–506.
- Hu, F., Liu, S., Santosh, M., Deng, Z., Wang, W., Zhang, W., Yan, M., 2016b. Chronology and tectonic implications of Neoproterozoic blocks in the South Qinling Orogenic Belt, Central China. *Gondwana Res.* 30, 24–47.
- Hu, F., Ducea, M.N., Liu, S., Chapman, J.B., 2017a. Quantifying crustal thickness in continental collisional belts: global perspective and a geologic application. *Sci. Rep.* 7, 7058.
- Hu, F., Liu, S., Ducea, M.N., Zhang, W., Deng, Z., 2017b. The geochemical evolution of the granitoid rocks in the South Qinling Belt: insights from the Dongjiangkou and Zhashui intrusions, central China. *Lithos* 278–281, 195–214.
- Hu, F., Liu, S., Ducea, M.N., Zhang, W., Chapman, J.B., Fu, J., Wang, M., 2018. Interaction among magmas from various sources and crustal melting processes during continental collision: insights from the Huayang Intrusive Complex of the South Qinling Belt, China. *J. Petrol.* 59, 735–770.
- Huang, F., Li, S., Dong, F., He, Y., Chen, F., 2008. High-Mg adakitic rocks in the Dabie orogen, central China: implications for foudering mechanism of lower continental crust. *Chem. Geol.* 255, 1–13.
- Jian, X., Weislogel, A., Pullen, A., 2019. Triassic sedimentary filling and closure of the Eastern Paleo-Tethys Ocean: new insights from detrital zircon geochronology of Songpan-Ganzi, Yidun, and West Qinling Flysch in Eastern Tibet. *Tectonics* 38, 767–787.
- Jiang, Y.-H., Jin, G.-D., Liao, S.-Y., Zhou, Q., Zhao, P., 2010. Geochemical and Sr-Nd-Hf isotopic constraints on the origin of Late Triassic granitoids from the Qinling orogen, central China: implications for a continental arc to continent-continent collision. *Lithos* 117, 183–197.
- Jiang, Y.-H., Jin, G.-D., Liao, S.-Y., Zhou, Q., Zhao, P., 2012. Petrogenesis and tectonic implications of ultrapotassic microgranitoid enclaves in Late Triassic arc granitoids, Qinling orogen, central China. *Int. Geol. Rev.* 54, 208–226.
- Kaban, M.K., Petrunin, A.G., El Khrepy, S., Al-Arfi, N., 2018. Diverse continental subduction scenarios along the Arabia-Eurasia collision zone. *Geophys. Res. Lett.* 45, 6898–6906.
- Katsube, A., Hayasaka, Y., Santosh, M., Li, S., Terada, K., 2009. SHRIMP zircon U-Pb ages of eclogite and orthogneiss from Sulu ultrahigh-pressure zone in Yangkou area, eastern China. *Gondwana Res.* 15, 168–177.
- Kay, R.W., Kay, S.M., 1993. Delamination and delamination magmatism. *Tectonophysics* 219, 177–189.
- Kroner, U., Romer, R.L., 2013. Two plates – many subduction zones: the Variscan orogeny reconsidered. *Gondwana Res.* 24, 298–329.
- Kusky, T.M., Bradley, D.C., Donley, D.T., Rowley, D., Haueussler, P., 2003. Controls on intrusion of near-trench magmas of the Sanak-Baranof belt, Alaska, during Paleogene ridge subduction, and consequences for forearc evolution. In: Sisson, V.B., Roeske, S., Pavlis, T.L. (Eds.), *Geology of a Transpressional Orogen Developed During a Ridge - Trench Interaction Along the North Pacific Margin*. *Geol. Soc. Am. Spec. Pap.* vol. 371, pp. 269–292.
- Kusky, T.M., Windley, B.F., Wang, L., Wang, Z.S., Li, X.Y., Zhu, P.M., 2014. Flat slab subduction, trench suction, and craton destruction: comparison of the North China, Wyoming, and Brazilian cratons. *Tectonophysics* 630, 208–221.
- Kusky, T.M., Windley, B.F., Polat, A., 2018. Geological evidence for the operation of plate tectonics throughout the Archean: records from Archean paleo-plate boundaries. *J. Earth Sci.* 29, 1291–1303.
- Lai, X.L., Yin, H.F., Yang, F.Q., 1995. Reconstruction of the Qinling Triassic Paleo-Ocean. *Earth Sci. - J. China Univ. Geosci.* 20, 648–656 (in Chinese with English abstract).
- Lee, C.T.A., Cheng, X., Horodyskyj, U., 2006. The development and refinement of continental arcs by primary basaltic magmatism, garnet pyroxenite accumulation, basaltic recharge and delamination: insights from the Sierra Nevada, California. *Contrib. Mineral. Petro.* 151, 222–242.
- Lei, M., 2010. Petrogenesis of Granites and Their Relation to Tectonic Evolution of Orogen in the East Part of Qinling Orogenic Belt. *Chinese Acad. Geol. Sci.*, Beijing, pp. 1–162.
- Li, J.Y., Wang, Z.Q., Zhao, M., 1999.  $^{40}\text{Ar}/^{39}\text{Ar}$  thermochronological constraints on the timing of collisional orogeny in the Mian-Lue collision belt, southern Qinling Mountains. *Acta Geol. Sin.* 73, 208–215 (in Chinese with English abstract).
- Li, S.G., Jagoutz, E., Chen, Y.Z., Li, Q.L., 2000. Sm-Nd and Rb-Sr isotopic chronology and cooling history of ultrahigh pressure metamorphic rocks and their country rocks at Shuanghe in the Dabie Mountains, Central China. *Geochim. Cosmochim. Acta* 64, 1077–1093.
- Li, X.-H., Li, Z.-X., Ge, W., Zhou, H., Li, W., Liu, Y., Wingate, M.T.D., 2003. Neoproterozoic granitoids in South China: crustal melting above a mantle plume at ca. 825 Ma? *Pre-cambrian Res.* 122, 45–83.
- Li, S., Kusky, T.M., Wang, L., Zhang, G., Lai, S., Liu, X., Dong, S., Zhao, G., 2007. Collision leading to multiple-stage large-scale extrusion in the Qinling orogen: insights from the Mianlue suture. *Gondwana Res.* 12, 121–143.
- Li, X.B., Wang, C.S., Liu, A., 2008. Sedimentary response to the Indosinian movement—a case study of the Mid-Upper Triassic in the Zigui basin, Hubei. *Geol. China* 35, 984–991 (in Chinese with English abstract).
- Li, X.-W., Mo, X.-X., Yu, X.-H., Ding, Y., Huang, X.-F., Wei, P., He, W.-Y., 2013. Petrology and geochemistry of the early Mesozoic pyroxene andesites in the Maixiu Area, West Qinling, China: products of subduction or syn-collision? *Lithos* 172–173, 158–174.
- Li, L., Meng, Q., Pullen, A., Garzione, C.N., Wu, G., Wang, Y., Ma, S., Duan, L., 2014. Late Permian–early Middle Triassic back-arc basin development in West Qinling, China. *J. Asian Earth Sci.* 87, 116–129.
- Li, N., Chen, Y.J., Santosh, M., Pirajno, F., 2015a. Compositional polarity of Triassic granitoids in the Qinling Orogen, China: implication for termination of the northermost paleo-Tethys. *Gondwana Res.* 27, 244–257.
- Li, Y., Xu, Z.Q., Pei, X.Z., Zhang, J., Zhao, J.N., Zhang, L., Wu, Y., 2015b. The probability of the Mianlue suture zone, South Qinling extends to Dabie-Sulu UHP belt, East Qinling: constrain from the activity time of Ningshan shear zone. *Acta Petrol. Sin.* 31, 3595–3608 (in Chinese with English abstract).
- Li, X., Mo, X., Huang, X., Dong, G., Yu, X., Luo, M., Liu, Y., 2015c. U-Pb zircon geochronology, geochemical and Sr-Nd-Hf isotopic compositions of the Early Indosinian Tongren Pluton in West Qinling: petrogenesis and geodynamic implications. *J. Asian Earth Sci.* 97, 38–50.
- Li, S.Z., Yang, C., Zhao, S.J., Li, X.Y., Guo, L.L., Yu, S., Liu, X., Suo, Y.H., Lan, H.Y., 2016a. Global Early Paleozoic orogens (I): collision-type orogeny. *J. Jilin Univ. (Eng. Sci. Ed.)* 46, 945–967 (in Chinese with English abstract).
- Li, H., Gao, R., Wang, H., Li, W., Xiong, X., 2016b. Using large dynamite shots to image the structure of the Moho from deep seismic reflection experiment between the Sichuan basin and Qinling orogen. *Earthquake Sci.* 29, 321–326.
- Li, Y., Liang, W., Zhang, G., Jiang, D., Wang, J., Li, S., 2017. Tectonic setting of the Late Triassic magmatism in the Qinling Orogen: new constraints from the interplay between granite emplacement and shear zone deformation in the Shagou area. *Geol. J.* 52, 250–271.
- Li, S., Zhao, S., Liu, X., Cao, H., Yu, S., Li, X., Somerville, I., Yu, S., Suo, Y., 2018a. Closure of the Proto-Tethys Ocean and Early Paleozoic amalgamation of microcontinental blocks in East Asia. *Earth-Sci. Rev.* 186, 37–75.
- Li, N., Chen, Y.-J., Santosh, M., Pirajno, F., 2018b. Late Mesozoic granitoids in the Qinling Orogen, Central China, and tectonic significance. *Earth-Sci. Rev.* 182, 141–173.
- Li, J., Li, Z., Liu, S., Ran, B., Ye, Y., Deng, B., Sun, D., 2018c. Kinematics of the Chengkou Fault in the South Qinling Orogen, Central China. *J. Struct. Geol.* 114, 64–75.
- Liang, W., 2009. The Characteristics of Intracontinental Tectonics and Process in the Conjecture Area of the East and West Qinling Orogen of Qinling Mountains. *Northwest Univ. Xi'an*, pp. 1–186 (in Chinese with English abstract).
- Liang, S., Liu, L., Zhang, C.L., Yang, Y.C., Yang, W.Q., Kang, L., Cao, Y.T., 2013. Metamorphism and zircon U-Pb age of high-pressure mafic granulites in the Mian-Lue suture zone, South Qinling orogen. *Acta Petrol. Sin.* 29, 1657–1674 (in Chinese with English abstract).
- Liang, W., Zhang, G., Bai, Y., Jin, C., Nantasin, P., 2015. New insights into the emplacement mechanism of the Late Triassic granite plutons in the Qinling orogen: a structural study of the Mishulung pluton. *Geol. Soc. Am. Bull.* 127, 1583–1603.
- Liao, J., Gerya, T., 2016. 3D numerical modeling on oblique continental collision. *EGU Gen. Ass'y Conf. Abs.* 18.
- Lin, Y.C., Chung, S.L., Bingöl, A.F., Yang, L., Okrostsvardiz, A., Pang, K.N., Lee, H.Y., Lin, T.H., 2020. Diachronous initiation of post-collisional magmatism in the Arabia-Eurasia collision zone. *Lithos* 356, 105394.
- Ling, W.L., 1996. Isotope geochronology and crustal growth of Proterozoic basement along the Northern margin of Yangtze Craton: I. Houhe Group and Xixiang Group. *Earth Sci.* 21, 491–494 (in Chinese with English abstract).
- Ling, W.L., Reng, B.F., Duan, R.C., Liu, X.M., Mao, X.W., Peng, L.H., Liu, Z.X., Cheng, J.P., Yang, H.M., 2008. Timing of the Wudangshan, Yaolinge volcanic sequences and mafic sills in South Qinling: U-Pb zircon geochronology and tectonic implication. *Chinese Sci. Bull.* 53, 2192–2199.
- Liu, R.Y., 2011. The Geochronology, Geochemical Characteristics and Tectonic Implication of the Xiaomaoling Composite Intrusives in Zhashui, Shaanxi. *Chinese Acad. Geol. Sci., Beijing*, pp. 1–68 (in Chinese with English abstract).
- Liu, F.L., Liou, J.G., 2011. Zircon as the best mineral for P-T-time history of UHP metamorphism: a review on mineral inclusions and U-Pb SHRIMP ages of zircons from the Dabie-Sulu UHP rocks. *J. Asian Earth Sci.* 40, 1–39.
- Liu, S., Zhang, G., 2013. Mesozoic basin development and its indication of collisional orogeny in the Dabie orogen. *Chin. Sci. Bull.* 58, 827–852.
- Liu, F.L., Xu, Z.Q., Xue, H.M., 2004a. Tracing the protolith, UHP metamorphism, and exhumation ages of orthogneiss from the SW Sulu terrane (eastern China): SHRIMP U-Pb dating of mineral inclusion-bearing zircons. *Lithos* 78, 411–429.
- Liu, X.C., Jahn, B.M., Liu, D.Y., Dong, S.W., Li, S.Z., 2004b. SHRIMP U-Pb zircon dating of a metagabbro and eclogites from western Dabieshan (Hong'an Block), China, and its tectonic implications. *Tectonophysics* 394, 171–192.
- Liu, S., Steel, R., Zhang, G., 2005. Mesozoic sedimentary basin development and tectonic implication, northern Yangtze Block, eastern China: record of continent-continent collision. *J. Asian Earth Sci.* 25, 9–27.
- Liu, F.L., Gerdes, A., Liou, J.G., Xue, H.M., Liang, F.H., 2006a. SHRIMP U-Pb zircon dating from Sulu-Dabie dolomitic marble, eastern China: constraints on prograde, ultrahigh-pressure and retrograde metamorphic ages. *J. Metamorph. Geol.* 24, 569–589.
- Liu, D., Jian, P., Kröner, A., Xu, S., 2006b. Dating of prograde metamorphic events deciphered from episodic zircon growth in rocks of the Dabie-Sulu UHP complex, China. *Earth Planet. Sci. Lett.* 250, 650–666.

- Liu, F.L., Gerdes, A., Zeng, L.S., Xue, H.M., 2008a. SHRIMP U-Pb dating, trace elements and the Lu-Hf isotope system of coesite-bearing zircon from amphibolite in the SW Sulu UHP terrane, eastern China. *Geochim. Cosmochim. Acta* 72, 2973–3000.
- Liu, X., Jahn, B.M., Dong, S., Lou, Y., Cui, J., 2008b. High-pressure metamorphic rocks from Tongbaishan, central China: U-Pb and  $^{40}\text{Ar}/^{39}\text{Ar}$  age constraints on the provenance of protoliths and timing of metamorphism. *Lithos* 105, 301–318.
- Liu, J., Sun, Y., Tong, L., Sun, W., 2009. Emplacement age of the Songshugou ultramafic massif in the Qinling orogenic belt, and geologic implications. *Int. Geol. Rev.* 51, 58–76.
- Liu, X.C., Jahn, B.M., Cui, J.J., Li, S.Z., Wu, Y.B., Li, X.H., 2010. Triassic retrograded eclogites and Cretaceous gneissic granites in the Tongbai Complex, central China: implications for the architecture of the HP/UHP Tongbai-Dabie-Sulu collision zone. *Lithos* 119, 211–237.
- Liu, S.W., Li, Q.G., Tian, W., Wang, Z.Q., Yang, P.T., Wang, W., Bai, X., Guo, R.R., 2011a. Petrogenesis of Indosinian granitoids in middle-segment of South Qinling Tectonic Belt: constraints from Sr-Nd isotopic systematics. *Acta Geol. Sin.* 85, 610–628.
- Liu, X.C., Wu, Y.B., Gao, S., Peng, M., Wang, J., Wang, H., Gong, H.J., Yuan, H.L., 2012. Triassic high-pressure metamorphism in the Huwan shear zone: tracking the initial subduction of continental crust in the whole Dabie orogen. *Lithos* 136–139, 60–72.
- Liu, C.H., Wu, C.L., Gao, Y.H., Lei, M., Qin, H.P., Li, M.Z., 2014. Zircon LA-ICP-MS U-Pb dating and Lu-Hf isotopic system of Dongjiangkou, Zhashui, Liuyuantang granitoid intrusions, South Qinling belt, central China. *Acta Petrol. Sin.* 30, 2402–2420 (in Chinese with English abstract).
- Liu, S., Qian, T., Li, W., Dou, G., Wu, P., 2015a. Oblique closure of the northeastern Paleo-Tethys in central China. *Tectonics* 34, 413–434.
- Liu, X., Li, S., Jahn, B.M., 2015b. Tectonic evolution of the Tongbai-Hong'an orogen in central China: from oceanic subduction/accretion to continent-continent collision. *Science China Earth Sciences* 58, 1477–1496.
- Liu, L., Liao, X., Wang, Y., Wang, C., Santosh, M., Yang, M., Zhang, C., Chen, D., 2016. Early Paleozoic tectonic evolution of the North Qinling Orogenic Belt in Central China: insights on continental deep subduction and multiphase exhumation. *Earth-Sci. Rev.* 159, 58–81.
- Liu, Z., Chen, L., Qu, W., Hu, J., Liu, X., 2019. Early Mesozoic metamorphism, anatexis and deformation of foping area in South Qinling Belt: constrains from U-Pb zircon dating. *Acta Geosci. Sin.* 40, 545–562.
- Lü, X.Q., Wang, X.X., Ke, C.H., Li, J.B., Yang, Y., Meng, X.Y., Nie, Z.R., Zhang, P.C., 2014. LA-ICP-MS zircon U-Pb dating of Taibai pluton in North Qinling Mountains and its geological significance. *Mineral Dep.* 33, 37–52 (in Chinese with English abstract).
- Lu, Y.H., Zhao, Z.F., Zheng, Y.F., 2016. Geochemical constraints on the source nature and melting conditions of Triassic granites from South Qinling in central China. *Lithos* 264, 141–157.
- Lustrino, M., 2005. How the delamination and detachment of lower crust can influence basaltic magmatism. *Earth-Sci. Rev.* 72, 21–38.
- Magni, V., Faccenna, C., van Hunen, J., Funiciello, F., 2013. Delamination vs. break-off: the fate of continental collision. *Geophys. Res. Lett.* 40, 285–289.
- Malatesta, C., Gerya, T., Crispini, L., Federico, L., Capponi, G., 2013. Oblique subduction modelling indicates along-trench tectonic transport of sediments. *Nat. Commun.* 4, 2456.
- Maniar, P.D., Piccoli, P.M., 1989. Tectonic discrimination of granitoids. *Geol. Soc. Am. Bull.* 101, 635–643.
- Martin, H., Smithies, R.H., Rapp, R., Moyen, J.F., Champion, D., 2005. An overview of adakite, tonalite-trondhjemite-granodiorite (TTG), and sanukitoid: relationships and some implications for crustal evolution. *Lithos* 79, 1–24.
- Mattauer, M., Matte, P., Malavieille, J., Tapponnier, P., Maluski, H., Qin, X.Z., Lun, L.Y., Qin, T.Y., 1985. Tectonics of the Qinling belt: build-up and evolution of eastern Asia. *Nature* 317, 496–500.
- McCay, G.A., Robertson, A.H.F., 2012. Late Eocene–Neogene sedimentary geology of the Girne (Kyrenia) Range, northern Cyprus: a case history of sedimentation related to progressive and diachronous continental collision. *Sediment. Geol.* 265–266, 30–55.
- McDonough, W.F., Sun, S.S., 1995. The composition of the Earth. *Chem. Geol.* 120, 223–253.
- Menant, A., Sternai, P., Jolivet, L., Guillou-Frottier, L., Gerya, T., 2016. 3D numerical modeling of mantle flow, crustal dynamics and magma genesis associated with slab rollback and tearing: the eastern Mediterranean case. *Earth Planet. Sci. Lett.* 442, 93–107.
- Meng, Q.R., Zhang, G.W., 1999. Timing of collision of the North and South China blocks: controversy and reconciliation. *Geology* 27, 123–126.
- Meng, Q.-R., Wang, E., Hu, J.-M., 2005. Mesozoic sedimentary evolution of the northwest Sichuan basin: implication for continued clockwise rotation of the South China block. *Geol. Soc. Am. Bull.* 117, 396–410.
- Meng, Q.-R., Wu, G.-L., Fan, L.-G., Wei, H.-H., 2019. Tectonic evolution of early Mesozoic sedimentary basins in the North China block. *Earth-Sci. Rev.* 190, 416–438.
- Middlemost, E.A.K., 1994. Naming materials in the magma/igneous rock system. *Earth-Sci. Rev.* 37, 215–224.
- Miles, A.J., Woodcock, N.H., Hawkesworth, C.J., 2016. Tectonic controls on post-subduction granite genesis and emplacement: the late Caledonian suite of Britain and Ireland. *Gondwana Res.* 39, 250–260.
- Miller, C.F., McDowell, S.M., Mapes, R.W., 2003. Hot and cold granites? Implications of zircon saturation temperatures and preservation of inheritance. *Geology* 31, 529–532.
- Moyen, J.-F., 2009. High Sr/Y and La/Yb ratios: the meaning of the “adakitic signature”. *Lithos* 112, 556–574.
- Nábělek, P.I., Whittington, A.G., Hofmeister, A.M., 2010. Strain heating as a mechanism for partial melting and ultrahigh temperature metamorphism in convergent orogens: implications of temperature-dependent thermal diffusivity and rheology. *J. Geophys. Res. -Sol. Ea.* 115, B12417.
- Nie, H., Yang, J., Zhou, G., Liu, C., Zheng, J., Zhang, W.-X., Zhao, Y.-J., Wang, H., Wu, Y., 2017. Geochemical and Re-Os isotope constraints on the origin and age of the Songshugou peridotite massif in the Qinling orogen, central China. *Lithos* 292–293, 307–319.
- Oh, C.W., Kusky, T.M., 2007. The Late-Permian to Triassic Hongseong-Odesan Collision belt in South Korea and its tectonic correlation with Korea, China and Japan. *Int. Geol. Rev.* 49, 636–657.
- Otamendi, J.E., Patiño Douce, A.E., 2001. Partial melting of aluminous metagreywackes in the Northern Sierra de Comechingones, Central Argentina. *J. Petrol.* 42, 1751–1772.
- Patiño Douce, A.E., 1999. What do experiments tell us about the relative contributions of crust and mantle to the origin of granitic magmas? *Geol. Soc. Spec. Publ.* 168, 55–75.
- Pecceirillo, A., Taylor, S.R., 1976. Geochemistry of Eocene calc-alkaline volcanic rocks in the Kastamonu area, Northern Turkey. *Contrib. Mineral. Petrol.* 58, 63–81.
- Pirouz, M., Simpson, G., Chiaradia, M., 2015. Constraint on foreland basin migration in the Zagros mountain belt using Sr isotope stratigraphy. *Basin Res.* 27, 714–728.
- Pullen, A., Kapp, P., Gehrels, G.E., Vervoort, J.D., Ding, L., 2008. Triassic continental subduction in central Tibet and Mediterranean-style closure of the Paleo-Tethys Ocean. *Geology* 36, 351–354.
- Qian, Q., Hermann, J., 2013. Partial melting of lower crust at 10–15 kbar: constraints on adakite and TTG formation. *Contrib. Mineral. Petrol.* 165, 1195–1224.
- Qin, Z.W., 2016. Early Paleozoic Magmatism in the North Qinling Orogenic Belt and Its Implications for Continental Crust Evolution. *China Univ. Geosci., Wuhan*, pp. 1–137 (in Chinese with English abstract).
- Qin, J.-F., Lai, S.-C., Grapes, R., Diwu, C.-r., Ju, Y.-J., Li, Y.-F., 2010a. Origin of Late Triassic high-Mg adakitic granitoids rocks from the Dongiangkou area, Qinling orogen, central China: implications for subduction of continental crust. *Lithos* 120, 347–367.
- Qin, J.-F., Lai, S.-C., Diwu, C.-r., Ju, Y.-J., Li, Y.-F., 2010b. Magma mixing origin for the post-collisional adakitic monzogranite of the Triassic Yangba pluton, Northwestern margin of the South China block: geochemistry, Sr-Nd isotopic, zircon U-Pb dating and Hf isotopic evidences. *Contrib. Mineral. Petrol.* 159, 389–409.
- Qin, J.-F., Lai, S.-C., Li, Y.-F., 2013. Multi-stage granitic magmatism during exhumation of subducted continental lithosphere: evidence from the Wulong pluton, South Qinling. *Gondwana Res.* 24, 1108–1126.
- Qin, Z.-w., Wu, Y.-B., Wang, H., Gao, S., Zhu, L.-Q., Zhou, L., Yang, S.-H., 2014. Geochronology, geochemistry, and isotope compositions of Piaochi S-type granitic intrusion in the Qinling orogen, central China: petrogenesis and tectonic significance. *Lithos* 202–203, 347–362.
- Qin, Z., Wu, Y., Siebel, W., Gao, S., Wang, H., Abdalsamed, M.I.M., Zhang, W., Yang, S., 2015. Genesis of adakitic granitoids by partial melting of thickened lower crust and its implications for early crustal growth: a case study from the Huichizi pluton, Qinling orogen, central China. *Lithos* 238, 1–12.
- Rapp, R.P., Watson, E.B., 1995. Dehydration melting of metabasalt at 8–32 kbar: implications for continental growth and crust-mantle recycling. *J. Petrol.* 36, 891–931.
- Rapp, R.P., Shimizu, N., Norman, M.D., Applegate, G.S., 1999. Reaction between slab-derived melts and peridotite in the mantle wedge: experimental constraints at 3.8 GPa. *Chem. Geol.* 160, 335–356.
- Ratschbacher, L., Hacker, B.R., Calvert, A., Webb, L.E., Grimmer, J.C., McWilliams, M.O., Ireland, T., Dong, S., Hu, J., 2003. Tectonics of the Qinling (Central China): tectonostratigraphy, geochronology, and deformation history. *Tectonophysics* 366, 1–53.
- Roger, F., Jolivet, M., Malavieille, J., 2010. The tectonic evolution of the Songpan-Garzé (North Tibet) and adjacent areas from Proterozoic to Present: a synthesis. *J. Asian Earth Sci.* 39, 254–269.
- Rollinson, H., 1993. *Using Geochemical Data: Evaluation, Presentation, Interpretation*. Longman Sci. Tech., London, pp. 1–384.
- Schildgen, T.F., Yıldırım, C., Cosentino, D., Strecker, M.R., 2014. Linking slab break-off, Hellenic trench retreat, and uplift of the Central and Eastern Anatolian plateaus. *Earth-Sci. Rev.* 128, 147–168.
- Schmidt, A., Weyer, S., Mezger, K., Scherer, E.E., Xiao, Y.L., Hoefs, J., Brey, G.P., 2008. Rapid eclogitisation of the Dabie-Sulu UHP terrane: constraints from Lu-Hf garnet geochronology. *Earth Planet. Sci. Lett.* 273, 203–213.
- Schmidt, A., Mezger, K., O'Brien, P.J., 2011. The time of eclogite formation in the ultrahigh pressure rocks of the Sulu terrane constraints from Lu-Hf garnet geochronology. *Lithos* 125, 743–756.
- Seghedi, I., Downes, H., 2011. Geochemistry and tectonic development of Cenozoic magmatism in the Carpathian-Pannonian region. *Gondwana Res.* 20, 655–672.
- Shad Manaman, N., Shomali, H., Koyi, H., 2011. New constraints on upper-mantle S-velocity structure and crustal thickness of the Iranian plateau using partitioned waveform inversion. *Geophys. J. Inter.* 184, 247–267.
- Shen, J., Zhang, Z.Q., Liu, D.Y., 1997. Sm-Nd, Rb-Sr, Ar/Pb age of the Douling metamorphic complex from eastern Qinling Orogenic Belt. *Acta Geosci. Sin.* 18, 248–254 (in Chinese with English abstract).
- Shi, Y., Yu, J.-H., Xu, X.S., Tang, H.F., Qiu, J.S., Chen, L.H., 2011. U-Pb ages and Hf isotope compositions of zircons of Taihua Group in Xiaojinling area, Shaanxi Province. *Acta Petrol. Sin.* 27, 3095–3108 (in Chinese with English abstract).
- Shi, Z.S., Zhao, Z.W., Jin, H., Song, H.J., 2012. Depositional characteristics and its geological significance of the Upper Triassic Xiaotangzi Formation in Sichuan Basin. *J. Palaeogeogr.* 14, 477–486 (in Chinese with English abstract).
- Shi, Y., Yu, J.-H., Santosh, M., 2013. Tectonic evolution of the Qinling orogenic belt, Central China: new evidence from geochemical, zircon U-Pb geochronology and Hf isotopes. *Precambrian Res.* 231, 19–60.
- Sisson, T.W., Ratajeski, K., Hankins, W.B., Glazner, A.F., 2005. Voluminous granitic magmas from common basaltic sources. *Contrib. to Mineral. Petrol.* 148, 635–661.
- Smithies, R.H., 2000. The Archaean tonalite-trondhjemite-granodiorite (TTG) series is not an analogue of Cenozoic adakite. *Earth Planet. Sci. Lett.* 182, 115–125.

- Soder, C.G., Romer, R.L., 2018. Post-collisional potassio-ultrapotassio magmatism of the Variscan Orogen: implications for mantle metasomatism during continental subduction. *J. Petrol.* 59, 1007–1034.
- Song, P., Teng, J., Zhang, X., Liu, Y., Si, X., Ma, X., Qiao, Y., Dong, X., 2018. Flyover crustal structures beneath the Qinling Orogenic Belt and its tectonic implications. *J. Geophys. Res. -Sol. Ea.* 123, 6703–6718.
- Spakman, W., Chertova, M.V., van den Berg, A., van Hinsbergen, D.J.J., 2018. Puzzling features of western Mediterranean tectonics explained by slab dragging. *Nat. Geosci.* 11, 211–216.
- Stern, R.J., 2002. Subduction zones. *Rev. Geophys.* 40, 4.
- Stern, C.R., Kilian, R., 1996. Role of the subducted slab, mantle wedge and continental crust in the generation of adakites from the Andean Austral Volcanic Zone. *Contrib. Mineral. Petro.* 123, 263–281.
- Sternai, P., Jolivet, L., Menant, A., Gerya, T., 2014. Driving the upper plate surface deformation by slab rollback and mantle flow. *Earth Planet. Sci. Lett.* 405, 110–118.
- Streule, M.J., Strachan, R.A., Searle, M.P., Law, R.D., 2010. Comparing Tibet-Himalayan and Caledonian crustal architecture, evolution and mountain building processes. *Geol. Soc. Spec. Publ.* 335, 207–232.
- Sun, S.S., McDonough, W., 1989. Chemical and isotopic systematics of oceanic basalts: implications for mantle composition and processes. *Geol. Soc. Spec. Publ.* 42, 313–345.
- Sun, W.D., Li, S.G., Chen, Y.D., Li, Y.J., 2002. Timing of synorogenic granitoids in the South Qinling, Central China: constraints on the evolution of the Qinling-Dabie Orogenic Belt. *J. Geol.* 110, 457–468.
- Sylvester, P.J., 1998. Post-collisional strongly peraluminous granites. *Lithos* 45, 29–44.
- Tang, L., Santosh, M., Dong, Y., Tsunogae, T., Zhang, S., Cao, H., 2016. Early Paleozoic tectonic evolution of the North Qinling orogenic belt: evidence from geochemistry, phase equilibrium modeling and geochronology of metamorphosed mafic rocks from the Songshugou ophiolite. *Gondwana Res.* 30, 48–64.
- Teng, J.W., Li, S.L., Zhang, Y.Q., Zhao, J.R., Pi, J.L., Wang, F.Y., Yan, Y.F., Yang, H., Hu, G.Z., Pan, S.Z., 2014. Seismic wave fields and dynamical response for Qinling orogen and sedimentary basins and crystalline basement. *Chin. J. Geophys.* 57, 770–788 (in Chinese with English abstract).
- Tribuzio, R., Thirlwall, M.F., Vannucci, R., 2004. Origin of the gabbro–peridotite association from the Northern Apennine Ophiolites (Italy). *J. Petrol.* 45, 1109–1124.
- Valley, J.W., Kinny, P.D., Schulze, D.J., Spicuzza, M.J., 1998. Zircon megacrysts from kimberlite: oxygen isotope variability among mantle melts. *Contrib. Mineral. Petro.* 133, 1–11.
- Valley, J.W., Lackey, J.S., Cavosie, A.J., Clechenko, C.C., Spicuzza, M.J., Basei, M.A.S., Bindeman, I.N., Ferreira, V.P., Sial, A.N., King, E.M., Peck, W.H., Sinha, A.K., Wei, C.S., 2005. 4.4 billion years of crustal maturation: oxygen isotope ratios of magmatic zircon. *Contrib. Mineral. Petro.* 150, 561–580.
- van Hunen, J., Allen, M.B., 2011. Continental collision and slab break-off: a comparison of 3-D numerical models with observations. *Earth Planet. Sci. Lett.* 302, 27–37.
- Vogt, K., Matenco, L., Cloetingh, S., 2017. Crustal mechanics control the geometry of mountain belts. Insights from numerical modelling. *Earth Planet. Sci. Lett.* 460, 12–21.
- Wan, Y.S., Li, R.W., Wilde, S.A., Liu, D.Y., Chen, Z.Y., Yan, L., Song, T.R., Yin, X.Y., 2005. UHP metamorphism and exhumation of the Dabie Orogen, China: evidence from SHRIMP dating of zircon and monazite from a UHP granitic gneiss cobble from the Hefei Basin. *Geochim. Cosmochim. Acta* 69, 4333–4348.
- Wan, Y.S., Liu, D.Y., Dong, C.Y., Yin, X.Y., 2011. SHRIMP zircon dating of meta-sedimentary rock from the Qinling Group in the north of Xixia, North Qinling Orogenic Belt: constraints on complex histories of source region and timing of deposition and metamorphism. *Acta Petrol. Sin.* 27, 1172–1178 (in Chinese with English abstract).
- Wang, G.B., 1997. Isotope chronology and its significances of Foping gneiss system, south Qinling. *Northwest Geosci.* 18, 21–25 (in Chinese with English abstract).
- Wang, Z., Wang, T., Yan, Z., Yan, Q., 2002. Late Paleozoic forearc accretionary piggyback type basin system in the South Qinling, Central China. *Geol. Bull. Chi.* 21, 456–464 (in Chinese with English abstract).
- Wang, X., Wang, T., Jahn, B.-M., Hu, N., Chen, W., 2007. Tectonic significance of Late Triassic post-collisional lamprophyre dykes from the Qinling Mountains (China). *Geol. Mag.* 144, 837–848.
- Wang, T., Wang, X., Tian, W., Zhang, C., Li, W., Li, S., 2009. North Qinling Paleozoic granite associations and their variation in space and time: implications for orogenic processes in the orogens of central China. *Sci. China Earth Sci.* 52, 1359–1384.
- Wang, L., Kusky, T., Li, S.Z., 2010. Structural geometry and evolution of an exhumed ultra-high pressure eclogite massif, Yangkou Bay, Sulu Belt, China. *J. Struct. Geol.* 32, 423–444.
- Wang, X., Wang, T., Castro, A., Pedreira, R., Lu, X., Xiao, Q., 2011a. Triassic granitoids of the Qinling orogen, central China: genetic relationship of enclaves and rapakivi-textured rocks. *Lithos* 126, 369–387.
- Wang, H., Wu, Y.-B., Gao, S., Liu, X.-C., Gong, H.-J., Li, Q.-L., Li, X.-H., Yuan, H.-L., 2011b. Eclogite origin and timings in the North Qinling terrane, and their bearing on the amalgamation of the South and North China Blocks. *J. Metamorph. Geol.* 29, 1019–1031.
- Wang, X., Wang, T., Zhang, C., 2013a. Neoproterozoic, Paleozoic, and Mesozoic granitoid magmatism in the Qinling Orogen, China: constraints on orogenic process. *J. Asian Earth Sci.* 72, 129–151.
- Wang, L.-J., Griffin, W.L., Yu, J.-H., O'Reilly, S.Y., 2013b. U-Pb and Lu-Hf isotopes in detrital zircon from Neoproterozoic sedimentary rocks in the northern Yangtze Block: implications for Precambrian crustal evolution. *Gondwana Res.* 23, 1261–1272.
- Wang, H., Wu, Y.B., Gao, S., Liu, X.C., Liu, Q., Qin, Z.W., Xie, S.W., Zhou, L., Yang, S.H., 2013c. Continental origin of eclogites in the North Qinling terrane and its tectonic implications. *Precambrian Res.* 230, 13–30.
- Wang, F., Zhu, R., Hou, Q., Zheng, D., Yang, L., Wu, L., Shi, W., Feng, H., Sang, H., Zhang, H., Liu, Q., 2014a.  $^{40}\text{Ar}/^{39}\text{Ar}$  thermochronology on Central China Orogen: cooling, uplift and implications for orogeny dynamics. *Geol. Soc. Spec. Publ.* 378, 189–206.
- Wang, L., Kusky, T.M., Polat, A., Wang, S.J., Jiang, X.F., Zong, K.Q., Wang, J.P., Deng, H., Fu, J.M., 2014b. Partial melting of deeply subducted eclogite from the Sulu Orogen in China. *Nat. Commun.* 5, 5604.
- Wang, H., Wu, Y.-B., Gao, S., Qin, Z.-W., Hu, Z.-C., Zheng, J.-P., Yang, S.-H., 2016a. Continental growth through accreted oceanic arc: zircon Hf-O isotope evidence for granitoids from the Qinling orogen. *Geochim. Cosmochim. Acta* 182, 109–130.
- Wang, Q., Hawkesworth, C.J., Wyman, D., Chung, S.-L., Wu, F.-Y., Li, X.-H., Li, Z.-X., Gou, G.-N., Zhang, X.-Z., Tang, G.-J., Dan, W., Ma, L., Dong, Y.-H., 2016b. Pliocene-Quaternary crustal melting in central and northern Tibet and insights into crustal flow. *Nat. Commun.* 7, 11888.
- Wang, R., Xu, Z., Santosh, M., Liang, F., Fu, X., 2017. Petrogenesis and tectonic implications of the Early Paleozoic intermediate and mafic intrusions in the South Qinling Belt, Central China: Constraints from geochemistry, zircon U-Pb geochronology and Hf isotopes. *Tectonophysics* 712, 270–288.
- Wang, L., Wang, S.J., Brown, M., Zhang, J.F., Feng, P., Jin, Z.M., 2018. On the survival of intergranular coesite in UHP eclogite. *J. Metamorph. Geol.* 36, 173–194.
- Wang, R., Xu, Z., Santosh, M., Cai, Z., Xu, X., 2019. Formation of Dabashan arcuate structures: constraints from Mesozoic basement deformation in South Qinling Orogen, China. *J. Struct. Geol.* 118, 135–149.
- Wei, C.J., Yang, C.H., Zhang, S.G., Li, R.S., 1998. Discovery of granulite from the Foping area in southern Qinling Mountains and its geological significance. *Chin. Sci. Bull.* 43, 1358–1362.
- Weinberg, R.F., Hasalová, P., 2015. Water-fluxed melting of the continental crust: a review. *Lithos* 212, 158–188.
- Weislogel, A.L., Graham, S.A., Chang, E.Z., Wooden, J.L., Gehrels, G.E., 2010. Detrital zircon provenance from three turbidite depocenters of the Middle–Upper Triassic Songpan-Ganzi complex, central China: record of collisional tectonics, erosional exhumation, and sediment production. *Geol. Soc. Am. Bull.* 122, 2041–2062.
- Wortel, M.J.R., Spakman, W., 2000. Subduction and slab detachment in the Mediterranean-Carpathian region. *Science* 290, 1910–1917.
- Wu, Y.B., Zheng, Y.F., 2013. Tectonic evolution of a composite collision orogen: an overview on the Qinling-Tongbai-Hong'an-Dabie-Sulu orogenic belt in central China. *Gondwana Res.* 23, 1402–1428.
- Wu, F.Y., Huang, B.C., Ye, K., Fang, A.M., 2008a. Collapsed Himalayan-Tibetan orogen and the rising Tibetan Plateau. *Acta Petrol. Sin.* 24, 1–30 (in Chinese with English abstract).
- Wu, Y.B., Gao, S., Zhang, H.F., Yang, S.H., Jiao, W.F., Liu, Y.S., Yuan, H.L., 2008b. Timing of UHP metamorphism in the Hong'an area, western Dabie Mountains, China: evidence from zircon U-Pb age, trace element and Hf isotope composition. *Contrib. Mineral. Petro.* 155, 123–133.
- Wu, Y.B., Gao, S., Liu, X.C., Wang, J., Peng, M., Gong, H.J., Yuan, H.L., 2011. Two-stage exhumation of ultrahigh-pressure metamorphic rocks from the western Dabie Orogen, central China. *J. Geol.* 119, 15–31.
- Wu, G.-L., Meng, Q.-R., Duan, L., Li, L., 2014a. Early Mesozoic structural evolution of the eastern West Qinling, northwest China. *Tectonophysics* 630, 9–20.
- Wu, Y., Zhou, G., Gao, S., Liu, X., Qin, Z., Wang, H., Yang, J., Yang, S., 2014b. Petrogenesis of Neoarchean TTG rocks in the Yangtze Craton and its implication for the formation of Archean TTGs. *Precambrian Res.* 254, 73–86.
- Xia, L.Q., Xia, Z.C., Xu, X.Y., Li, X.M., Ma, Z.P., 2007. Petrogenesis of the Bikou Group volcanic rocks. *Earth Sci. Front.* 14, 84–101 (in Chinese with English abstract).
- Xia, L.Q., Xia, Z.C., Li, X.M., Ma, Z.P., Xu, X.Y., 2008. Petrogenesis of the Yaoling group, Wudang group volcanic rocks and basic dyke swarms from eastern part of the South Qinling Mountains. *Northeast Geol.* 41, 1–29 (in Chinese with English abstract).
- Xia, B., Brown, M., Wang, L., Wang, S.J., Piccoli, P., 2018. Phase equilibrium modeling of MT-UHP eclogite: a case study of coesite eclogite at Yangkou Bay, Sulu Belt, Eastern China. *J. Petrol.* 59, 1253–1280.
- Xu, Z.Q., Zhang, Z.M., Liu, F.L., Yang, J.S., Li, H.B., Yang, T.N., Qiu, H.J., Li, T.F., Meng, F.C., Chen, S.Z., Tang, Z.M., Chen, F.Y., 2003. Exhumation structure and mechanism of the Sulu ultrahigh-pressure metamorphic belt, central China. *Acta Geol. Sin.* 77, 432–450 (in Chinese with English abstract).
- Xu, S., Liu, Y., Chen, G., Ji, S., Ni, P., Xiao, W., 2005. Microdiamonds, their classification and tectonic implications for the host eclogites from the Dabie and Su-Lu regions in central eastern China. *Mineral. Mag.* 69, 509–520.
- Xu, C., Chakhmouradian, A.R., Taylor, R.N., Kynicky, J., Li, W., Song, W., Fletcher, I.R., 2014. Origin of carbonatites in the South Qinling orogen: implications for crustal recycling and timing of collision between the South and North China Blocks. *Geochim. Cosmochim. Acta* 143, 189–206.
- Xu, Z., Dilek, Y., Cao, H., Yang, J., Robinson, P., Ma, C., Li, H., Jolivet, M., Roger, F., Chen, X., 2015. Paleo-Tethyan evolution of Tibet as recorded in the East Cimmerides and West Cathaysides. *J. Asian Earth Sci.* 105, 320–337.
- Yan, Q.R., Hanson, A.D., Wang, Z.Q., Druschke, P.A., Yan, Z., Wang, T., Liu, D.Y., Song, B., Jian, P., Zhou, H., Jiang, C.F., 2004. Neoproterozoic subduction and rifting on the northern margin of the Yangtze plate, China: implications for Rodinia reconstruction. *Int. Geol. Rev.* 46, 817–832.
- Yan, Z., Wang, Z., Wang, T., Yan, Q., Xiao, W., Li, J., 2006a. Provenance and tectonic setting of clastic deposits in the Devonian Xicheng Basin, Qinling orogen, central China. *J. Sediment. Res.* 76, 557–574.
- Yan, Z., Wang, Z., Yan, Q., Wang, T., Xiao, W., Li, J., Han, F., Chen, J., Yang, Y., 2006b. Devonian sedimentary environments and provenance of the Qinling orogen: constraints on late Paleozoic southward accretionary tectonics of the North China craton. *Int. Geol. Rev.* 48, 585–618.
- Yan, Z., Wang, Z., Wang, T., Yan, Q., Xiao, W., Li, J., Han, F., Chen, J., 2007. Tectonic setting of Devonian sediments in the Qinling orogen: constraints from detrital modes and geochemistry of clastic rocks. *Acta Petrol. Sin.* 23, 1023–1042 (in Chinese with English abstract).

- Yan, Z., Wang, Z., Chen, J., Yan, Q., Wang, T., Zhang, Y., 2009. Geochemistry and SHRIMP zircon U-Pb dating of amphibolites from the Danfeng Group in the Wuguan area, North Qinling Terrane and their tectonic significance. *Acta Geol. Sin.* 83, 1632–1645 (in Chinese with English abstract).
- Yan, Z., Wang, Z., Yan, Q., Wang, T., Guo, X., 2012a. Geochemical constraints on the provenance and depositional setting of the Devonian Liuling Group, East Qinling Mountains, Central China: implications for the tectonic evolution of the Qinling Orogenic Belt. *J. Sediment. Res.* 82, 9–20.
- Yan, Z., Wang, Z., Li, J., Xu, Z., Deng, J., 2012b. Tectonic settings and accretionary orogenesis of the West Qinling Terrane, northeastern margin of the Tibet Plateau. *Acta Petrol. Sin.* 28, 1808–1828 (in Chinese with English abstract).
- Yan, M., Liu, S.W., Li, Q.G., Yang, P.T., Wang, W., Guo, R.R., Bai, X., Deng, Z.B., 2014a. LA-ICP-MS zircon U-Pb chronology and Lu-Hf isotopic features of the Mi hunzhen pluton in the South Qinling tectonic belt. *Acta Petrol. Sin.* 30, 390–400 (in Chinese with English abstract).
- Yan, Z., Guo, X., Fu, C., Aitchison, J., Wang, Z., Li, J., 2014b. Detrital heavy mineral constraints on the Triassic tectonic evolution of the West Qinling terrane, NW China: implications for understanding subduction of the Paleotethyan Ocean. *J. Geol.* 122, 591–608.
- Yan, Z., Aitchison, J.C., Fu, C., Guo, X., Xia, W., Niu, M., 2016a. Devonian sedimentation in the Xiqingshan Mountains: implications for paleogeographic reconstructions of the SW Qinling Orogen. *Sediment. Geol.* 343, 1–17.
- Yan, Z., Fu, C., Aitchison, J.C., Buckman, S., Niu, M., Cao, B., 2020. Triassic turbidites in the West Qinling Mountains, NW China: part of the collisional Songpan-Ganzi Basin or an active forearc basin? *J. Asian Earth Sci.* 194, 104366.
- Yan, Z., Fu, C., Wang, Z., Yan, Q., Chen, L., Chen, J., 2016b. Late Paleozoic subduction-accretion along the southern margin of the North Qinling terrane, central China: evidence from zircon U-Pb dating and geochemistry of the Wuguan Complex. *Gondwana Res.* 30, 97–111.
- Yang, Y., 2017. Spatial-Temporal Distribution and Sources of Granitoids in the Middle Qinling Orogenic Belt, Central China: Implications for the Nature of Deep Crustal Basement. *Chinese Acad. Geol. Sci.*, Beijing, pp. 1–185 (in Chinese with English abstract).
- Yang, C.H., Wei, C.J., Zhang, S.C., Li, H.M., Wan, Y.S., Li, R.S., 1999. U-Pb zircon dating of granulite facies rocks from the Foping area in the Southern Qinling Mountains. *Geol. Rev.* 45, 173–179 (in Chinese with English abstract).
- Yang, J.-H., Chung, S.-L., Zhai, M.-G., Zhou, X.-H., 2004. Geochemical and Sr-Nd-Pb isotopic compositions of mafic dikes from the Jiaodong Peninsula, China: evidence for vein-plus-peridotite melting in the lithospheric mantle. *Lithos* 73, 145–160.
- Yang, B.L., Zhang, C.L., Li, L., 2011. Sr-Nd-Pb isotopic characteristics of the granitoids in the Douling complexes, eastern Qinling, China and its geological significance. *Geol. Bull. Chi.* 30, 439–447 (in Chinese with English abstract).
- Yang, P., Liu, S., Li, Q., Wang, Z., Wang, R., Wang, W., 2012a. Geochemistry and zircon U-Pb-Hf isotopic systematics of the Ningshan granitoid batholith, middle segment of the south Qinling belt, Central China: constraints on petrogenesis and geodynamic processes. *J. Asian Earth Sci.* 61, 166–186.
- Yang, P., Liu, S., Li, Q., Wang, Z., Wang, W., Bai, X., 2012b. Emplacing age of the Tiewadian Pluton in the South Qinling Tectonic Belt and its geological implications. *Acta Geol. Sin.* 86, 1525–1540 (in Chinese with English abstract).
- Yang, P., Liu, S., Li, Q., Wang, Z., Zhang, F., Wang, W., 2014. Chronology and petrogenesis of the Hejiazhuang granitoid pluton and its constraints on the Early Triassic tectonic evolution of the South Qinling Belt. *Sci. China Earth Sci.* 57, 232–246.
- Yang, L.-Q., Deng, J., Dilek, Y., Qiu, K.-F., Ji, X.-Z., Santosh, M., Song, K.-R., Song, Y.-H., Geng, J.-Z., Zhang, C., Hua, B., 2015a. Magma mixing and crust-mantle interaction in the Triassic monzogranites of Bikou Terrane, central China: constraints from petrology, geochemistry, and zircon U-Pb-Hf isotopic systematics. *J. Asian Earth Sci.* 98, 320–341.
- Yang, L.-Q., Deng, J., Dilek, Y., Qiu, K.-F., Ji, X.-Z., Li, N., Taylor, R.D., Yu, J.-Y., 2015b. Structure, geochronology, and petrogenesis of the Late Triassic Puziba granitoid dikes in the Mianlue suture zone, Qinling orogen, China. *Geol. Soc. Am. Bull.* 127, 1831–1854.
- Yang, X.K., Han, K., Wu, X., Wang, B.Y., Wang, X., Yang, H.Y., He, J.H., Chao, H.X., Yu, H.B., 2016. The structural deformation and tectonic evolution of intra-continental orogeny in South Qinling orogen: structural deformation analysis of the northern part of Shiquan-Hanyan belt in the late Indosian-Yanshanian period. *Earth Sci. Front.* 23, 72–80 (in Chinese with English abstract).
- Yuan, C., Zhou, M.F., Sun, M., Zhao, Y., Wilde, S., Long, X., Yan, D., 2010. Triassic granitoids in the eastern Songpan-Ganzi Fold Belt, SW China: magmatic response to geodynamics of the deep lithosphere. *Earth Planet. Sci. Lett.* 290, 481–492.
- Zhai, X., Day, H.W., Hacker, B.R., You, Z., 1998. Paleozoic metamorphism in the Qinling orogen, Tongbai Mountains, central China. *Geology* 26, 371–374.
- Zhang, R.Y., Liou, J.G., 1996. Coesite inclusions in dolomite from eclogite in the southern Dabie Mountains, China: the significance of carbonate minerals in UHPM rocks. *Am. Mineral.* 81, 181–186.
- Zhang, E.P., Niu, D.Y., Huo, Y.G., Zhang, L.F., Li, Y.G., 1993. *Geologic-Tectonic Features of Qinling-Dabashan Mountains and Adjacent Regions*. Geological Publishing House, Beijing, pp. 1–291 (in Chinese with English abstract).
- Zhang, G., Zhang, B., Yuan, X.C., Xiao, Q., 2001. *Qinling Orogenic Belt and Continental Dynamics*. Science Press, Beijing, pp. 1–806 (in Chinese with English abstract).
- Zhang, B.R., Gao, S., Zhang, H.F., Han, Y.W., 2002a. *Geochemistry of Qinling Orogenic Belt*. Science Press, Beijing, pp. 1–188 (in Chinese).
- Zhang, Z.Q., Zhang, G.W., Tang, S.H., Xu, J.F., Yang, Y.C., Wang, J.H., 2002b. Age of Anzishan granulites in the Mianxian-Lueyang suture zone of Qinling Orogen: with a discussion of the timing of final assembly of Yangtze and North China Craton blocks. *Chin. Sci. Bull.* 22, 1925–1930.
- Zhang, Z.Q., Song, B., Tang, S.H., Zhang, S.G., Yang, Y.S., Wang, J.H., 2004. Age and material composition of the Foping metamorphic crystalline complex in the Qinling Mountains: SHRIMP zircon U-Pb and whole-rock Sm-Nd geochronology. *Geol. China* 31, 161–168 (in Chinese with English abstract).
- Zhang, Z.Q., Zhang, G.W., Liu, D.Y., Wang, Z.Q., Tang, S.H., Wang, J.H., 2006a. *Isotopic Geochronology and Geochemistry of Ophiolites, Granites and Clastic Sedimentary Rocks in the Qinling Orogenic Belt*. Geol. Publ. House, Beijing, pp. 1–348 (in Chinese).
- Zhang, S.-B., Zheng, Y.-F., Wu, Y.-B., Zhao, Z.-F., Gao, S., Wu, F.-Y., 2006b. Zircon isotope evidence for  $\geq 3.5$  Ga continental crust in the Yangtze craton of China. *Precambrian Res.* 146, 16–34.
- Zhang, H.F., Jin, L.L., Zhang, L., Harris, N., Zhou, L., Hu, S.H., Zhang, B.R., 2007. Geochemical and Pb-Sr-Nd isotopic compositions of granitoids from western Qinling belt: Constraints on basement nature and tectonic affinity. *Sci. China Earth Sci.* 50, 184–196.
- Zhang, R.Y., Liou, J.G., Ernst, W.G., 2009. The Dabie-Sulu continental collision zone: a comprehensive review. *Gondwana Res.* 16, 1–26.
- Zhang, C., Liu, L., Wang, T., Wang, X., Li, L., Gong, Q., Li, X., 2013. Granitic magmatism related to early Paleozoic continental collision in North Qinling. *Chin. Sci. Bull.* 58, 4405–4410.
- Zhang, H.Y., Ducea, M.N., Ding, L., Pullen, A., Kapp, P., Hoffman, D., 2014a. Southern Tibetan Oligocene-Miocene adakites: a record of Indian slab tearing. *Lithos* 210, 209–223.
- Zhang, S.M., Jiang, G.L., Liu, K.F., Wang, C.G., 2014b. Evolution of Neoproterozoic-Mesozoic sedimentary basins in Qinling-Dabie Orogenic Belt. *Earth Sci. -J. China Univ. Geosci.* 39, 1185–1199 (in Chinese with English abstract).
- Zhang, H., Ye, R.-S., Liu, B.-X., Wang, Y., Zhang, Y.-S., Siebel, W., Chen, F., 2016. Partial melting of the South Qinling orogenic crust, China: evidence from Triassic migmatites and diorites of the Foping dome. *Lithos* 260, 44–57.
- Zhang, J., Zhang, H.-F., Li, L., 2018. Neoproterozoic tectonic transition in the South Qinling Belt: new constraints from geochemistry and zircon U-Pb-Hf isotopes of diorites from the Douling Complex. *Precambrian Res.* 306, 112–128.
- Zhao, X.X., Coe, R.S., 1987. Palaeomagnetic constraints on the collision and rotation of North and South China. *Nature* 327, 141–144.
- Zhao, T., Zhai, M., Xia, B., Li, H., Zhang, Y., Wan, Y., 2004. Zircon U-Pb SHRIMP dating for the volcanic rocks of the Xionger Group: constraints on the initial formation age of the cover of the North China Craton. *Chin. Sci. Bull.* 49, 2495–2502.
- Zhao, Z.-F., Zheng, Y.-F., Gao, T.-S., Wu, Y.-B., Chen, B., Chen, F.K., Wu, F.-Y., 2006. Isotopic constraints on age and duration of fluid-assisted high-pressure eclogite-facies recrystallization during exhumation of deeply subducted continental crust in the Sulu orogen. *J. Metamorph. Geol.* 24, 687–702.
- Zhao, J.-H., Zhou, M.-F., Zheng, J.-P., Fang, S.-M., 2010. Neoproterozoic crustal growth and reworking of the Northwestern Yangtze Block: constraints from the Xixiang dioritic intrusion, South China. *Lithos* 120, 439–452.
- Zhao, S., Li, S., Liu, X., Santosh, M., Somerville, I.D., Cao, H., Yu, S., Zhang, Z., Guo, L., 2015. The northern boundary of the Proto-Tethys Ocean: constraints from structural analysis and U-Pb zircon geochronology of the North Qinling Terrane. *J. Asian Earth Sci.* 113, 560–574.
- Zhao, S., Li, S., Yu, S., Li, X., Cao, H., Liu, X., Wang, P., 2016. Proto-Tethys Ocean in East Asia (III): structures of ductile shear zones in the North Qinling. *Acta Petrol. Sin.* 32, 2645–2655 (in Chinese with English abstract).
- Zhao, Z.F., Liu, Z.B., Chen, Q., 2017. Melting of subducted continental crust: geochemical evidence from Mesozoic granitoids in the Dabie-Sulu orogenic belt, east-central China. *J. Asian Earth Sci.* 145, 260–277.
- Zhao, J.-H., Li, Q.-W., Liu, H., Wang, W., 2018. Neoproterozoic magmatism in the western and northern margins of the Yangtze Block (South China) controlled by slab subduction and subduction-transform-edge-propagator. *Earth-Sci. Rev.* 187, 1–18.
- Zhao, J., Dong, Y., Huang, B., 2020. Paleomagnetic constraints of the Lower Triassic Strata in South Qinling Belt: evidence for a discrete terrane between the North and South China Blocks. *Tectonics* 39, e2019TC005698.
- Zheng, Y., 2008. A perspective view on ultrahigh-pressure metamorphism and continental collision in the Dabie-Sulu orogenic belt. *Chin. Sci. Bull.* 53, 3081–3104.
- Zheng, Y.F., Wu, Y.B., Zhao, Z.F., Zhang, S.B., Xu, P., Wu, F.Y., 2005. Metamorphic effect on zircon Lu-Hf and U-Pb isotope systems in ultrahigh-pressure eclogite facies metagranite and metabasite. *Earth Planet. Sci. Lett.* 240, 378–400.
- Zheng, R.C., Dai, Z.C., Zhu, R.K., Zhai, W.L., Gao, G.C., Geng, W., 2009. Sequence-based lithofacies and paleogeographic characteristics of Upper Triassic Xujiahe Formation in Sichuan Basin. *Geol. Rev.* 55, 484–495 (in Chinese with English abstract).
- Zheng, Y.-F., Xia, Q.-X., Chen, R.-X., Gao, X.-Y., 2011. Partial melting, fluid supercriticality and element mobility in ultrahigh-pressure metamorphic rocks during continental collision. *Earth-Sci. Rev.* 107, 342–374.
- Zheng, Y., Zhao, Z., Chen, Y., 2013. Continental subduction channel processes: Plate interface interaction during continental collision. *Chin. Sci. Bull.* 58, 4371–4377.
- Zheng, Y.-F., Zhao, Z.-F., Chen, R.-X., 2018. Ultrahigh-pressure metamorphic rocks in the Dabie-Sulu orogenic belt: compositional inheritance and metamorphic modification. *Geol. Soc. Spec. Publ.* SP474.479.
- Zhou, M.F., Ma, Y., Yan, D.P., Xia, X., Zhao, J.H., Sun, M., 2006. The Yanbian terrane (Southern Sichuan Province, SW China): a Neoproterozoic arc assemblage in the western margin of the Yangtze block. *Precambrian Res.* 144, 19–38.
- Zhou, L.-G., Xia, Q.-X., Zheng, Y.-F., Chen, R.-X., Hu, Z., Yang, Y., 2015. Tectonic evolution from oceanic subduction to continental collision during the closure of Paleotethyan ocean: geochronological and geochemical constraints from metamorphic rocks in the Hong'an orogen. *Gondwana Res.* 28, 348–370.
- Zhu, R.X., Yang, Z.Y., Wu, H.N., Ma, X.H., Huang, B.C., Meng, Z.F., Fang, D.J., 1998. Paleomagnetic constraints on the tectonic history of the major blocks of China during the Phanerozoic. *Sci. China Earth Sci.* 41, 1–19.
- Zhu, X., Chen, F., Nie, H., Siebel, W., Yang, Y., Xue, Y., Zhai, M., 2014. Neoproterozoic tectonic evolution of South Qinling, China: evidence from zircon ages and geochemistry of the Yaoling volcanic rocks. *Precambrian Res.* 245, 115–130.

- Zhu, X., Chen, F., Liu, B., Zhang, H., Zhai, M., 2015a. **Geochemistry and zircon ages of mafic dikes in the South Qinling, central China: evidence for late Neoproterozoic continental rifting in the northern Yangtze block**. *Int. J. Earth Sci. (Geol Rundsch)* 104, 27–44.
- Zhu, D.C., Wang, Q., Zhao, Z.D., Chung, S.L., Cawood, P.A., Niu, Y., Liu, S.A., Wu, F.Y., Mo, X.X., 2015b. **Magmatic record of India-Asia collision**. *Sci. Rep.* 5, 14289.
- Zhu, G., Liu, C., Gu, C., Zhang, S., Li, Y., Su, N., Xiao, S., 2018. **Oceanic plate subduction history in the western Pacific Ocean: constraint from late Mesozoic evolution of the Tan-Lu Fault Zone**. *Sci. China Earth Sci.* 61, 386–405.
- Zou, G.F., Xia, T., Lou, X.Y., 2003. **Sequence stratigraphy of the Late Triassic strata in the Guangyuan region, Sichuan**. *Sediment. Geol. Tethys. Geol.* 23, 73–80 (in Chinese with English abstract).



**Fangyang Hu** is a postdoctoral researcher at the Institute of Geology and Geophysics, Chinese Academy of Sciences since 2018. He graduated with a BS from the China University of Geosciences (Wuhan), P.R. China, in 2013, and received his PhD from the Peking University, P.R. China, in 2018. His main research interests are magmatism, especially granitoid magmatism, mantle and crust interaction, and crustal and tectonic evolution during continental collisional process.



**Shuwen Liu** is a professor of the School of Earth and Space Sciences, Peking University, PR China. He obtained his BS (1982), MS (1988), and PhD (1991) from the Changchun College of Geology, PR China (now the College of Earth Sciences in Jilin University) in 1991 and worked at the Peking University since 1991. His research focused on geochronology, magmatism, metamorphism, and crustal evolution of the North China Craton during the Precambrian age. To date, he has published over 200 papers and 4 books.



**Mihai N. Ducea** is a professor of Geology at the University of Arizona and also holds a courtesy appointment at the University of Bucharest, Romania. He received a BS from the University of Bucharest, followed by a PhD at Caltech. His research is primarily aimed at understanding links between igneous and metamorphic petrologic processes and the tectonic evolution of continents. He is primarily interested in continental margin processes, e.g., in the western North American Cordillera, the central Andes, the Carpathians, and southern Tibet. He is a Fellow of the Geological Society of America.

**James B. Chapman** is an assistant professor at the University of Wyoming. He obtained his BS from the College of William and Mary in 2003, and MS from the University of Texas El Paso in 2008, and PhD from the University of Arizona in 2018. His research focuses on the tectonics of convergent margins and the evolution of the continental lithosphere. He is especially interested in the tectonics of continental arcs and continental collisional orogens, e.g., the American Cordillera, the Andes, and Tibet.

**Fuyuan Wu** is a professor and the director of the Institute of Geology and Geophysics, Chinese Academy of Sciences. He received his BS (1984), MS (1987), and PhD (1990) from the Changchun College of Geology, PR China (now the College of Earth Sciences in Jilin University). His research is focused on granite petrogenesis, mantle geochemistry, geochronology, and isotopic geochemistry. He is an academician of Chinese Academy of Sciences and is recognized as a Fellow of the Geological Society of America and a Geochemistry Fellow of the Geochemical Society and the European Association of Geochemistry.

**Timothy Kusky** is a Distinguished Professor, Changjiang Scholar, and Director of the Center for Global Tectonics in the School of Earth Sciences at China University of Geosciences, Wuhan. Since his PhD at Johns Hopkins University in 1990, he has authored several hundred papers and over two dozen books, with research in the fields of global tectonics, neotectonics, convergent margins, and the early history of the Earth. He is a Fellow of the Geological Society of America, and a Friendship Medal Laureate of the Peoples Republic of China, the highest award to foreigners in China.